

©Copyright 2018

Vaishnavi Nattar Ranganathan

Wireless Biomedical Sensing:
Wireless Power, Communication and Computation for Wearable and
Implantable Devices

Vaishnavi Nattar Ranganathan

A dissertation
submitted in partial fulfillment of the
requirements for the degree of

Doctor of Philosophy

University of Washington

2018

Dissertation Reading Committee:

Joshua R. Smith, Chair

Chet T. Moritz

Sidhant Gupta

Program Authorized to Offer Degree:
Electrical Engineering

University of Washington

Abstract

Wireless Biomedical Sensing:
Wireless Power, Communication and Computation for Wearable and Implantable Devices

Vaishnavi Nattar Ranganathan

Chair of the Supervisory Committee: Joshua R. Smith
Department of Electrical Engineering

This work addresses challenges in power delivery, efficient computation and communication to power-constrained wearable and implantable devices. We are surrounded today by over 25 billion smart devices, and this number is constantly increasing. Owing to the shrinking CMOS technology, some of these devices are so small that they can even be worn on the human body or implanted inside it. The sheer number of devices and their drastic miniaturization and integration into the human body posit two major challenges. First, how do we communicate with these numerous small devices? Second, how do we deliver power to them? The wearable or implantable nature of these smart devices only exacerbates these challenges. Since these devices are designed to be worn or implanted, they must be small, comfortable and, most importantly, safe to use. They must be small so that they are discrete when worn or can be implanted easily. They must be comfortable so that people can use them for extended periods of time for physiological monitoring, without the devices interfering with their normal lifestyle. Finally, they must not cause discomfort by overheating and operate at low power consumption so that they are safe to use.

Traditionally, cables were used to power or communicate. However, with the proliferation of smart devices, tethering to communicate with or to recharge them is no longer a practical solution. Bluetooth technology allows some degree of wireless communication with smart devices, but it is a power-hungry technology and thus unsuited for implanted devices. Hence

there is a need for reliable communication of data at low power levels. Batteries are currently the most prevalent option for power delivery, but are a less-than-ideal solution. While progress in CMOS technology has reduced size and power consumption of smart devices, the batteries used to power them are still large. With higher energy requirements, larger these batteries become. Even when rechargeable, these batteries have a diminishing efficiency over their lifetime of about two to three years. Hence, they are not the best option for powering these billions of devices, especially when they are implanted in the body and need surgery for replacement.

One of the solutions to make these devices untethered and battery free is to use wireless power transfer and low-power wireless communication. However, these smart devices used in diverse application have vastly different power requirements and communication data rates. Hence, it becomes difficult to standardize ways to wirelessly power and communicate with them. The wireless solutions presented here are applied to two different applications, one wearable and the other implantable, demonstrating the ability to serve diverse requirements.

The first application includes a wearable sensing platform that operates with ultra-low power consumption to perform analog sensing of physiological signals and use backscatter communication, which is an ultra-low power communication method, to transmit sensed data. The total power consumption for sensing and communicating data to an external base station is as low as $35 \mu\text{W}$ to $160 \mu\text{W}$. This modular wireless platform is battery-free and can be made in the form of an adhesive bandaid that can sense physiological parameters like heart rate, breathing rate and sense sounds to monitor health conditions. Thus it enables simple, continuous and seamless monitoring of health parameters while a person goes about their everyday tasks.

The second application is an implantable platform that can record neural signals from the brain and process them locally to identify events in the signals that can trigger neural stimulations. The requirements for this implantable device are far more complex than the simple wearable application. The implants operate with several 100 mW of power

consumption and need several Mbps data rates to transmit the recorded and processed data out to the user. To address the high power and high data rate requirements, this work presents a novel dual-band approach that supports wireless power delivery at high frequency (HF) and backscatter communication at ultra-high frequency (UHF). At the smart implantable device, the dual-band wireless system harvests energy from HF wireless signals while simultaneously communicating data using UHF backscatter. To localize the implant and deliver power to it, a novel low-overhead echolocation method is presented in this work. This method uses reflected parameters on a phased array of wireless power transmitters to locate the wireless device and deliver focussed power to it.

The implantable platform is intended for use in two different application domains. First, in neural engineering research where neural interface devices are used to understand, record and map the brain function and to leverage them and develop brain-controlled technology like prosthetic limbs. Second, for treatment and rehabilitation of people suffering from spinal cord injury and chronic neural disorders. An implantable brain-computer-spinal interface (BCSI) is presented in this work, that records neural signals and processes them locally to extract intent. The decoded action intention can be used to trigger stimulation in the spinal cord to reanimate the paralyzed limb and perform the action. In addition, this device is developed as a low-power FPGA-based platform so that it is reconfigurable to enable research in closed-loop algorithms to understand and treat several other neural disorders. We expect that such wireless biomedical sensing can provide a better understanding of physiological parameters and enable treatment for chronic disorders.

Table of Contents

	Page
List of Figures	iii
Chapter 1: Introduction	1
1.1 RF Bandaid: An ultra-low power wearable biosensor	4
1.2 Brain-Computer-Spinal Interface: A Low-Power Implantable Neural Interface	4
1.3 Thesis Organization	7
Chapter 2: Wearable Sensor Platform: The RF Bandaid	9
2.1 Introduction	9
2.2 System Design and Theory of Operation	12
2.3 Application-Specific Design Options	19
2.4 Testing and Results	22
2.5 Related Work	32
2.6 Conclusion	38
Chapter 3: Implantable Wireless Neural Stimulator	39
3.1 Dual-Band Power Transfer and Communication	39
3.2 System Design	42
3.3 System Characterization	44
3.4 Wireless Spinal Stimulation	46
3.5 System Evolution	47
3.6 Summary	48
Chapter 4: High Data-Rate Backscatter Communication for Implants	49
4.1 System Design	49
4.2 Experimental Validation	53
4.3 Summary	56
Chapter 5: Localized Wireless Power Delivery	57
5.1 Introduction to Phased-Array WPT and HF Echolocation	57

5.2	Theoretical Analysis of Phased-Array Power and Localization	60
5.3	Validation of Phased-Array Operation	66
5.4	Experimental Validation of Echolocation	70
5.5	Summary	76
Chapter 6:	Closed-Loop Neural Interface	77
6.1	Introduction	77
6.2	System Design	78
6.3	Test setup	82
6.4	Results and Discussion	84
6.5	Conclusion	85
Chapter 7:	Discussion for Closed-Loop Spike Signal Analysis	86
7.1	Signal Acquisition and Stimulation	86
7.2	Intent Decoding For Closed-Loop Operation	88
7.3	Algorithm Analysis Results	92
Chapter 8:	Discussion and Thesis Conclusion	97
Bibliography	101

List of Figures

Figure Number	Page
1.1 Number of connected devices in comparison to human population on earth between 2003 and 2020-projection by Cisco (left). Impact of technology on medical sensing-wearable and implantable devices (right)	1
1.2 Application space for smart connected devices (left). Image of a smart watch and a pacemaker with large batteries (right)	3
2.1 A system level description of the RF Bandaid system and sensors used for testing	13
2.2 A functional block diagram detailing the fully-analog RF sensing platform . .	16
2.3 Heart rate data, sensed as radial pressure signals with the RF sensing platform, along with the ground truth EKG signal	23
2.4 Breathing rate data, sensed using an e-textile stretch sensor along with the RF sensing platform, annotated with exhale indicators	24
2.5 Experimental setup for long range testing and an RF spectrum of the test environment	26
2.6 Temperature data measured using an RTD and the RF sensing platform, along with the ground truth data from a commercial temperature logger . .	27
2.7 High-bandwidth audio sensed using an electret microphone and the RF sensing platform. Audio used: The Guild Wars 2 title music	30
2.8 Spectrogram plots for a continuous frequency sweep, white noise, speech and music audio signal transmission.	31
2.9 Power vs. range representation of the RF backscatter device space	33
3.1 a) System architecture and control for the wireless neural stimulator, b) labeled control PCB	40
3.2 Design specifications for near-field HF (wireless power) and UHF (Backscatter Communication) coils	44
3.3 Characterization of HF WPT, a) shows the plot of $ S21 ^2$ frequency response for varied distances between Tx and Rx. b) is the S21 trace at 13.56MHz. The overcoupled region is indicated by the dip in S21 at 10mm. c) Implant in rat for temerature monitoring while transmitting 100mW of load power and d), e) and f) characterization of simultaneous UHF BSC communication at varying distances. Communication was good up to 20mm	46

3.4	The sedated rat with wirelessly powered and wirelessly controlled epidural stimulator, a) provices StTAs of triceps EMG response to spinal stimulation. Arrow indicates time at which stimulus was delivered.	47
3.5	a) Prototype version 2 without coils, b) Board version 3 with WPT coil.	48
4.1	Top level architecture of proposed approach for simultaneous WPT and bi-directional communication	50
4.2	Transmit and receive resonators for simultaneous WPT and bi-directional communication	51
4.3	Near field UHF bi-directional communication performance.	54
4.4	A time domain oscilloscope measurement of the baseband bi-directional communication between the external reader and the implanted system.	55
4.5	Co-existence of WPT and communication	56
5.1	Circuit representation of a three coil system.	61
5.2	V_o for a range of α and ϕ for a three-coil phased-array system with varying k_{12} , k_{13} , k_{23}	64
5.3	System level block diagram of experimental configuration using two Tx coils and one Rx coil.	67
5.4	Experimental and simulation results for received power corresponding to three different coil configurations and various Tx power levels.	69
5.5	(A) Schematic of transmitter, (B) Experimental setup. The time trace of Tx power variation during phase sweep for (C) Adjacent, (D) Overlap, and (E) Optimal configurations.	71
5.6	Different positions of the Rx coil used in the localization experiments. Tx Coils were positioned in the optimal overlap configuration.	72
5.7	Magnitude plots for reflected signals over ϕ sweep for nine Rx positions.	72
5.8	Phase plots for reflected signals over ϕ sweep for nine Rx positions.	73
5.9	(A) LOC constellation plot showing averaged LOC parameter for three different distances and each position from multiple trials(B) Test case localization points were added for 2° and 3° sweep interval	75
6.1	Functional Block Diagram of the NeuralCLIP and its application for spinal cord injury rehabilitation	79
6.2	Timing diagram illustrating the record, and process pipeline for closed-loop operation	80
6.3	Power consumption vs. system clock	82

6.4	Spectral content from a single channel of neural recording and corresponding lever push data	83
6.5	Test signals at 30 Hz, 200 Hz and 800 Hz recorded and processed on the BCSI device	84
6.6	Recorded and processed local field potential signal with ground truth lever push task signal	85
7.1	Signal processing steps involved in the closed-loop BCSI system, taking a rat as the subject	87
7.2	Template for positive and negative phase spikes that are found in the recorded time series data	89
7.3	Raw and filtered neural signals showing spikes and artifact	93
7.4	Spike detection and artifact rejection with three separate methods	94
7.5	Number of spikes detected per channel using the three different algorithms .	95

Acknowledgments

I would like to first thank my advisor Prof. Josh Smith for being the best advisor and a friend over the past five years of my PhD. His unwavering trust and patience helped me find interesting topics to work on and his guidance has helped me in both research and life. I thank him for creating a lab where I could truly enjoy working towards my PhD.

I would also like to thank Prof. Chet Moritz, and my colleagues in the Sensor Systems Lab and the Moritz Lab for their invaluable support, memorable conversations and the sleepless nights spent working towards deadlines. I would also like to thank my mentors Dr. Benjamin Waters, Dr. Jonathan Lester and Dr. Sidhant Gupta for their insightful advice and everything they have taught me.

Dedication

To my family:

My parents, Gayathri, Karthik and my husband Seetharam.

Chapter 1

Introduction

We are currently witnessing the transition of technology from an era of human-machine interface to an era of human-machine integration. Driven by the vision of an Internet of Things, each person is associated with numerous smart sensing devices. These devices have become integrated into our everyday life, thus enabling a comfortable and healthy lifestyle. In 2008, the number of smart devices overtook the human population on earth and their numbers have only increased further since. According to a conservative projection by Cisco, by the year 2020 each person on earth will be associated with an average of seven smart objects (Fig. 1.1). The increase in smart connected sensing is already visible today in the form of smart homes and other distributed networks of commercially available sensors and systems [1].

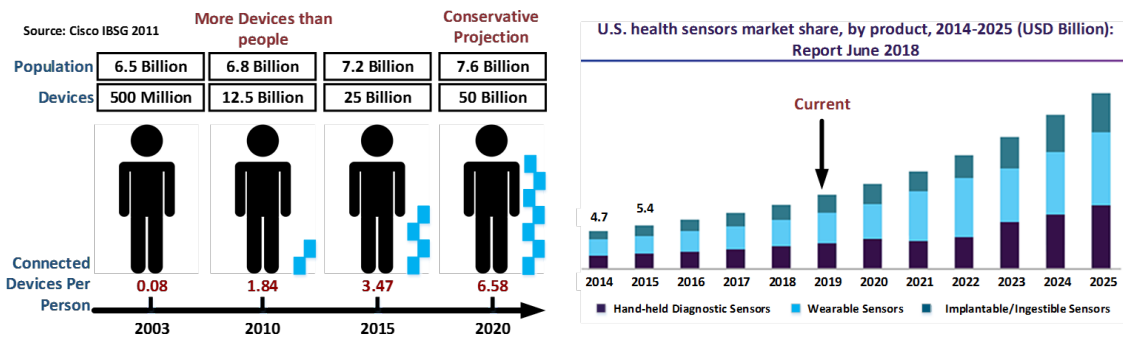


Figure 1.1: Number of connected devices in comparison to human population on earth between 2003 and 2020-projection by Cisco (left). Impact of technology on medical sensing-wearable and implantable devices (right).

In the biomedical field, recent advances in technology has led to the early diagnosis of

various health disorders and helped develop and deliver appropriate treatment for them. With this came the increased life expectancy and awareness of fitness and health. Recent development in technology targeted at biomedical applications has accelerated this field by providing handheld systems and wearable or implantable devices that are safe and reliable treatment options. Recently, as a result of the rising geriatric population and awareness of risks posed by disorders like stroke and diabetes, there is an increasing demand for home-based health monitoring.

On one hand, simple mobile monitoring devices like the Apple watch, Fitbit and the Garmin chest strap are widely used to monitor physiological parameters like heart rate and physical wellness. On the other hand, chronic implantable technology like pacemakers, deep brain stimulators and cochlear implants provide treatment for chronic disorders. The main functions of both sets of devices is to perform physiological sensing, computation and communication of the sensed data to the user and, in some cases, provide treatment, like stimulation. Advancement of CMOS processes and increased integration has brought to us devices with enhances performance, speed, reduced power and small size that can be implanted in the body. This increasing number of smart sensing devices in our everyday life, especially implants, has brought into light two of the main challenges that are currently holding back this technology from becoming truly pervasive.

While the devices and the sensors are shrinking in size, the batteries and cables associated with them are shrinking at a much slower rate or are not getting any smaller at all. The roadblocks associated with using batteries and cables to power and communicate with these devices are currently a concern that overshadows the benefits of miniaturization. Cables tether the device and restrict mobility. When implanted inside the human body, the cables that exit the body can cause exit site trauma or infections. Batteries, in their current form, occupy more space than the electronics themselves and make the sensing devices large and bulky. Fig. 1.2 shows a wearable device used for health monitoring and an implantable device used for treatment of chronic heart disease. The battery, in both these devices, occupies more than 50% of the device size. The operation of these devices also

has to be interrupted for recharging or replacing the batteries which poses a challenge when continuous monitoring is necessary. Especially in case of implants, where surgical procedures are required to remove or replace the batteries. Moreover, batteries have a limited lifetime and their capacity reduces over time. Maintaining billions of these devices and their batteries to recharge or replace them poses a large economic impact. In addition, batteries also have a negative environmental impact, where these devices end up generating billions of dead batteries that need special recycling.

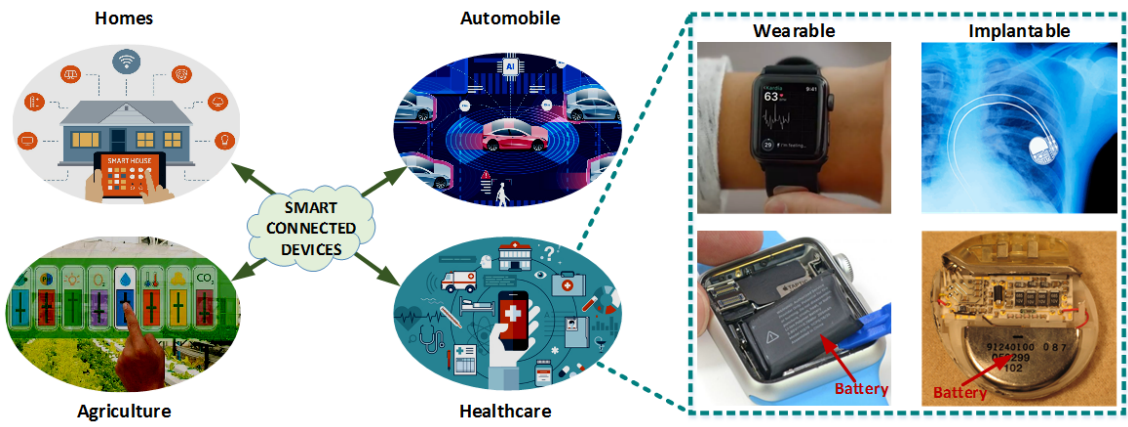


Figure 1.2: Amongst applications driven by smart connected devices, healthcare is currently facing a road-block with device size and energy requirements. In both wearable and implantable devices, the use of cables and large batteries to communicate with and power them are posing a limitation on their size, safety and performance.

The focus of this work lies in addressing the challenges of power delivery, communication and computation to reduce power consumption in biomedical devices. The system requirements for biomedical devices depends on the sensing application they are developed for. Hence these requirements and challenges, along with the contributions in this work to address them, are highlighted with respect to one wearable and one implantable application.

1.1 RF Bandaid: An ultra-low power wearable biosensor

The wearable RF Bandaid operates with ultra-low power consumption at less than $160 \mu\text{W}$ to perform sensing and communication of sensed data. It is envisioned to be a fabric-like tiny platform that is simple, inexpensive, battery-free, wireless and comfortable [2]. Typical wireless sensing platforms consist of blocks for sensing, digitization, computation and communication. The RF Bandaid is developed as a fully-analog platform for sensing physiological signals. All computation and processing of the sensed data is performed in an external centralized processor that has less restrictions in terms of power and resources. Thus the platform is left with only the sensing and communicating tasks which are implemented using analog circuit design techniques. The sensed analog signal is communicated using low power backscatter technique that leads to a 100 times power reduction in comparison to conventional radios [3]. The key to this implementation lies is in the mapping of sensed data into frequency modulations that are communicated as RF backscatter modulations.

The simplicity of the RF Bandaid makes it battery-free, passive and capable of operating at power levels as low as $35 \mu\text{W}$. Owing to this small power budget, the device can harvest energy from UHF signals and operate continuously at ranges greater than 10ft and communicate data to receivers at a distance of 30ft. Unlike the bulky commercial sensing devices and smart watches, this device can be worn all day long to continuously sense without interfering with everyday tasks. The device is battery-free, which makes it small in size and inexpensive to develop. Existing work in the field of on-skin electronics like [4] and [5] also shows that the social stigma and unwanted attention associated with medical devices can be overcome by using such simple devices designed to be aesthetically enhancing, like tattoos [6].

1.2 Brain-Computer-Spinal Interface: A Low-Power Implantable Neural Interface

Following the ultra-low power wearable device, the second contribution is an implantable, low-power, wireless neural interface device. This device is developed to sense and func-

tion as an implant for reliable monitoring and treatment of chronic conditions. Unlike the wearable device, the implantable device needs to be smart and capable of performing some local computation to function without depending on an external controller. The commercial applications that drive research in the field of neural interface devices are a general need to understand how the brain functions and to develop brain-controlled devices. The other application lies in the medical field, where neural interface devices can be used for treatment of various neurological disorders like epilepsy and paralysis due to spinal cord injury. More recently, the pharmaceutical industry is looking at peripheral nerve stimulation as an alternative to drugs for treatment of chronic disorders like arthritis [7] [8].

In this work we develop the brain-computer-spinal interface (BCSI) device for application towards treatment and rehabilitation of patients paralyzed by spinal cord injury. In an uninjured person, intentions that arise as neural signals in the brain (e.g. intention to move an arm) typically travel down the spinal cord and reach the organ of interest (i.e the arm) and perform the action (i.e. movement). In a person with an injury in the spinal cord, there is a break in the connection between the brain and the organs which leaves the person paralyzed. Therefore, a means to bypass this injury and reanimate the paralyzed arm requires the following three fundamental operations. First, recording neural signals from the brain (motor cortex) . Second, decoding the intention (e.g. intention to move the arm). Third, stimulating in the spinal cord, beyond the injury, to activate neurons and trigger action.

With respect to recording, some of the most prominent works focus on developing the electrodes that interface to the neurons and acquiring the signals using these electrodes [9] [10] [11]. With respect to stimulation, electrical current-based or optical stimulation can be used to trigger the activity or block the activity of a population of neurons [12] [13]. In the case of treatment for spinal cord injury, stimulation in the spinal cord beyond the break can be used to reestablish the broken connection [14]. In the case of Epilepsy, recording in the brain to identify irregular activity that indicates seizure onset can be used to trigger stimulation that blocks the seizure itself. The ideal treatment solution for such neurological

disorders requires the ability to record and stimulate, but in addition the neural interface device should also be capable of processing the recorded signals to identify the intentions and trigger stimulations. Thus, the third and the most important component that is required for closed-loop neural interface devices is the computation capability. Existing work includes innovation in algorithms for processing neural signals and implementing closed-loop devices for treatment [15] [16]. Such system, however, are implemented using large benchtop setups or depend on an external computer for processing [17] [18].

Table 1.1: Summary of ISM Band Limits

Frequency (MHz)	Center Frequency	Bandwidth	Field Strength
6.765 - 6.795	6.78 MHz	30 kHz	100 μ V/m at 30 m
13.553 - 13.567	13.56 MHz	14 kHz	15,848 μ V/m at 30 m
26.957 - 27.283	27.12 MHz	326 kHz	10,000 μ V/m at 3 m
433.050 - 434.790	433.92 MHz	1.74 MHz	11,000 μ V/m at 3 m
902 - 928	915 MHz	26 MHz	500 μ V/m at 3 m
2400 - 2500	2.4 GHz	100 MHz	500 μ V/m at 3 m

One of the contributions in this work implement electrical stimulation of neurons using a low-power and miniaturized circuit board that operates at less than 250 mW. This work also demonstrates a novel simultaneous dual-band wireless operation for power delivery and data communication to make the device free of batteries and cables. The device harvests energy from a wireless near-field link at HF 13.56 MHz to meet the 250 mW device power budget. Based on limitations by the FCC listed in Table 1.1 this band was chosen for its efficiency in power transfer, but is not optimal for communication due to bandwidth limitations [19]. To meet high data rate requirements in the order of several Mbps, UHF backscatter communication at 915 MHz is used. Finally, the BCSI device developed in this work is also capable of recording neural signals from the brain, low-power processing on

an FPGA and triggering stimulations that can relay the intention into action. The results from testing the neural stimulation device in-vivo to demonstrate reliable dual-band wireless operation, and the ability of the BCSI device to record and process neural signals to trigger stimulation are presented in the following chapters.

1.3 Thesis Organization

The contributions of this work with respect to the applications described so far are organized in the following chapters as summarized below:

- Chapter 2: This section provides a brief introduction to wearable sensing and backscatter communication for low power communication. Following this, a system-level description of the RF bandaid along with an evaluation of its operation in various use cases and design principles that facilitate them are provided. The results from testing the RF Bandaid for long range operation at ultra-low power consumption and sensing with various passive sensor modules (audio, pressure and temperature) are provided. This chapter concludes with limitations of this work along with future directions that can enhance this design or benefit from it.
- Chapter 3: An introduction to the challenges and requirements of an implantable neural interface device are provided in this chapter. The detailed design and characterization of the dual-band simultaneous wireless power transfer and backscatter communication are also presented. In-vivo test results applying the dual-band system for intra-spinal stimulation, targeting treatment and rehabilitation of spinal cord injury, are also provided.
- Chapter 4: Having laid out the foundation for simultaneous dual-band operation to communicate data and deliver power, this chapter addresses the need for high data rate communication in neural interface devices. The contribution here highlights the implementation of an FPGA-based backscatter protocol that achieves 6 Mbps uplink

communication rates in the near field. This section also presents the experimental validation of dual-band operation with low interference while communicating at several Mbps data rates.

- Chapter 5: This chapter introduces a means to localize the implantable device in the near field without any circuit overhead dedicated to localization on the device. The system level development of a phased-array wireless power transfer system that can locate the receiver and deliver focussed power to it is discussed in detail. The operation of the phased-array system is experimentally demonstrated with respect to a 2D localization and power delivery.
- Chapter 6: This chapter presents the contributions in neural signal processing developed on the BCSI device to enable closed-loop operation. The need for local processing on a neural interface is addressed here with the implementation of a miniaturized FPGA-based Neural Closed-Loop Implantable Platform (NeuralCLIP) that can record and process the neural signals, to decode intent, at low power consumption. This chapter provides a detailed description of the design and architecture of the NeuralCLIP and a characterization of its capability with recording and processing neural signals. The application demonstrated here is used to detect action intent from local field potential signals, recorded in the motor cortex of a rodent, which can be used to trigger stimulation.
- Chapter 7: A discussion and analysis of low-complexity processing for neural spike signals that can be implemented on an FPGA-based wireless device is provided in this chapter.
- Chapter 8: This chapter summarizes the contributions in this thesis and provides a discussion of future directions for these wireless biomedical devices.

Chapter 2

Wearable Sensor Platform: The RF Bandaid

2.1 *Introduction*

The first ever passive radio frequency (RF) sensor was the "Great Seal Bug" listening device invented by Leon Theremin in 1945. The Great Seal Bug demonstrated wireless sensing with a passive cavity resonator connected to an antenna for transmitting sound [20]. The Great Seal Bug inspired the creation of modern RFID systems that come with microprocessors which enable digital communication and on-board computation [21] [22] [23]. Digitization and transmission of digital data provides reliable sensing with better noise tolerance than the simple transmission of amplitude modulation employed by the Great Seal Bug. These digital platforms are great for applications where a smart sensing device is necessary to sense, compute, and perform certain tasks. However, these advantages come with a power budget, device area, and cost tradeoff – in addition to the need to configure the device for specific applications and sensors.

Using 1940s technology, Theremin was able to achieve a wireless, fully battery free, passive, and difficult to detect audio sensor. Motivated by these appealing properties, we looked at the current state of the art in battery free wireless sensors; we found that most approaches focused on utilizing digital logic on the remote sensing portion of their system and/or attempted to build on standards compliant protocols such as RFID. While digital communication has advantages and standards compliance enables the use of off-the-shelf equipment, we realized that there was an opportunity to learn from Theremin's device and use some of his techniques to build a system with a different set of trade-offs/advantages.

Our work is motivated by the need for a wearable, compact, flexible, and potentially one-time use (disposable) sensing platform which could be used in physiological sensing applications such as home monitoring. This work uses three take-aways from Theremin’s Great Seal Bug:

1. Added complexity on the infrastructure/receiver is acceptable if it imparts positive attributes to the wearable sensor
2. Standards compliance is not critical with the increased availability and commoditization of Software Defined Radios (SDRs)
3. Digital components are not a requirement for a wearable sensor (they impart advantages but are not necessary); analog signaling is appropriate and advantageous if you are willing to accept some trade-offs

These three ideas allow us to envision a much simpler wearable sensor. Our work is less concerned with widespread adoption and more with enabling new use-cases, rapid prototyping, and exploring use-cases where the trade-offs of a simpler wearable sensor design are advantageous enough (i.e. enabling a reduced physical size/reduced power consumption) to offset the limitations. Limitations are discussed in Section 2.5, system designers will need to weigh the advantages of a simpler analog system with the disadvantages and decide whether an RFSP-like system is appropriate for their application.

While RFID based platforms still serve a number of use cases, we found that there was significant scope for improvement in terms of size, components count (essential to make it ‘disposable’), and power requirements by exploring more analog solutions that offload computation to an AC powered receiver. Analog operations are appealing because they reduce the required operating power on the wearable sensor. Lower operating power correlates to increased range without any additional energy storage. Our device has roughly 3-5x the range of similar digital backscatter devices with the same transmit power level [21] due to its lower operating power requirements. In this paper, we present a complementary

fully-analog RF Sensing Platform (RFSP) which can interface to a variety of sensors and which maps sensed data into direct frequency modulation, that are backscattered to the Receiver Processing Unit (RPU). This approach has two main goals:

1. Moves digitization and computation overhead from the sensing device (RFSP) to the remote RPU - which saves complexity, cost, area, and power on the sensing device.
2. Using frequency modulation to encode and transmit data makes it more tolerant to noise and attenuation in comparison to transmitting the data using direct amplitude modulations.

We believe that the analog sensing and backscatter approaches presented here, although not novel (in light of use by surveillance agents for many years and designs being closed-source) have not received appropriate attention by the sensing and IoT community. Backscattering analog signals with frequency modulation is a complementary approach to traditional digital backscattering approaches. We believe this method allows us to create a flexible platform which can be interfaced to a number of analog sensors (resistive or capacitive). The RFSP presented in this work is currently designed as a development platform. By presenting a detailed account of the RF architecture, component choices, trade-offs, and presenting evidence of its superior functionality we are confident that we can enable follow-up work that benefits from flexible, ultra-low power, small, and battery-free ubiquitous sensing.

Applications that require continuous monitoring (like wearable measurement of physiological signals, temperature monitoring in food/pharmaceutical industry, etc.) benefit from small, flexible low-power devices. Specifically, for applications such as continuous bedside monitoring of physiological signals we need a device that is not only small but comfortable to wear. Our device is configured for a power budget under $200 \mu\text{W}$ for sensing and data transmission. This enables it to be powered by the energy harvested from the incident UHF signal. The bedside monitoring scenario in this case would require a dumb omni-directional transmitter that transmits the UHF continuous wave (CW) signal. The device worn by

the patient (envisioned as a disposable fabric band-aid with a tiny circuit board) harvests energy from this signal to perform the sensing and backscatters the sensed data as subcarrier modulation on the UHF signal. This modulation is picked up by a sensitive receiver (the RPU) which could be incorporated into a bedside device (i.e. a bedside clock). The RPU servers as the hub for digitization and processing of data to display the sensed data to care-providers. The TX and the RPU are a one-time installation, while the wearable device is a flexible, low cost (potentially one-time use) bandaid-like device and which uses the same analog system for different sensing applications. A block representation of this RFSP is provided in Fig. 2.2.

To understand the RFSP better, Section 2.2 provides a detailed description of the system design and theory of operation. An analysis of different sensing scenarios and design choices is provided in Section 2.3. This is followed by results from sensing measurements using the RFSP and an analysis of power consumption and range of the device in Section 2.4. Finally, a discussion on limitations, related work and methods to address challenges, potential applications and future design improvements is covered in Section 2.5 and Section 2.6 provides conclusions to summarize our work.

2.2 System Design and Theory of Operation

2.2.1 RF Sensing Platform Description

There are four main design and operational constraints that we optimize our prototype of RFSP for. First, it should map the sensed signal directly to a frequency modulation. This is what primarily makes it an analog sensing platform. Second, use this modulated frequency to drive an antenna to produce the backscatter effect. In particular, this involves use of an RF switch that is toggled at the desired frequency to produce a subcarrier modulation that rides on the incident UHF signal. Third, to power the sensing, frequency generation and RF switching, energy is needed. This is accomplished by harvesting energy from the incident UHF signal. Finally, to ensure a large practical operational range, the overall power budget needs to be kept low.

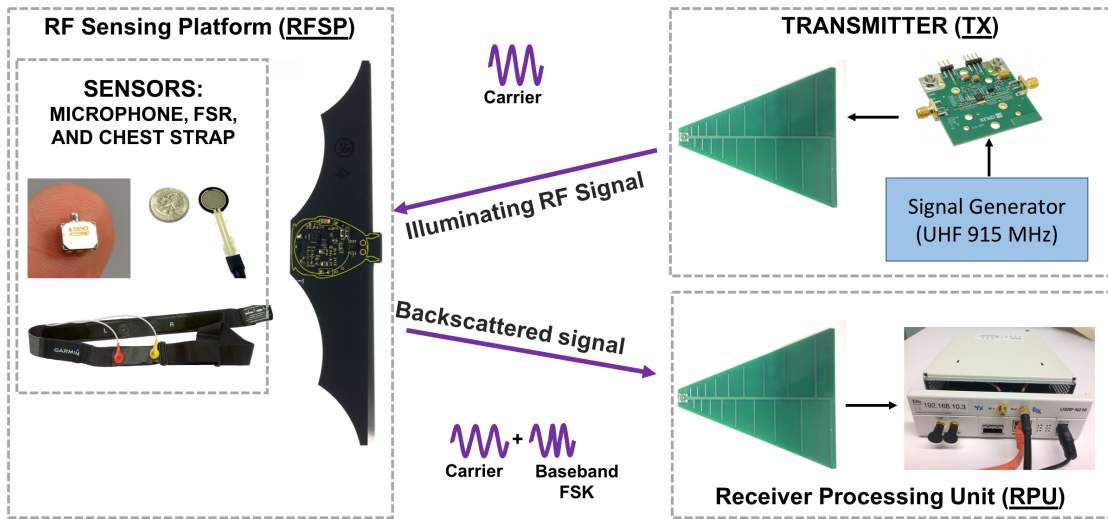


Figure 2.1: A system description of the RF Bandaid system with the transmitter and the receiver processing unit (RPU) on the right side and the RF sensing platform (RFSP) with its sensors on the left. The receiver side (the RPU) consists of an Ettus Research N210 Software Defined Radio (with SBX daughterboard) which acquires the backscattered signals. All processing of the backscattered signal is performed on a computer that controls the SDR. The transmitter (TX) side consists of a 915 MHz signal source and a RFMD RF6886PCK-410 linear power amplifier. TX side is a dumb device which outputs a continuous wave (CW) at 915 MHz to provide backscatter power and the carrier signal. The RFSP harvests power from the TX side and maps signals sensed by a resistive/capacitive sensor into a modulated frequency output which is backscattered on the carrier signal. This signal is received and processed by the RPU to display sensor data to user.

Before we discuss system specific component choice and optimizations, we briefly describe the operational principle behind a backscatter device. Consider the Great Seal Bug. It was a mechanical cavity resonator with an antenna such that when energized by illuminating it with a continuous wave RF signal, the specially designed cavity's capacitance and the antenna would form a tuned RF frontend. Any changes in the cavity (and hence its capacitance) caused a 'detuning' of this resonance structure. When sound waves fall on the cavity and create a vibration, these vibrations are encoded as a series of capacitance changes and hence a time-varying detuning of the antenna that results in reflecting a slightly varied signal than the original illuminating RF signal. In effect, any sound expressed on the cavity resonator was directly mixed into the illuminating signal and reflected back as an amplitude modulated (AM) signal. Here, the Great Seal Bug resonator acts as a mirror that reflects (hence, the term backscatter) the illuminating source at different frequencies instead of generating its own source for response. This electronics-free operation allowed it to function with only a mechanical cavity and remain undetected for seven years [20]. Backscatter principles have now been adapted as a communication method for several RFID based sensing and computation systems. Compared to active radio communication, where the sensing device generates the UHF carrier for data transmission, this method (employed by backscatter systems such as RFID) has 100x reduction in power consumption (with devices ranging from several 10s of mW to less than 200 μ W) since there is no active generation of the UHF carrier signal [24] [23].

In the RFSP, the varying signal and the detuning (or the signal mixing) of the antenna is implemented using a tunable oscillator and an RF switch. The time varying signal we generate is a frequency modulation such that the frequency varies as a function of the sensor input. For instance, for a resistive pressure sensor, as the resistance decreases with pressure, the frequency increases. The key component that enables this function is a low cost micropower precision programmable oscillator (MPPO) from Linear Technology LTC6906 [25]. This device can be configured to convert a varying resistance at sensor output

to set its output frequency. It maps a resistance change in range of 100 kOhm to 1 MOhm into frequencies in range 1 MHz to 10 kHz.

To drive the antenna, we toggle an RF switch across the antenna that acts like a mixer to modulate its switching frequency on top of the incident 915 MHz carrier wave. The communication front end on the RFSP uses the ADG902 reflective wide-band switch from Analog Devices [26]. We chose this particular part because it operates with an ultra-low power consumption and low quiescent current (max 1 μ A). As an added advantage, this analog switch also has low insertion loss (-0.8 dB) and high isolation (-40 dB) properties at 915 MHz. For the RF switch to effectively backscatter, the RF frontend needs to be tuned at 915 Mhz. We accomplish this using a L-matching network that consists of a capacitor in parallel from antenna to ground and an inductor in series.

To interface the sensors that modulate the oscillator, we first use a 100 kOhm resistor to set the minimum required resistance (R_{SET}) at the frequency set pin (SET) of the MPPO and add the sensor in series to it. The next step is to calibrate the resistance change of sensor (R_{Sense}) to vary between 1 kOhm and 900 kOhm with a step resolution of at least 500 Ohms. The limit on the resolution depends on resolution of the ADC on the RPU and its sampling rate. Limiting different sensors to specific variation range in R_{SET} lets us allocate separate channels to different types of RFSP that might be associated with a single RPU. The SET pin on the MPPO is at 650 mV and acts as a current sink to an operational amplifier that sets the master output frequency of a internal voltage controlled oscillator (VCO). This frequency is then divided based on the configured ratio. This pin also has a precision internal capacitance of 10 pF that combines with $R_{SET}(100KOhm + R_{Sense})$ to set the oscillation frequency. The output of this MPPO drives the gate of the RF switch for backscattering.

The MPPO IC can operate at a DC voltage range of 2.25 V to 5.5 V, while the RF switch can operate between 1.7 V to 2.75 V. To provide a supply for these two components a Texas Instruments BQ25570 Nano-power buck-boost IC is used to harvest and buffers the small amount of energy for operation in through a small ceramic capacitor ($\sim 50 \mu$ F) [27]. The

DC-DC conversion module also has a low dropout regulator which is set by divide resistors to regulate a 2.3 V supply to power the components on the system. BQ25570 was chosen for its ultra-low cold start voltage (330 mV) and high efficiency (greater than 85%) for the power levels being harvested in this application. The IC also provides the means to charge a small battery if this feature becomes necessary for future application-specific instantiations of the RFSP. This design flow is summarized in the block diagram provided in Fig. 2.2 The specific components for RFSP design were carefully selected to maximize sensing ability while minimizing the cost, area and power consumption. This also helps eliminate the need for a large storage device which makes it possible to develop small, flexible and low cost devices.

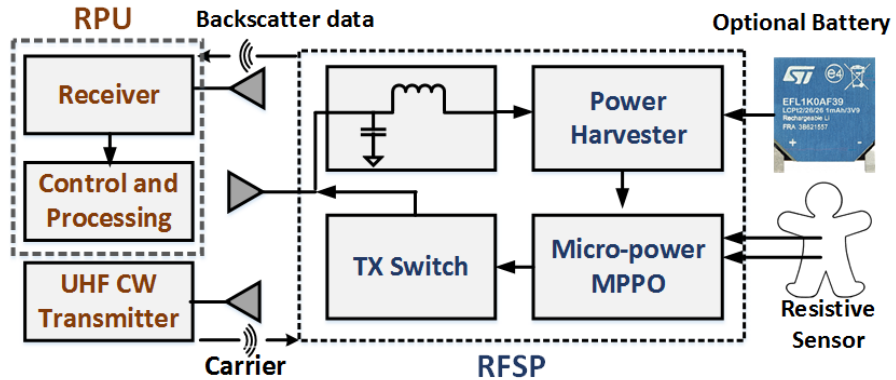


Figure 2.2: A block representation of the RF Bandaid system. The RPU and transmitter are shown on the left (RX & TX) and a detailed block diagram of the RFSP is shown on the right. Power from TX is harvested by the RFSP through its front end and power harvester. The power harvester will store charge in a small ceramic capacitor until the capacitor voltage exceeds it's set threshold. Once this threshold is reached (currently set to 2.6 V with a hysteresis at 2.4 V—that is, charging doesn't resume until capacitor voltage is below 2.4 V), the power harvester enables a low power LDO or supplies power directly into a resistive sensor (depending on the system designers needs). As the resistive sensor changes, it modulates the output of a low power VCO (MPPO) which controls the gate of a TX switch. This modulation encodes the changes in resistance into a "carrier + sensed FSK" radio signal which is picked up by our receiver path (an SDR in our current system).

2.2.2 MPPO Configuration

The LTC6906 is a micropower resistor set oscillator which allows its output, f_{out} , to vary between 10 kHz and 1 MHz depending upon the resistance at R_{SET} . It's output, f_{out} , is generated by an internal 1 MHz master oscillator which is followed by a frequency divider which operates according to the following formula:

$$f_{out} = \frac{1MHz}{N} * \frac{100kOhm}{R_{SET}} \quad (2.1)$$

The R_{SET} value determines the master oscillator frequency while the DIV pin sets a division ratio N . For the LTC6906, R_{SET} must be 100 kOhm at a minimum and 1 MOhm at the maximum. The operating range of f_{out} output can be configured for a specific band in this 10 kHz to 1 MHz frequency range by setting a resistor-set clock divider, N . With the master clock of the MPPO fixed at 1 MHz, f_{out} output is calibrated for operation within:

- 100 kHz to 1 MHz by using a clock divider ratio set to 1 [$N = 1$]
- 33.3 kHz to 333.3 kHz by using a clock divider ratio set to 3 [$N = 3$]
- 10 kHz to 100 kHz by using a clock divider ratio set to 10 [$N = 10$]

For any given frequency the power can be minimized by reducing the master oscillator frequency (maximize R_{SET}) and using the lowest possible clock divider ratio ($N = 1$). Specifically, if R_{SET} is at the minimum 100 kOhm, the master oscillator output is at 1 MHz (output is at 100 kHz for the maximum 1MOhm). By setting the clock divider ratio to 10 ($N = 10$), this 1 MHz signal is divided, by 10, to 100 kHz and provided as MPPO output. This setting accounts for a maximum current draw and the RFSP has been characterized for this maximum current draw setting. The measured minimum power consumption of the RFSP is 35 μ W when $R_{SET} = 1$ MOhm and a divide ratio of $N = 10$ are used. The maximum RFSP power consumption was tested to 160 μ W when the R_{SET} was fixed set to 100 KOhm with $N = 10$.

- To interface sensors with resistive variation in 100's of kOhms to MOhms, the actual sensor interface has a 1 MOhm base resistor ($R_{Baseline} = 1$ MOhm) across the SET pin and R_{Sense} is added in parallel to it (this sets the minimum frequency to 10 kHz without any sensor). As R_{Sense} varies, the R_{SET} value decreases. Thus increasing the R_{Sense} value results in an increase in the MPPO output frequency, up to 1 MHz.
- For sensors with resistance values in the 10's of kOhms, we use a $R_{Baseline} = 100$ kOhm to set the minimum required resistance on the MPPO SET pin. The R_{Sense} value is added in series to this baseline resistor, $R_{Baseline}$. $R_{Sense} = 0$ corresponds to an MPPO output frequency of 1MHz. In this case, increasing values of R_{Sense} correspond with a decrease in the MPPO output frequency, down to 10 kHz.

The current consumption of the MPPO can be calculated using the following equation.

$$I^+ = 5 \mu A + (6 * \frac{V_{SET}}{R_{SET}} + V^+ * f_{out} * (C_{load} + 5 pF) + \frac{V^+}{2 * R_{load}}) \quad (2.2)$$

Specifically, for the RFSP $V_{SET} = 0.650$ V and C_{load} is 2 pF at 1MHz from the ADG902 switch input specifications. With an operation voltage of $V^+ = 2.3$ V, the value for I_{MAX}^+ is around $61.25 \mu A$ ($140.87 \mu W$) and I_{MIN}^+ is around $11.6 \mu A$ ($26.68 \mu W$). These computed values correlate with the overall power consumption that was measured on the RFSP with a minimum of $35 \mu W$ and a maximum of $160 \mu W$. As evident, the MPPO is the largest power consuming component in the RFSP.

2.2.3 Receiver Processing Unit

Since the sensor is designed to harvest energy and communicate data using a 915 MHz front-end, the setup requires a 915 MHz continuous wave transmitter (TX). This can be a standard signal generator or a programmable transmitter module connected to a 915 MHz antenna and can provide sufficient power. The receiver (RX) must be capable of picking up the backscattered signal and also perform the necessary computation as a back-end. Since this is the smarts of the setup, we implemented it using a USRP N210 software defined radio

(SDR) module from Ettus Research [28]. This setup uses a SBX daughterboard (400 MHz to 4400 MHz band) where the RX2 port was configured to receive the backscattered signal. A GNU radio user interface controls the USRP for receiving and processing the data. A python script was used to process the received data and obtain sensed measurement results. The USRP module is capable of more than 40 MHz sampling speed at its ADC, which sets the resolution limit for the sensed signal. We have tested the USRP with 10 MHz sampling rate while processing data in real-time. For our test applications which primarily involve lower frequency signals, we used a 1 MHz sampling rate which supported real time processing and data viewing with GNU radio running on a Lenovo Thinkpad T530.

With our 1 MHz sampling rate we can resolve R_{SET} step variations that are 500 Ohms. For applications which require a higher resolution of R_{SET} (steps variation that are smaller than 500 Ohms). Smaller R_{SET} step variations translate to smaller variations in MPPO output frequency. System designs can perform two optimization, to improve the system. Firstly, improving the sensitivity of the RPU and second, using higher sampling rates at the receiver ADC for better temporal resolution. A higher sampling rate at the receiver unit (for example, the USRP's maximum 40 MHz) allows for a higher temporal resolution of the received signal (versus the 1 MHz sampling rate currently used), allowing the system to track smaller variations in MPPO output frequency. Higher temporal resolution also allows for finer time resolution.

2.3 Application-Specific Design Options

Range is typically one of the most important parameters for backscatter systems. We have tested the range of the RF Bandaid system with the transmitter (TX) output power set at 26 dBm (390 mW) to be around 4 meters with no duty cycling (that is, the backscatter tag has surplus power and continuously operates) and 2.7 meters with the TX output power at 23 dBm (200 mW), again with no duty cycling. Beyond these ranges the sensor begins to consume more power than it receives and has to duty cycle: turning off to store enough charge before continuing operation. Increasing the range further causes the sensor to drop

out completely. Duty cycling of the RFSP allows the sensor to continue to provide useful output. During duty cycling, the RFSP waits until it has enough power to start then begins to perform frequency modulation until it no longer has enough power to operate. The RPU sees this as a reflected signal appearing and then disappearing when the RFSP duty cycles off. In our range tests we used commercial log-periodic 915 MHz antennas for TX and RX, and output power was limited to a max of 26 dBm due to an equipment limitation, the FCC limit of 1W (30 dBm) would enable a bit more range between TX and the sensor. The RFSP tag has a half-wavelength dipole antenna shown in Figure 2.1 along the wing edge of the bat shaped board. The receiver side antenna (RPU) was placed approximately 10 meters away from the TX antenna and both were not moved during testing, instead the sensor was moved further away from the TX side to test the range.

2.3.1 RX Placement and RX/TX Antenna Configuration

One interesting property of decoupling RX and TX is that the RFSP is more sensitive to the distance between the sensor and the TX power source (the sensor needs enough TX power to operate). The RX side has more than enough sensitivity so the limiting distance in our system becomes how close the TX power source is to the RFSP. If we place the RFSP close enough to the TX power source so that it has enough operating power we can move the RX antenna much further away (in our tests at least 9+ meters) into another room and still receive data. Because our system only needs a CW transmitter, the TX power sources are much cheaper and simpler (a 915 MHz RF signal source + optional amplifier + antenna) allowing us to distribute TX antennas around while having only a single or a few more complex and expensive RPUs. This allows in a standard home setup to centrally place a high-gain RPU and to distribute dumb TX units around the entire home to power RFSPs throughout the home.

2.3.2 Operational Range

As with a typical TX-RX setup, the transmitted UHF signal attenuates with distance, governed by Friis path loss equation. Hence, the closer the device is to the TX, the stronger its backscattered signal and the more power that is available for continuous operation. In the applications described so far, a small capacitor is sufficient to smooth out fluctuations in power availability when the TX side is relatively close-by. When the device is further away from TX, it does not receive sufficient power to perform the sensing task. Also, the signal is backscattered on a much smaller amplitude carrier. As the device moves away, it starts duty cycling between being on and off based on power availability. There are four different ways of improving the operational range of this device;

- Move device closer to TX: In some applications, if range permits, having the device close (within 0.5 meters) to the TX allows for more power availability and the RX can be moved further away.
- Increase TX power: We tested the device for range using the 915 MHz log-periodic antenna at TX and a whip antenna at the RPU placed 10 meters apart and moved the device away from the receiver until it started duty-cycling. This distance was recorded to be 3 meters for 23 dBm, 3.6 meters for 24 dBm, 3.8 meters for 25 dBm and 4 meters for 26 dBm. With this diminishing return due to path loss, increasing transmit power is not an ideal resolution.
- Using a battery: To extend the range further we tested the device in the same setting with battery power (a $160 \mu\text{m}$ thick ultra-thin battery), and 26 dBm at the TX. We observed continuous operation on the device up to 8.8 meters away from the TX.
- Better antennas: We have used simple commercially available antennas for our generic tests. Using application-specific high-gain antennas would enable sensing at further distances as well as better transmission of power and harvesting.

Even though one of the strengths of our system is that it does not require a super capacitor or battery for an energy storage device, it is capable of operating with a battery. For system designers or applications where a battery is acceptable or where the added functionality is worthwhile, batteries are an interesting operating mode. Because the RFSP consumes very little power, a system designer can always choose to add in a small primary cell or rechargeable battery to increase the operating range or reliability of the system. This can be useful for two reasons 1) situations where backscatter power cannot supply enough power for a power hungry sensor and the battery source is used to keep such a sensor running 2) to bridge any gaps in TX coverage to allow for continuous operation. The 2nd option is useful for our proposed monitoring application because our low power draw means we can make use of ultra-thin film rechargeable batteries (such as the ST Microelectronics EFL1K0AF39 [29] which has a paper thin $160\ \mu\text{m}$ total thickness, rated for 1 mAh at 3.9 V). Because we only draw power from the battery when TX received power drops below our power consumption, we normally would consume very little battery current. It should be noted that such thin and low-density batteries have otherwise limited application scenarios. However, coupled with the low current draw of the analog RFSP, batteries open up application scenarios that would otherwise not be practical. When the RFSP has excess TX power it can always charge the battery, helping to make the system far more reliable if needed. Or for more difficult environments or times of severe body occlusions the battery can provide enough power to allow our system to operate continuously for several hours where it would otherwise need to duty cycle.

2.4 Testing and Results

All tests for the RF Bandaid system were performed in the corridors and rooms of a busy office building with no control over the RF environment (Fig.2.5c). Many common sensors typically involve a change in resistance or capacitance. One of the strengths of this system is that we can easily interface to a wide variety of resistive or capacitive based sensors. The focus of this work is to measure resistive changes that are mapped into frequency modula-

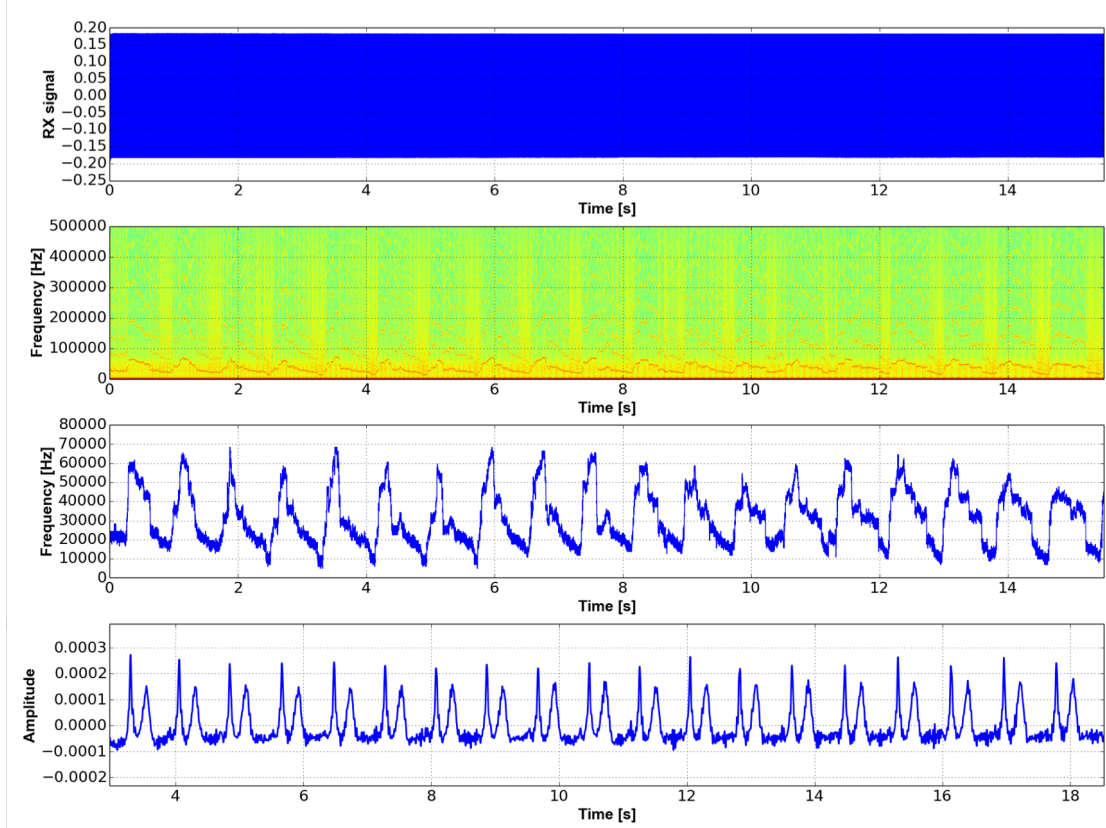


Figure 2.3: Received and processed signals for heart rate sensing. The plots show the raw time-domain signal, spectrogram, the extracted frequency modulation envelop and EKG measured using a medical grade sensor from top to bottom, respectively. The time-domain signal looks like an envelop function due to the dense signal. The spectrogram shows the encoded signals along with the harmonics, this figure is centered at 915 MHz (0 Hz in this subplot is 915 MHz) and shows harmonics visible within 500 kHz of 915 MHz. And finally the bottom two signals are a raw signal extracted from the spectrogram showing the sensor data and the bottom figure is the EKG ground truth measurement. Both show the 19 pulses measured over 15 seconds of measurement.

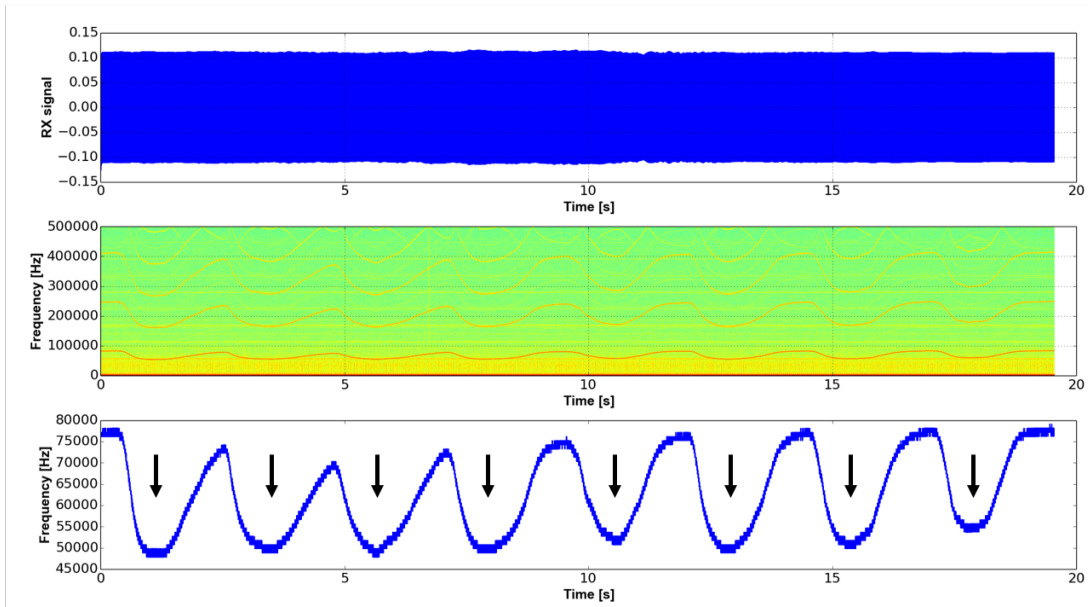


Figure 2.4: Received and processed signals for breathing showing the raw time-domain signal, spectrogram and the extracted frequency modulation envelop from top to bottom, respectively. The spectrogram shows the encoded signals along with the harmonics for the breathing sensor, this figure is centered at 915 MHz (0 Hz in this subplot is 915 MHz) and shows harmonics visible within 500 kHz of 915 MHz. And finally the bottom signal is a raw signal extracted from the spectrogram showing the breath sensor data. The arrows indicate the times at which the user starts exhaling. The breathing rate measured here is 8 exhalations in 20 seconds.

tion for transmission. Capacitive sensors can be used with impedance transformation with circuits such as a common-source amplifier. To demonstrate this we examine three different resistive sensors that measure temperature, force, and stress in this section. To demonstrate the use of capacitive sensors with the RFSP we have also tested the system for transmission of audio signals sensed with an electret microphone. These microphones are typically a capacitive cavity with a FET common-source amplifier. The first test demonstrates the use of body-worn resistive sensors to measure physiological parameters. For example: the heart rate of a person can be detected as a pulse in the wrist, chest or neck. Similarly a piezo-resistive stretch sensor can be used to measure breathing rate with expansion of the chest cavity. Force sensing resistors (FSR) are also used for detection and rehabilitation of patients with carpal tunnel syndrome and for posture correction. Other applications like force measurement in prosthetic limbs can also be measured using resistive force and stretch sensors. To interface these sensors with the MPPO, we have calibrated them to vary in the range of 30 kOhm to 500 kOhm and have configured the MPPO for maximum power consumption.

The signals received by the SDR are first filtered to the desired band where we expect the frequency modulation. The envelop of the frequency modulation signal is then extracted to obtain the sensed value. Measurements for heart rate, breathing rate, and temperature, using resistive sensors, were tested using the RFSP. Their setup and results are provided in the following sections. The heart rate and breathing rate sensors were tested on four volunteers to verify reliable and reproducible operation.

2.4.1 Heart Rate Measurement

The RFSP is first tested to measure heart rate in beats per minute. A typical method to detect pulse rate is from the carotid artery in the neck where a distinct pulse can be felt by placing fingers on the neck to the side of the windpipe. The number of pulses felt is counted over 10 seconds to calculate approximate beats per minute. By placing the FSR (R_{sense}) at the neck we can measure the resistive change that corresponds to heart rate.

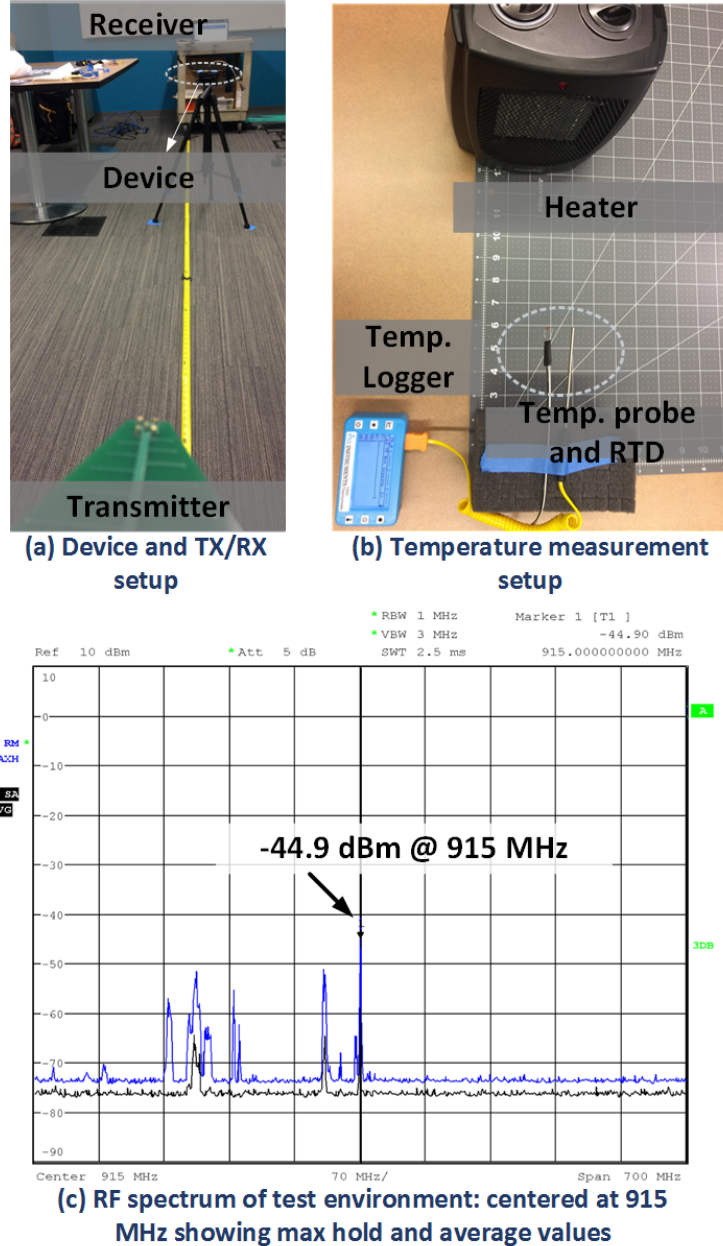


Figure 2.5: The experimental setup with TX, the RFSP and the RX is provided in (a). The RFSP is 2.7 meters away from the TX and the RX is placed at 4.3 meters distance from the TX for these experiments. The test setup for ground truth measurement of temperature along with a RTD sensor that interfaces to our prototype is shown in (b). A heater was used to ramp up the temperature after cooling the sensors to 36 °F. (c) Is a spectrum analyzer measurement showing the RF signals present in the test environment

Three separate trial measurements were taken from four volunteers with our device. To verify this measurement, a parallel study was performed using an industry standard EKG sensor to measure heart rate during the three trials. Fig.2.3(a) shows the received signal, a spectrogram obtained from raw received signal, the measured heart rate signal (as frequency modulation) extracted from filtered signal and finally the EKG recording from the ground truth device. On detecting the envelop of the filtered signal we then extracted the pulse rate of around 19 beats in 15 seconds (76 beats per minute). The measurement from our device shows heart beat rates correlating to the measurement from the ground truth device. Since the RPU is capable of high complexity computation, standard signal processing algorithms can be employed for identifying the heart rates from the received signal.

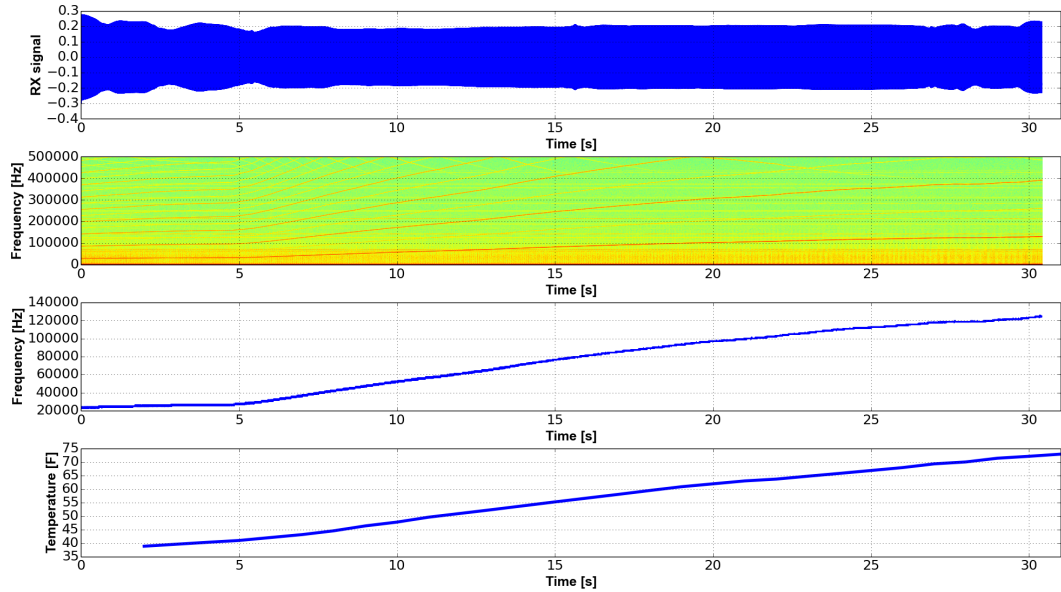


Figure 2.6: Received and processed signals for temperature sensor showing the raw time-domain signal, spectrogram, extracted frequency modulation envelop, and ground truth temperature reading from top to bottom, respectively. Similar to Fig.2.3 we show the time varying RX input signal (which looks like an envelop), spectrogram centered at 915 MHz (0 corresponds to the received 915 MHz carrier), and the extracted temperature signal which corresponds well with the ground truth.

2.4.2 Breathing Rate Measurement

Several state-of-the-art commercial respiratory monitors use a strap/harness around the chest [30] or in the abdomen [31] for measurement. To leverage this expansion in the chest/abdominal cavity to measure breathing we built a custom strap using a carbon doped fabric that changes resistivity as it stretches [32]. The fabric is sensitive enough to register small elongations or contractions which result in resistive changes on the order of several 10's of kOhms for a few millimeters of stretch. This resistance change is added in parallel to a baseline resistance ($R_{Baseline} = 1$ Mohm) that calibrates the MPPO to its fundamental low frequency output and any R_{Sense} variation increases the output frequency as the overall R_{SET} decreases. Fig.2.4 shows the raw received signal, the spectrogram of the received signal and the frequency modulation corresponding to breathing extracted from the filtered signal. The test subjects were asked to perform a button push task on exhalation during the test and the timestamps were used to verify the breathing rate. The exhalation points are marked by downward arrows on the extracted signal. A total of 8 breaths were recorded in the 20 seconds of measurement (24 breaths per minute). Similar to heart rate measurement, more complex algorithms can be used to identify the breathing rate since the RPU is not constrained by power limitations.

2.4.3 Temperature Measurement

To measure non-periodic parameters like pressure and temperature, we use the same technique of transmitting the signals encoded as subcarrier modulation. To demonstrate this we used a standard off-the-shelf resistive temperature detector (RTD) with the RFSP to log temperature changes. We also used a Pax Instruments T400 temperature logger in parallel to log the ground truth data. Both sensors were initially cooled in ice to 36 °F. While logging the temperature, both the sensors were exposed to a space heater that increased the temperature to around 75 °F. The data logged by the RFSP and its respective spectrogram, the extracted frequency modulation and the T400 logger data are provided in Fig.2.5. The

change in frequency corresponding to the change in temperature is observable during the log interval of 30 seconds.

2.4.4 Audio Transmission with Capacitive Sensor

The sensors incorporated so far are resistive in nature and can be directly used with the MPPO. To interface capacitive sensor we must first convert the sensor variation to a varying current draw from the SET pin. This can be achieved by using common source amplifiers that convert the voltage change with capacitance at the gate of a FET into a current draw change at the drain terminal. To demonstrate this we used an electret microphone (EK23024) by Knowels along with the RFSP. The drain and source of the microphone was connected in parallel to the 1 MOhm resistor at the SET pin to ground (as R_{Sense}). The test was carried out by playing a fixed waveform on a mobile phone and transmitting the recorded microphone data by backscattering. The waveform file as well as the received signal were processed and are presented in Fig.2.7 along with the frequency content for each of these signals in the audible range. We also played a continuous sweep of signals between 100 Hz and 5 kHz, white noise, speech and music signals to test the transmission. The processed backscatter signal's spectrum had some aliasing and a constant sound at 800 Hz, but the audio is still legible . These are artifacts created by our $R_{Baseline}$ and can be rectified by design improvements to the sensor interface and/or signal processing.

2.4.5 Device Functional Summary

A summary of the power consumption, range and lifetime of the RFSP paired with each of these sensors are provided in Table.2.1. The table provides sensor specs, RFSP power consumption, measured range with continuous operation at a TX power of 23 dBm and the calculated lifetime for the RFSP when it is augmented with the thin film battery rated 3.9 V and 1 mAh. It is evident that the low-power consumption of the RFSP allows it to function at increased range and can be configured to operate continuously off a thin-film battery for at least one day.

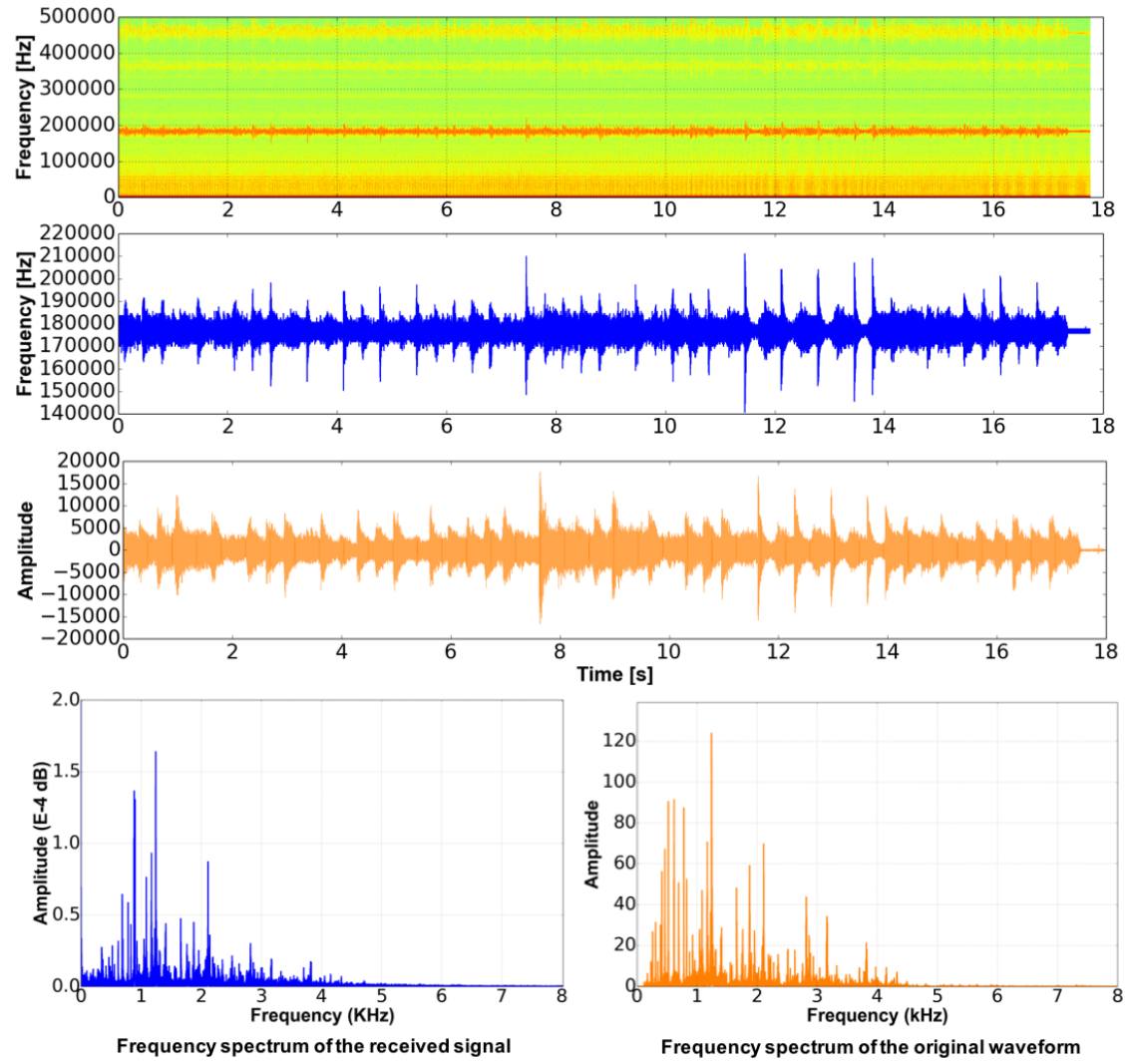


Figure 2.7: Received and processed signals for audio signal transmission showing the spectrogram, extracted frequency modulation envelop representing the received waveform (blue), the original waveform played (orange) and the frequency spectrum of the backscattered (blue) and original waveforms (orange) from top to bottom, respectively. Similar to 2.3 the spectrogram is centered at 915 MHz (0 corresponds to the received 915 MHz carrier). The extracted audio waveform which corresponds with the original waveform. There is some attenuation and distortion in the frequency content when compared to the actual waveform.

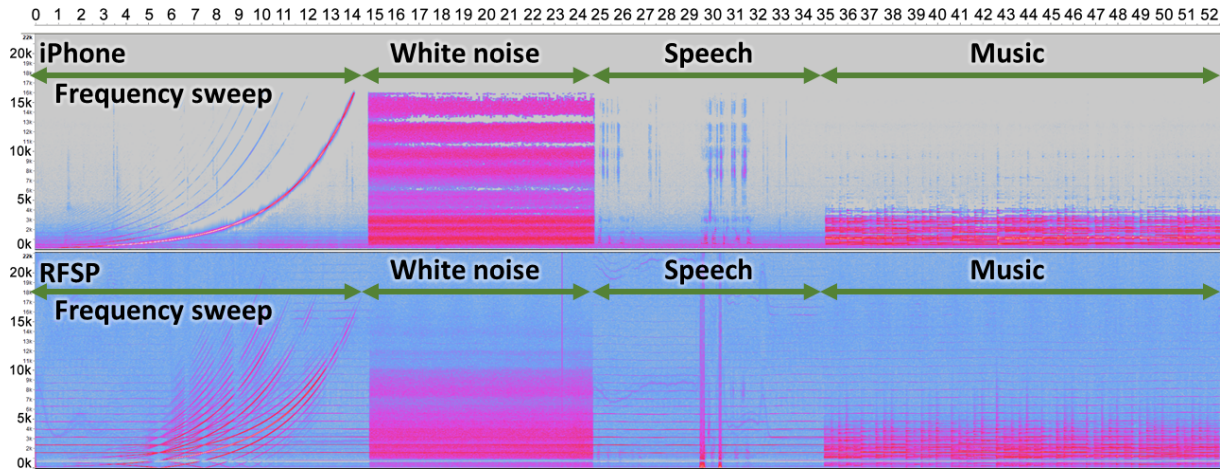


Figure 2.8: Top plot is spectrogram of audio signal recorded with an iPhone and the bottom is the spectrogram of signals from the RFSP. The aliasing and a constant noise at 800 Hz is prominent in the bottom figure.

Table 2.1: Power consumption, range (TX set to 200 mW or 23dBm), range with an on-board battery source (TX set to 200 mW or 23dBm), and the worst case battery runtime for the breathing, heart rate, and temperature sensors

Sensor	Part Spec.	Power Range(μW)	Range w/o Battery	Range w/ Battery	Lifetime w/ Battery(Hrs)
Chest Strap (breathing rate)	BodiTrak Smart Fabric	128 to 158	<3 m	>4.26 m	~8 to 6.5
FSR (heart rate)	SEN-09375	87 to 147	<3 m	>4.26 m	~12.5 to 7
Temp.	254JG1J	87 to 156	<3 m	>4.26 m	~12.5 to 6.5

2.5 Related Work

2.5.1 RFID and Passive Digital Devices

With the availability of low-power computation modules like the MSP430 and STM ARM cortex processors and ability to produce application specific ICs, small devices that can sense compute and transmit data have been developed. Examples of such devices are the EMG telemetry device described in [33] and the early work on accelerometers powered by RF energy harvesting on WISP [21]. These devices have A/D converters that digitize the sensed signals and a state machine to either perform computation or communicate the data out as packets. They perform these tasks at an impressive power budget as low as 1 mW to 2 mW. With the ability to store harvested energy in supercapacitors and batteries, tasks that require up to several 10's of mW can be handled by these devices only restricted to duty-cycling based on power availability (about 25% duty-cycling for the WISP [21] [34]). While these devices come with superior capabilities in terms of sensing and communication, they have more components, consume more power and cost more than a simple design like that of the Great Seal Bug. In this work we try to address the design space between such extremely simple analog sensing device and the more complex digital device. At the same time we demonstrate continuous operation without duty-cycling over a larger physical range with our small power budget (160 μ W maximum).

2.5.2 Hybrid Analog Devices

One of the prior works that addresses the challenge with power and the processing needs proposes a hybrid solution that switches between pure analog operation and digital operation [22]. This work combines the use of a microphone sensor (similar to the Great Seal Bug) with an RFID activation sequence on a WISP. Their analytical model predicts an operational range of 14 ft with the TX power set to 26.7 dBm. In this work we demonstrate the ability of our system to work at this predicted range with lower TX power levels and we also experimentally verify and demonstrate methods to extend the range. Recent work

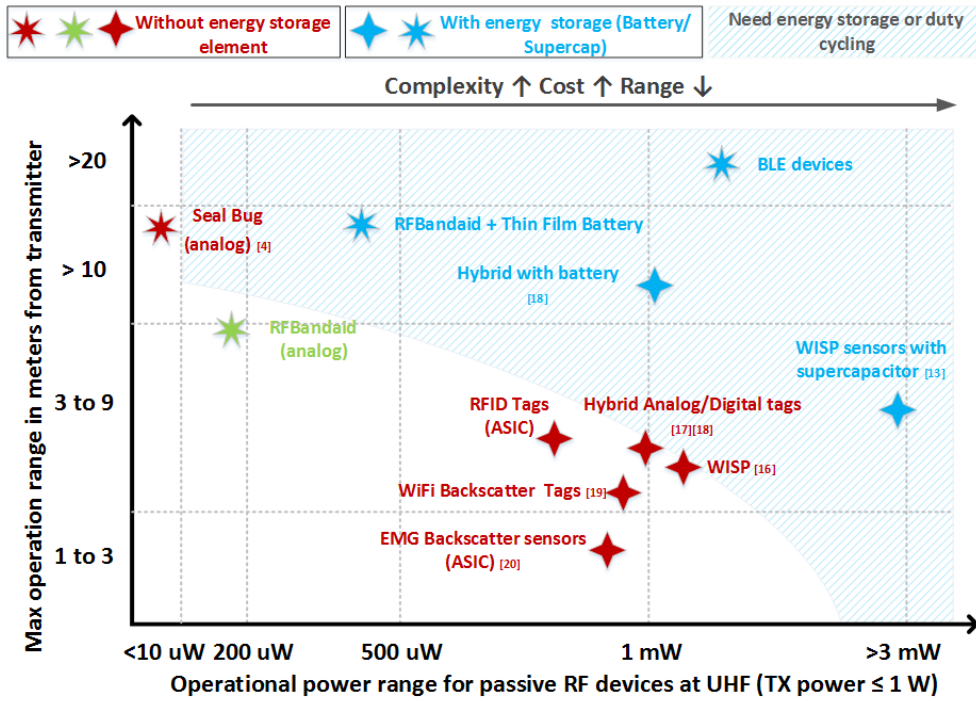


Figure 2.9: Representation of the RF devices based on operation scheme (analog/digital), the amount of power consumed and the range between RF tag and receiver for continuous or duty cycles operation. The X axis shows the power consumed and Y axis shows the maximum range capable. The 4 point stars represent Digital devices and the 7 point stars are the analog devices. Color schemes with red indicate battery-free devices and blue are RF devices augmented with energy storage elements. The shaded region in the chart represents the approximate boundary between range that can be supported with continuous operation of a tag while it uses no battery for a given power level in range.

on hybrid devices has led to the development of a battery-free phone, which uses the hybrid technology to establish a connection through using the RFID based digital communication. Once connected it transmits the sound profile through analog backscatter [35]. This system has also demonstrated low-power operation up to 31 ft with duty-cycling based on power availability. One of the methods to harvest more power suggested here is to harvest from multiple bands of frequencies. However, the conclusion that available power was still insufficient for continuous operation of the existing digital processing supports the need to develop analog systems.

2.5.3 Design Improvements

While the RFSP harvests energy from the 915 MHz continuous wave source, this can also be scaled to other frequencies in the ISM band. The ability to harvest energy from ambient signals like radio, TV and cellular towers and Wi-Fi routers has been demonstrated and their magnitudes are comparable to our power budget [36] [37], [38]. Designing our prototype to harvest energy from different bands would enable powering it using the ambient signals for extended range operation. One of the main challenges with existing single band systems is self-Jamming, where the isolation between the TX and RX is poor and the 915 MHz carrier wave leaks into the receiver module. This becomes a major problem especially when trying to implement the TX and RX on same hardware or close to each other. In either case, the bandwidth and sensitivity for the weak backscattered data is limited due to the presence of the strong carrier signal. One of the solutions proposed for this challenge in [39] is to use harmonic backscatter, where energy is harvested completely from the 915 MHz while a first or second harmonic is used to backscatter the sensed data. Such devices are designed to use nonlinear components to passively generate a harmonic that can be used for backscatter from device. Another related work uses a tattoo mesh sensor that can be worn on the skin for measuring various parameters [40]. This design implements resistive strain gauge and temperature sensors that are capable of converting the sensed data into frequency modulation. Integrating such a sensor with our low-power device would enable

tattoo form-factor sensing using the harvested energy.

2.5.4 Limitations and Future Work

The RFSP is a minimalistic platform that achieves sensing and communication with a minimum number of components. This enables it to be flexible, small, operate with a low power budget and is easy to use. However, such a minimalistic device comes with some trade-offs and limitations. As seen in Fig. 2.9, the RF device space has a large number of passive devices that come with digital processing and sensing. However, this addition of an ADC to digitize the sensed signals and a microcontroller to process and transmit them adds an overhead to the power budget of the device. From Fig. 2.9, this reduces the effective operating range of the device since it requires more power while RF energy available at increasing distances drops as $1/r^2$. On the other end of the spectrum are fully analog devices (the Great Seal Bug) that transmit the data as amplitude modulations. AM transmission of data have inherently low SNR and noise tolerance. With the RFSP, we have a fully analog platform that harvests energy from a 915MHz continuous wave, senses data, converts it to a frequency modulation and backscatters this as FSK to a remote receiver (RPU). While the RFSP achieves very low power operation (around $160 \mu\text{W}$ max), it comes with some limitations which are listed below along with some solutions for future directions.

- The RFSP does not have any processor on it, hence it does not currently have the ability to process the sensed signal or use any specific protocol to communicate them. It is designed for continuous backscattering of the sensed signals. Microcontrollers can be added to it, although this comes with its own power overhead.
- One of the main limitations here is security of the backscattered data, especially in the medical domain. The data is encoded as FSK and can be easily picked up by a sensitive receiver even 10 meters away. While this work does not focus on adding security features, one of the suggestions for future exploration is to use a low-power XOR logic that adds a pseudo random code to the data and provides a minimum

level of security. Another way is to reduce the TX power further (currently tested at 26dBm max) for applications where a large range is not necessary (example, bedside sensing). At a given transmit power level, the RFSP will still have larger operation range than other more complex RFID devices.

- Another limitation with the analog systems lies in the number of such devices that can be deployed simultaneously. While several tens to hundreds of the RFID tags can be used in the same environment, since they use time division multiplexing (TDM) or duty cycling, only a few of the analog sensors can be used with one receiver. Based on the application some of the following methods can be used to avoid collisions when using multiple RFSPs: a) If adding power overhead is permissible, a low-power state machine can be used to enable TDM and anti-collision protocols to the device. b) Another solution that is feasible when different sensors are used with the RFSP in an environment is to divide the bandwidth (10 kHz to 1 MHz) of the RFSP's oscillator to allocate sub-bands (channels) to each RFSP based on the sensor type and application. This also allows simultaneous transmission where different sensor RFSPs identify with a different channel. Moreover, it does not add any power overhead. c) In other applications where the sensors are localized, directional antenna on the RPU can be used to receive data from a specific sensor.
- The RFSP currently has a standard half wave dipole antenna. While this antenna is practical and simple to implement, application specific high-gain antenna design can increase its performance. One of the future directions is to design an inverted-F antenna for on-body applications.

The key features of the RFSP, which include simplicity, modularity, low power consumption and increased range are enablers for new analog sensor and sensing application development. The RFSP's flexibility across multiple sensing domains has been demonstrated in this paper with different types of sensing applications. We have provided results for sensing physiological signals (heart rate, temperature and breathing) as well as for sensing signals with

interesting frequency content (audio signals using a microphone). The RFSP is currently designed as a development platform for researchers to explore new sensing methods and solutions for encrypting analog signals. The detailed design specifications for the RFSP are provided and adding sensors or other features to it is a straightforward task. Moreover, the RFSP can be augmented with a thin-film battery and this extends its range to higher than 10 meters as shown in the paper. Adding an energy storage element can also be translated to higher power availability. This supports the power overhead that comes with the use of additional low power digital processing. In terms of power budget reduction: The largest amount of power consumed in the RFSP is by the oscillator, which accounts for around 80% of the total power budget. Hence to further reduce the power of the system two separate approaches can be used. Higher the frequency output of the oscillator, more power is consumed by the RFSP. The first method of setting an upper limit for the output frequency can keep the power consumption low. However, this method comes with a reduced resolution for the sensed data. The second method is to use an oscillator with lower power consumption than the existing option. Based on our extensive optimization for low power, the LTC6906 is the best COTS oscillator with the lowest power consumption for the range of frequencies between 10 KHz and 1 MHz. The work in [41] simulates the design for a low-power ring oscillator at 20 MHz. One of the solutions would be to implement a custom variable ring oscillator with low-power logic. This work also suggests using different power rails and simulates to show that there is significant power reduction with this method. In case of the RFSP, this method would be useful to maintain low power operation where future expansion requires using some simple digital logic. The 2.3 V rail that is currently used in RFSP is required for the oscillator operation. All other components can operate at supply voltage as low as 1.7 V, which will help reduce the remaining 20% power consumed by the other components on the RFSP..

2.6 Conclusion

We have so far characterized the RF Bandaid system which is a fully-analog wireless interface for resistive sensors. With the goal of bridging the gap between analog and digital backscatter platforms, we have presented the RFSP that can harvest energy from a dumb 915MHz continuous wave transmitter, measure and map sensor data to frequency modulations and transmit it out to a RPU using backscatter communication. This effectively moves all digitization and processing to a remote smart receiver, thereby reducing the power consumption, cost and size of the device. Owing to its low power consumption ($40 \mu\text{W}$ and $160 \mu\text{W}$), our device has shown continuous performance at a distance of 4 meters from the transmitter with a transmitted power of 26 dBm. We have also demonstrated the application scenario of deploying this system in a home, by testing sensor data transmission through walls to an RPU placed in a different room at a distance of 9 meters. We envision a bandaid sensor that can be used to sense physiological parameters like heart rate from a patient in a bed. With a transmitter on the bed powering the device, the RPU can be incorporated into a bedside clock that receives, processes and displays sensed data.

We also demonstrated extending the range of the device from the RX up to 9 meters when the device is powered by a small battery. The $160 \mu\text{m}$ thick battery from STMicroelectronics is rated for 1 mAh at 3.9 V and can sustain the device for several hours on a single charge. Finally, to demonstrate the device's ability to measure data from a wide range of sensors (medical and commercial) we have presented measurements for heart rate, breathing rate, temperature and audio data. This prototype was developed on a printed circuit board with COTS devices and was not optimized for space. The device can be shrunk down to a band aid form-factor with a small circuit board on fabric. Adapting better high-gain antenna designs would also optimize the power and data transfer.

Chapter 3

Implantable Wireless Neural Stimulator

The previous chapter presented the challenges and a solution for simple wireless sensing with respect to a wearable sensing platform. The rest of this work will focus on wireless biomedical sensing with implantable devices. This chapter describes the challenges with respect to power delivery and communication to implantable devices and presents a novel dual-band solution to address them.

3.1 Dual-Band Power Transfer and Communication

Wireless power and control have become a necessity for implanted devices, so as to improve implant lifetime and user comfort by eliminating batteries and subcutaneous cables. With the success of FDA-approved devices like deep-brain-stimulators and vagus nerve stimulators, there has been a growing interest in developing fully wireless/implantable interface devices for medical/neuroprosthetic applications [42]. Existing wireless neural interfaces either operate in the high-power domain ($\geq 100\text{mW}$), requiring near-field HF WPT, or in the low-power domain ($\sim 10\text{mW}$) which allows harvesting energy from far-field UHF signals [43]. While neural recording typically operates at low power ($\leq 50\mu\text{W}/\text{channel}$) electrical stimulation requires high power ($\geq 1\text{mW}/\text{channel}$). Such systems need to drive high-amplitude current pulses (10s of μA to 10mA), at high-voltage compliance (i.e. $\geq \pm 10\text{V}$), through interfacing electrodes in order to modulate neuron activity in the targeted tissue. Unavoidable loss in the front-end electronics driving the stimulus current further increases stimulator power consumption. At the same time, implanted systems which incorporate both neural

signal recording and stimulation are increasingly desired, with the former requiring communication data-rates and low-power transmitters. Such devices could revolutionize the treatment of limb paralysis caused by spinal cord injury, by creating an artificial bypass across the injury [44] [45] through post-injury stimulation (intra or epi-dural). Furthermore, the bypass could potentially be made bidirectional via taking neural recordings at the periphery and/or spinal cord and performing stimulation of the sensory cortex. Prior

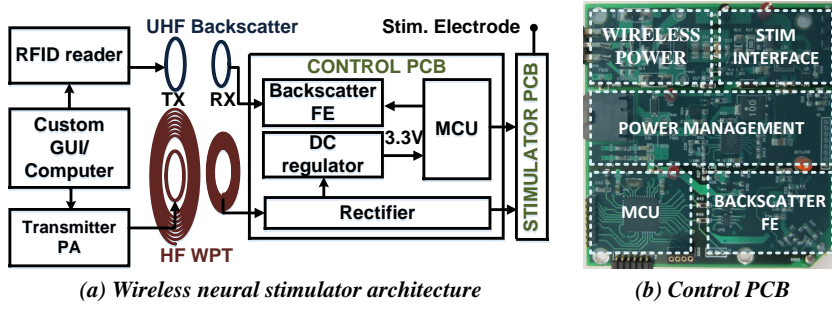


Figure 3.1: a) System architecture and control for the wireless neural stimulator, b) labeled control PCB

work on simultaneous wireless power and communication can be classified into two main categories: single antenna and multi antenna systems. Single antenna systems use one antenna/resonator operating at a single frequency for both near field wireless power transfer (WPT) and passive load modulation based communication. Load modulation for uplink is ultra-low power, however, it reduces the available power and creates a ripple at the output of a rectifier [46]. Additionally, downlink communication interferes with the power (ASK) and/or the recovered clock (PSK) at the receiver. Finally, there is a fundamental tradeoff between power transfer and communication. The efficiency of WPT is directly proportional to quality factor (Q) of the resonators and to achieve high WPT efficiency, high Q (i.e. low loss) resonators are used. On the other hand, communication data rate is inversely proportional to Q (low Q results in higher bandwidth). As a result, efficient power transfer and high data rate communication cannot simultaneously co-exist on the same resonator.

For example, authors in [46] demonstrate HF (1-13.56 MHz) power delivery of 100 mW but with very low data rate (10-100 KHz) communication. At UHF in [33, 47] high data rate communication (1 Mbps) is feasible but at the cost of low ($10 \mu W$) power delivery.

An alternative approach is to use separate antennas for power transfer and communication. However, this requires careful design and placement of antennas since the system suffers from interference between power and communication. Prior work has addressed the interference issue by designing orthogonal or coplanar coils for 1-100 MHz HF band [48–51]. Although orthogonal and coplanar resonator topology reduces the crosstalk between the wireless power and communication subsystems, it increases the size of the implant, which is prohibitive in most cases. Additionally, these systems have focused on design of resonators [48–51] to minimize the interference due to cross-coupling but do not evaluate how the residual interference impacts the communication performance. [49] proposed a coplanar coil topology with high speed OQPSK downlink but the system requires a power hungry receiver on the implant which is impractical for implanted systems. Finally, the systems are designed for wireless power and downlink and do not address high data rate, ultra-low power uplink communication which is required for applications such as neural recording systems. [48] proposed an active UWB radio for uplink communication, but is undesirable since it increases the power consumption of the implant.

This chapter presents a dual-band, HV-compliant ($\pm 30V$) neural stimulator, with near-field WPT at 13.56MHz and BSC at 915MHz. Recent work on dual-band power and communication [52], [53] demonstrates high data-rate communication for a system with fixed distance between transmitter (TX) and receiver (RX). [43] presents WPT at 915MHz for low current ($116\mu A$) stimulation but uses a battery for higher currents since harvesting high power is challenging at 915MHz. [53] also features an integrated version of a dual-band stimulator for seizure control ($\leq 3mW$), however, its stimulation capacity is limited to 10V and $30\mu A$. In contrast, the system presented is capable of delivering power on the order of 70mW ($\leq 0.5^\circ C$ tissue heating) with simultaneous bi-directional BSC and HV neuromodulation [54]. The BSC front-end currently uses a radio frequency identification (RFID) protocol

with 64Kbps data-rates. Improved data-rates on the order of several Mbps can be achieved using custom protocols that run in software. Future expansion of this system to record neural signals and transmit them out of the implant will benefit from high data-rate provided by the 915MHz communication. A system-level description of the neural stimulator is provided in Section 3.2, followed by a discussion on how the wireless system specifications were characterized (Section 3.3). Measurement results are provided in Section 3.4, including results from the *in – vivo* (anesthetized rat) evaluation of the wireless stimulator.

3.2 System Design

This implementation of a PCB-based wireless stimulator is an important proof-of-concept prototype for the future development of fully-wireless (and implantable) bidirectional neural interfaces, incorporating high-power neuromodulation, low-power neural recording, and digital processing. A block-diagram of the wireless neural stimulator and the labeled prototype are provided in Fig. 3.1. This main control PCB houses a 16-bit microcontroller unit (MCU: Texas Instruments - MSP430FR5969), which has 64kB of on-chip non-volatile FRAM memory. This prototype was designed for testability and hence is a four-layer PCB with test points and components on one side (5.2 x 5cm). The design has been optimized to smaller form factor for implantation and will be presented in the later sections.

3.2.1 Communication Scheme

Bi-directional BSC uses a Speedway Impinj R1000 reader controlled by a GUI implemented in python. The reader controller uses a Low Level Reader Protocol (LLRP) library to implement EPC Gen2 protocol [55]. Downlink (Reader to PCB) initiates communication with a 28dBm, Pulse Interval Encoded (PIE) signal and the uplink (PCB to reader) uses FMO modulation to encode data. The protocol is implemented on the MCU, which drives a switch across the antenna to modulate antenna impedance and backscatter the encoded data [56].

3.2.2 Power Management

The design of the system uses near-field resonant WPT to meet a 70mW power budget. The receiver chain includes full-bridge rectification and DC regulation using a Linear Technology synchronous buck-boost converter (LTC3115) that can operate within a input voltage range of 2.7V to 40V. This regulator is operated in burst mode, which sets the regulator switching frequency to the minimum required to sustain the load current, thereby maintaining efficient power management across varied load conditions. A 30mW power required for operation of the MCU with BSC (at 3.3V) is dominated by the MCU power. The total power requirement of the system varies with respect to the duty-cycle of stimulation. For example, driving 1mA, biphasic pulse stimulus at $250\mu\text{s}$ pulse width and 200Hz stimulus rate (i.e. 10% duty cycle) with $\pm 10\text{V}$ compliance requires $\leq 1\text{mW}$, plus any additional power consumption due to stimulator inefficiency. The WPT transmitter (Fig. 3.1) employs a custom power-amplifier based on a class-E topology; this board interfaces with the external primary coil to deliver 0.25W at 13.56MHz.

3.2.3 High Voltage Stimulator

The stimulator design used in this work is a HV compliant ($\pm 30\text{V}$), constant-current neural stimulator that is discretely implemented on a PCB using off-the-shelf HV tolerant components and a microcontroller. The driver utilizes an H-bridge front-end based on the CMOS integration-compatible, high-voltage compliant topology presented in [12]. For a PCB implementation, this topology choice simplifies the design of the power-management design and mitigates the effects of on-board parasitics on the shape of the stimulus current waveform. The stimulus is regulated by a sinking 8-bit current-DAC (IDAC), configured to deliver $0\text{-}250\mu\text{A}$. The switching topology for this design is controlled by the MCU. The stimulator front-end interfaces with an active and return electrode, with large, series blocking capacitors included for safety and to enable post-stimulus charge-balancing via electrode shorting.

3.3 System Characterization

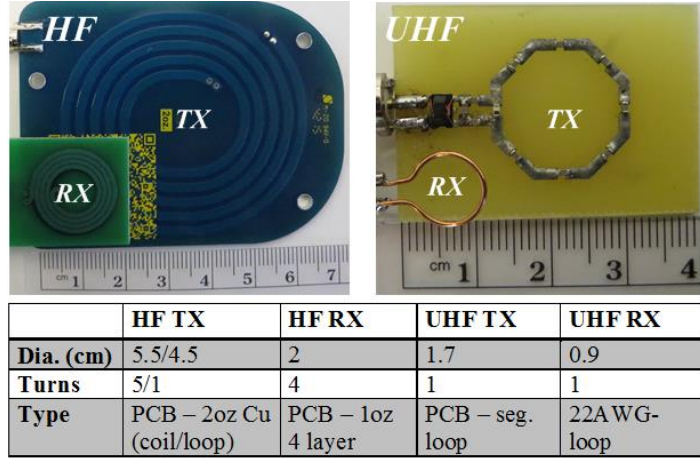


Figure 3.2: Design specifications for near-field HF (wireless power) and UHF (Backscatter Communication) coils

The TX and RX coils used for the following tests are shown in Fig. 3.2, along with their design specifications. The communication front-end on the PCB is tuned using an LC-filter network to match the impedance of the loop antenna, making the S11 a narrowband around 915MHz, thereby mitigating interference. The following subsections characterize WPT, BSC and HV stimulator.

3.3.1 Wireless Power Transfer

The S-parameter characterization of the two WPT coils is shown in Fig. 3.3a, for varied distances across a frequency range of 5MHz to 25MHz. Maximum power transfer occurs at 13.56MHz for the critical and undercoupled regions. While frequency splitting is observed in the over-coupled region. Fig. 3.3b shows the variation of WPT efficiency at 13.56MHz for varying TX-RX distances. Efficiency at the critically coupled region (10 to 20mm) is above 80% and falls off as the distance is increased, accordingly WPT can completely meet

the receiver load expectations (70mW) up to 45mm. A test to measure tissue heating with WPT across skin was done with the RX coil implanted in the abdomen of a sedated rat. Temperature increase was recorded in the tissue above and below the coil over 7 minutes of 100mW WPT and was noted to fall under 0.5°C. Implanting the coil in tissue generally leads to detuning of the coil due to additional tissue capacitance. To compensate for this detuning, the tuning capacitor on the receiver test coil was reduced based on an estimate study with ham and saline. The coil was also coated with a thin layer of Polydimethylsiloxane, a biocompatible material.

3.3.2 Backscatter Communication

To characterize the near fields BSC front-end and demonstrate simultaneous operation with WPT, the following study was done by varying the distance between communication TX and RX from 5 to 25mm at a reader output power of 28dBm. Power and communication TX coils were adjacently placed and the RX coils were placed facing the respective TX coil. The system was characterized by repeatedly reading 32 bytes of dummy-data from the MCU for a minute. Each read command using the EPC Gen2 protocol fetches 96 bits of EPC ID and 32 bytes of data (total of 352 bits). The entire communication was logged with a custom GUI and processed using a Matlab script to extract three parameters; bit rate (BR-Kbps), packet error rate (PER=failed reads/total number of reads) and received signal strength indication (RSSI);(Fig. 3.3d-f). These parameters were obtained when the PCB was both powered by DC supply and powered with WPT respectively. The first inference which can be made from (Fig. 3.3d and e) is that communication efficiency is not affected much by simultaneous WPT, which is reasonable since any interference between the two frequency bands were made negligible by design. This observation is consistent in both of BER and RSSI measurements. Secondly, PER is lower than 2% up to a distance of 20mm; however after 25mm the PER (BR) begin to significantly increase (decrease). The RSSI values show a quasi-linear decrease in signal strength as the receiver is moved away, with a sensitivity down to -60dBm.

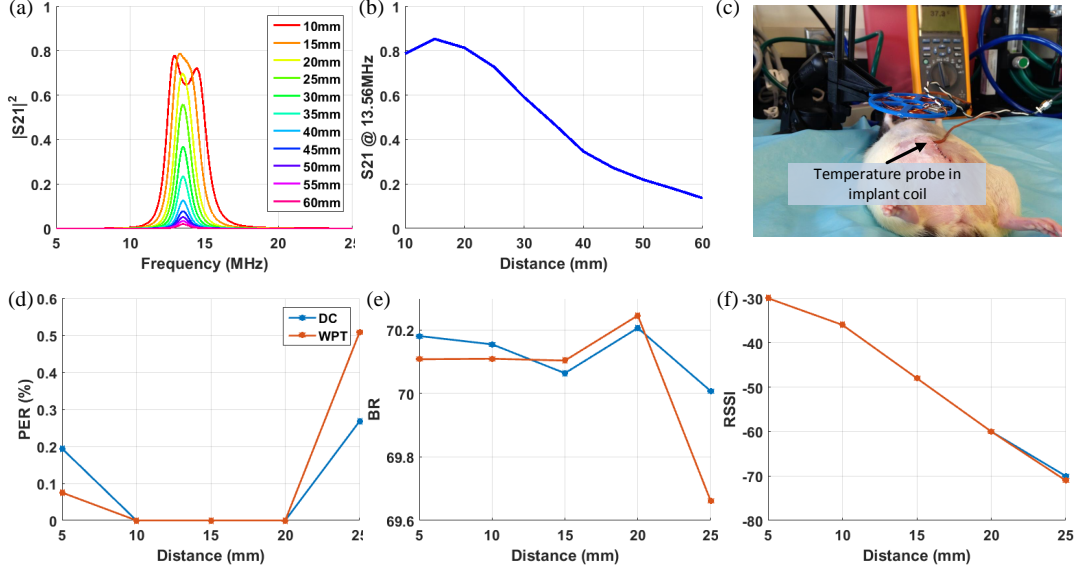


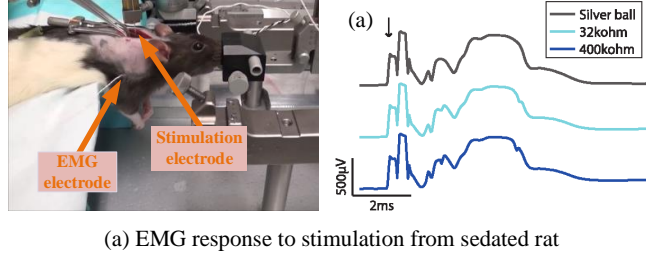
Figure 3.3: Characterization of HF WPT, a) shows the plot of $|S_{21}|^2$ frequency response for varied distances between Tx and Rx. b) is the S21 trace at 13.56MHz. The overcoupled region is indicated by the dip in S21 at 10mm. c) Implant in rat for temerature monitoring while transmitting 100mW of load power and d), e) and f) characterization of simultaneous UHF BSC communication at varying distances. Communication was good up to 20mm

3.3.3 Neural Stimulator

The wireless neural stimulator was bench-top tested to characterize power consumption. In stand-by mode(i.e. not driving a load) the isolated stimulator consumes 3.3mW to 8.5mW, when the HVDD is set at 3.5V to 24V, respectively. The entire system, including the control PCB, consumes \sim 70mW, in stand-by with HVDD set to 24V.

3.4 Wireless Spinal Stimulation

The stimulator was programmed to deliver biphasic stimulus to the spinal cord (C6 section) of a sedated rat to evoke muscle activity in the triceps. The system was powered wirelessly and stimulation was controlled by external commands transmitted over the UHF communi-



(a) EMG response to stimulation from sedated rat

Figure 3.4: The sedated rat with wirelessly powered and wirelessly controlled epidural stimulator, a) provides StTAs of triceps EMG response to spinal stimulation. Arrow indicates time at which stimulus was delivered.

cation channel. Stimulus pulse-width and frequency were set to $250\mu\text{s}$ and 1Hz, respectively. The active epidural stimulation electrode was a silver ball electrode, and the intra-spinal stimulation active electrode was a single tungsten microelectrode with either $32\text{k}\Omega$ or $400\text{k}\Omega$ tip impedance measured at 1kHz. Stimulus amplitude was varied with active electrode (32k or 400k). Electromyography (EMG) activity from the triceps muscle was recorded using 16 channels, each sampled at 24414KS/s for offline analysis. The stimulus-triggered averages (StTAs) were synthesized with a period of -1 to 9ms from the stimulus onset. The EMG data was then rectified and averaged. As shown in Fig. 3.4b, post-stimulation there is a clear EMG response in the targeted triceps associated with the applied stimulus. This correlated with triceps flexion in the sedated rat. The wireless stimulator was verified for reliable performance with all three investigated spinal stimulation configurations, with the capability of WPT to handle the varying load. The communication channel was also verified to have no drop-outs while operating along with WPT.

3.5 System Evolution

Based on the validation of the dual-band design with stimulation in the sedated rat, the system design evolved to a implantable formfactor with additional features. The current design of the prototype is sized to a implantable form factor as shown in Fig. 3.5(a). In

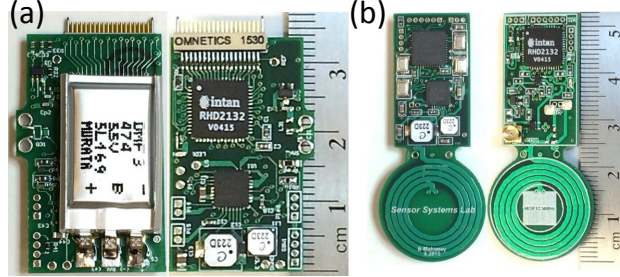


Figure 3.5: a) Prototype version 2 without coils, b) Board version 3 with WPT coil.

addition to the features from the main prototype board, it also has an off-the-shelf neural recording front-end from Intan. The Intan RHD2132 has 32 low-noise amplifier channels for unipolar neural signal recording. This prototype has also been verified for simultaneous WPT and BSC operation and is currently being developed to record neural signals. Fig. 3.5(b) shows a later version in which the WPT RX coil was included in the PCB.

3.6 Summary

This chapter demonstrated the operation of dual-band wireless HV neural stimulator that benefits from HF WPT (at 13.56MHz) and UHF BSC (at 915MHz) to control stimulation externally. WPT was capable of meeting the stimulator power budget (~ 70 mW) up to 45mm between TX and RX with an output power of 0.25W from the transmitter with $\leq 5^\circ\text{C}$ heating. BSC communication was efficient with less than 2% PER up to a distance of 20mm, while operating simultaneously with WPT. The application of this wireless stimulator to rehabilitation research, for patients with paralysis caused by spinal cord injury, was evaluated in-vivo with a sedated rat with varying stimulation electrodes and drive strengths.

Chapter 4

High Data-Rate Backscatter Communication for Implants

The previous chapter validated simultaneous WPT and BSC with RX coils placed adjacent to each other. This section demonstrates simultaneous WPT and high-data-rate bi-directional wireless communication using a concentric WPT and UHF receiver antenna configuration. The main goal here is to demonstrate reliable communication at \sim 6Mbps using BSC while being wirelessly powered. The backscatter protocol for uplink is implemented in an FPGA. The receiver for this protocol uses a wireless power harvesting and communication front-end implemented using 65nm CMOS process [57]. As before, we note that WPT at HF frequencies is highly efficient (lower attenuation) and communication at higher frequencies has larger bandwidth, which can support high data rates. We combine the benefits of WPT at HF and backscatter communication at UHF for simultaneous WPT and communication at high data rates. The top level architecture of the system is shown in Fig. 4.1.

4.1 System Design

This work investigates simultaneous delivery of high power wirelessly and ultra-low power high data rate wireless communication. While delivering up to 25mW of power we show that the system can achieve 6Mbps uplink communication at a separation of 1cm. The top level architecture of the system is shown in Fig. 4.1.

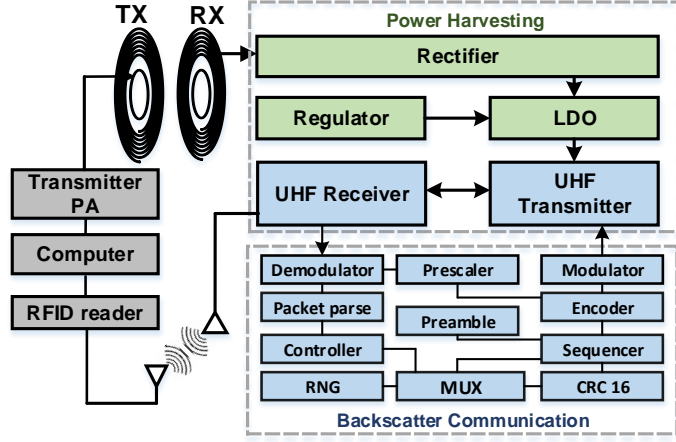


Figure 4.1: Top level architecture of proposed approach for simultaneous WPT and bi-directional communication

4.1.1 Near Field Wireless Power Transfer Specifications

A three coil magnetically coupled resonator topology operating at 13.56MHz was used for WPT between an external transmitter and the implanted miniature coils. The key advantage of resonant coupling is that adaptation techniques such as frequency tuning (used in this work) and impedance matching can be used to efficiently deliver power. The volume constraints for implants impose stringent size constraints on the implanted system. We use a 2cm diameter flat pancake coil made using 24 AWG copper wire encapsulated in PDMS as the receive resonator coil ($Q \approx 90$ in air) [57]. On the transmitter, we use 18 AWG 6.5cm diameter loop and a coil ($Q \approx 300$ in air). Transmit and receive resonators are optimized for an operating range of 7-10mm. The receive resonator was tuned by an external capacitor and connected to an on-chip HF rectifier. The technique to compensate for tissue-induced detuning of resonators presented in [58] can be used to achieve high WPT efficiencies with implanted coils. We implement a PMOS cross coupled switch and active deep-n-well NMOS rectifier using thick oxide I/O devices in 65nm CMOS process [59]. The

rectifier was optimized for mW level power delivery and achieves an efficiency of 80% for 25mW output power. The rectified and regulated output powers the communication and recording subsystems.

4.1.2 UHF Bi-directional Backscatter Communication

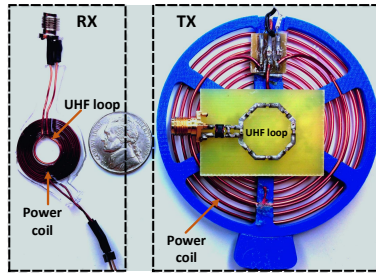


Figure 4.2: Transmit and receive resonators for simultaneous WPT and bi-directional communication

Backscatter communication at 915MHz is a perfect fit for neural implants that require low data rate downlink for sending commands and high data rate uplink to stream the recorded signals. For downlink, we use amplitude modulation with pulse interval encoding at 160kbps similar to an RFID reader. Since the implant is power constrained, active radios on the receiver are undesirable. Our receiver uses a charge pump based envelope detector followed by RC filters and a low power comparator to decode the bits. Uplink uses backscatter communication, wherein the implant switches the impedance at the receive UHF antenna between matched and short states to transmit bits. The external reader transmits the carrier wave and detects the change in reflected signal to decode the backscatter bits which are encoded using FM0 at 6Mbps. The reader implements time-domain multiplexing to avoid collision between down and uplink. The distance between transmitter and receiver is limited to 1cm in ECoG applications, which is in the near field at 915MHz. We use an 8 mm diameter loop antenna at the receiver and a segmented loop antenna for the transmitter [60] as shown in Fig. 4.2.

4.1.3 Digital Communication Block

The communication module was implemented in FPGA for IC compatibility and Fig. 4.1 shows the blocks involved in the communication protocol. The RX downlink from receiver provides the PIE clock and data which is demodulated and parsed for information based on the PIE delimiter measured. The controller decided the response package to send based on the parsed command using the random number generator (RNG for RN16), MUX and CRC blocks. The sequencer incorporates different parts of the packet together. The encoder performs a conversion of data into FM0 encoding. This data is then modulated and transmitted out to the backscatter switch on the antenna. The main clock frequency for the digital block is derived from 13.56MHz which is then divided to source other internal blocks. The Verilog implementation of the EPC Gen2 protocol with complete block read and block write modules and test protocols can be found in the repository in [61].

4.1.4 Integration and Interference Suppression

On the transmit side, HF power was prioritized and the UHF segmented loop antenna was placed behind the HF power coil. This configuration significantly improves the efficiency of WPT (compared to when the HF power coil is placed behind) and has minimal impact on the link budget of communication, which can be compensated with a nominal increase in the reader's transmit power. On the receive side, the UHF coil was placed concentrically inside the HF resonator, as shown in Fig. 4.2, to conform to the size restrictions. Concentrically placed coils have high coupling coefficient, which can lead to significant interference between wireless power and communication. We leverage separation in the frequency domain to minimize interference. First, since UHF band is used exclusively for near field communication, the UHF reader's transmit power is low and as a result, communication has negligible impact on WPT. Additionally, magnetically coupled resonators are extremely frequency selective (high-Q band-pass for efficient power transfer) and rectifiers have μF filtering capacitors at the output which makes WPT immune to interference at UHF.

On the other hand, the output power at HF is on the order of 100mW which causes significant interference on the UHF communication link operating at μW signal levels. To suppress this strong interference on downlink communication, first a high Q LC filter is used to match the receiver front end to the impedance of the UHF antenna ($6.7 - j63.9$). This provides the first level of filtering. Secondly, at the output of the four stage charge pump based envelope detector, additional band pass filtering which passes 160kbps downlink data suppresses the HF interference. Finally, a tradeoff between the sensitivity of the receiver and noise by introducing an offset in the comparator counters any residual interference at the input of the comparator. For uplink communication, the band pass on the external UHF reader suppresses the minimal interference from WPT in the UHF band. The receiver and transmitter on the implant side consumes an average of $2 \mu W$ and $950nW$ respectively. The baseband protocol is implemented on the FPGA was interfaced with the chip.

4.2 Experimental Validation

A HF rectifier and the UHF transceiver implemented in TSMC 65nm GP CMOS process were used for the following experiments [57]. The baseband protocol was implemented on a DE1 Altera FPGA and interfaced with the UHF front end. On the transmit side, a commercial power amplifier (100W1000B by AR) was used as the power source and the UHF backscatter reader was implemented on a USRP N210 software defined radio. The system was optimized to minimize the interference between wireless power and communication. The simultaneous operation is evaluated in the worst-case scenario, which would result in maximum interference. The output of the rectifier feeds a 1V LDO which requires a minimum input voltage of 1.2V while accounting for the 200mV dropout of LDO. The system was tested while operating at the worst case efficiency where 1.2V was set as the output. This configuration was achieved in experiment by sourcing 1.2V at the output of the rectifier and measuring the load current. The PA was set to deliver an output power of 200mW to a 50Ω load which supports a minimum load of 25mW at the maximum operating range of 1cm. The following experiments were run with the HF PA and UHF

reader operating simultaneously.

4.2.1 HF Wireless Power Transfer

The distance between transmit and receive resonators was varied and frequency tracking was used to ensure maximum power delivery. As the distance increased, the available power decreased due to reduction in coupling between the transmitter and receiver. The distance of 8mm was identified as the critical coupling point, and frequency tracking algorithm could deliver higher power to the receiver compared to fixed frequency operation. Beyond 8mm, frequency tracking algorithm converges to the fixed operating frequency of 13.93MHz since there was no frequency splitting beyond this point. The received power at 8mm was around 30mW and fell to the limit of 25mW at 10mm distance.

4.2.2 UHF Backscatter Communication

Next, the efficacy of UHF bi-directional communication between the implant and the external backscatter reader at 160kbps downlink and 6Mbps uplink data rates was tested. The output power of the reader was set to -5dBm (for operation up to 1cm) and the distance between transmit and receive resonators was varied. Fig. 4.3(a) shows the received signal at

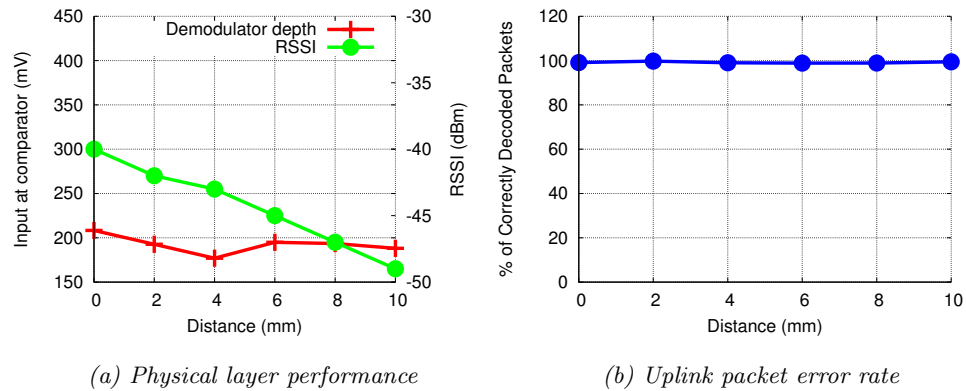


Figure 4.3: Near field UHF bi-directional communication performance.

the envelop detector and the RSSI of the backscatter uplink data receiver by the backscatter

reader. It can be seen that the signal strength decreases as the separation between transmit and receive antennas was increased. Moreover, the link budget for uplink communication is

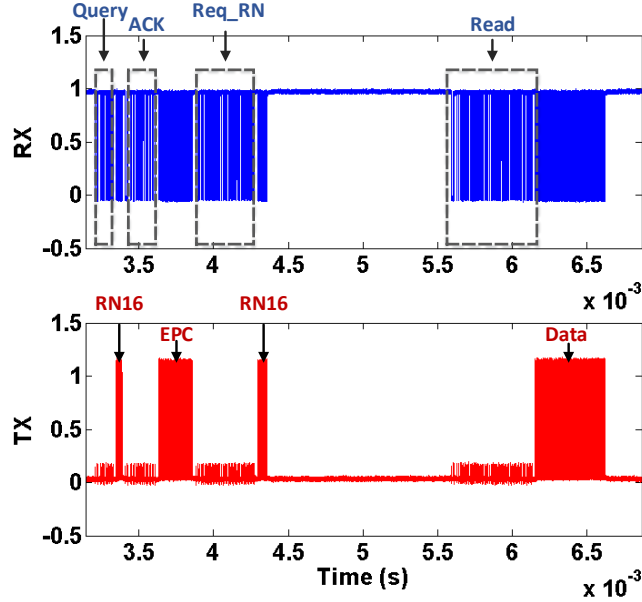


Figure 4.4: A time domain oscilloscope measurement of the baseband bi-directional communication between the external reader and the implanted system.

much greater than the sensitivity of the reader (-85dBm) which means either the transmit power can be reduced and/or higher data rate uplink communication can be supported with this configuration. Finally, Fig. 4.3(b) shows that percentage of packets correctly decoded on the reader to demonstrate the successful performance of the uplink communication up to a distance of 1cm. Fig. 4.4 is a time domain trace recorded from the implant on TX and RX ports. It shows the a single cycle of read command exchange with downlink encoded using PIE and the uplink response from the implant encoded using FM0.

4.2.3 Co-existence of WPT and Communication

Finally, we measure interference between WPT and communication. As expected, we notice that there is no interference due to communication on the output of the rectifier and

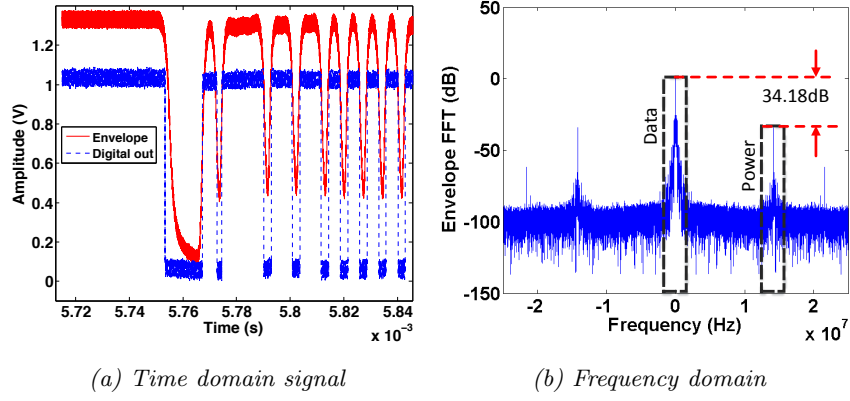


Figure 4.5: Co-existence of WPT and communication

similarly, there is no impact of WPT on the uplink communication. We study the impact of WPT on downlink communication by measuring the input to the receive comparator. This signal is shown in both time and frequency domain in Fig. 4.5. The time domain trace shows a comparison between the envelope and the filtered output to the demodulator. We notice a small 13.93MHz signal riding on top of the time domain signal at the output of the envelope detector and band pass filter. However, the additional offset in the comparator filters this interference to correctly decode the downlink data. The frequency domain plot shows that the interference from the power (25mW received) is 34dB lower than the average power of the downlink data.

4.3 Summary

This chapter introduced an approach of concentric antenna configuration for simultaneous wireless power transfer and wireless communication for implanted systems. Leveraging the benefits of wireless power transfer at HF and high data rate ultra low power backscatter communication at UHF, can enable large-scale fully implanted systems. The system design and performance of a high data rate communication system with simultaneous WPT was investigated and substantiated using experiments.

Chapter 5

Localized Wireless Power Delivery

5.1 Introduction to Phased-Array WPT and HF Echolocation

Wireless power transfer (WPT) using near-field magnetically coupled resonators has grown to the point where consumer devices with a single transmit (Tx) coil and single receive (Rx) coil can be found in use today. These systems are optimized and well-suited for applications where the mobility of the Rx coil is limited, such as wireless charging pads for phones where the Rx coil is placed directly on top of the Tx coil. However, if the desired transmission distance is greater than the diameter of the smallest coil in the system, or if the size of the Tx coil is much larger than an Rx coil, efficiency drops drastically [62]. Most consumer devices can accommodate this efficiency dropout as WPT is not critical for operation. When it comes to WPT for medical devices which help maintain organ function reliable power delivery becomes a necessity. Specifically, in case of wireless implantable systems the ability to targetedly deliver continuous power to the device is essential for normal operation of the implant. To facilitate targeted power delivery to a receiver, localization of objects in the powering space also becomes a primary necessity. Hence the two important challenges are;

- Targeted WPT to the device of interest
- Localization of the specific device

5.1.1 Targeted Power Delivery

To overcome the design challenges in HF WPT, transmit coil arrays can be used to improve efficiency across a wider power transfer range. Prior work has presented systems utilizing

multiple transmit coils [63–66]. However, these articles neglect the coupling between the Tx coils. It will be shown that the coupling between the transmit coils has a significant impact on the phase at which maximum (or minimum) power is delivered to the Rx coil. A WPT system with multiple Tx and Rx coils with inter-coil coupling that uses frequency tuning to optimize the system efficiency is presented in [67]. However, frequency tuning may violate the allowable bandwidths defined by federal regulatory bodies such as the FCC [68].

In [69] we show WPT to one or more receivers using phased array WPT system consisting of two (can be extended to more) transmit coils each driven by a power amplifier (PA). The transmitters are all phase-synchronized at the same frequency and the phase relationship between each transmitter can be dynamically controlled to enable constructive or destructive interference between the magnetic fields generated by each Tx coil. This work leverages the coupling between the Tx coils and uses amplitude and phase control to overcome decreasing efficiency associated with strong coupling between Tx and Rx coils. This work presents a thorough circuit analysis for a WPT system with two driven Tx coils and one Rx coil which is published in [70]. The control variables for these systems are the magnitude and phase of each transmitter. We derive expressions for the magnitude and phase that maximize or minimize power delivered to the Rx coil given any coupling coefficient arrangement between the various coils. Additionally, we derive the transition point that allows the system to determine cases where using a single Tx proves more efficient. Experimental results using a phased array WPT system are presented to verify the theoretical analysis.

5.1.2 Localization of Receiver

In case of near field WPT, a means of localization is of increased significance as the power levels can be very high and it is ideal to transmit power only to the targeted receive device. The reasons are primarily to conserve power and to avoid leakage of power to surrounding objects. Current localization protocols predominantly use radio frequency communication [71] and other hardware for detecting object presence. These systems consist of one or more Tx and Rx which communicate with each other to localize. This two-way communication adds

a burden to the Rx power budget in terms of localization.

To deliver power efficiently using the proposed phased array system, it is also important to localize the RX. With a single TX system, localization is done by having the RX inform the TX of its position using out-of-band communication, or use other position sensing hardware. This is primarily due to insufficient information gained from the reflected signal with a single TX. This chapter also presents a method that is analogous to echolocation used by bats and dolphins in nature. The goal for this work is to localize an RX by using the existing hardware on the TX side and eliminating the dependence on RX communication. The proposed method leverages the phase difference between the two HF transmitters to achieve localization. As we will see in the following sections, this method eliminates the necessity for additional hardware in the receiver dedicated to localization task. The theoretical analysis of this method will be explored in detail in the following sections.

The key advantages of implementing the localized phased-array WPT system are:

1. Increased range at which high efficiency can be achieved compared to a single transmitter system
2. Maximum efficiency can be achieved anywhere within a defined volume of space by optimizing the magnitude and phase of the various transmitters.
3. Maximum power regions and null-power regions can be generated simultaneously within a defined volume of space. This is desirable for systems that consist of multiple receivers where certain receivers can be targeted for charging.
4. Leakage fields can be reduced when maximum power is transferred to a targeted receiver compared to the single transmitter configuration. Minimum leakage fields are desirable for demonstrating regulatory compliance and mitigating the amount of energy induced upon surrounding objects.

5. Localization of object to set phase and magnitude variables for targetted maximum power delivery withing the Tx area.
6. Move the burden of localization entirely to the receiver. This eliminates the requirement of extra hardware and power dedicated to localization on Rx

$$\mathbf{V} = \begin{bmatrix} V_{TX,a1} \\ V_{TX,a2} \\ 0 \end{bmatrix}, \mathbf{Z} = \begin{bmatrix} Z_{TX,a1} & j\omega M_{a1a2} & j\omega M_{a1b1} \\ j\omega M_{a2a1} & Z_{TX,a2} & j\omega M_{a2b1} \\ j\omega M_{b1a1} & j\omega M_{b1a2} & Z_{RX,b1} \end{bmatrix}, \mathbf{I} = \begin{bmatrix} I_{TX,a1} \\ I_{TX,a2} \\ I_{RX,b1} \end{bmatrix}$$

$$\mathbf{V} = \mathbf{Z}\mathbf{I} \quad (5.1)$$

$$\begin{aligned} Z_{TX,a} &= R_{S,a} + R_a + j\omega L_a + \frac{1}{j\omega C_a} \\ Z_{RX,b} &= R_{L,b} + R_b + j\omega L_b + \frac{1}{j\omega C_b} \\ I_i &= \frac{\det(\mathbf{Z}_i)}{\det(\mathbf{Z})} : \quad i = 1, 2, 3 \dots n \quad V_{o,b} = I_b \times R_{L,b} \end{aligned} \quad (5.2)$$

5.2 Theoretical Analysis of Phased-Array Power and Localization

Phased-array of transmit antennas for beamforming have shown promise for extending the range of far-field wireless applications [72–74]. These systems rely on shifting the relative phase of transmitters to achieve constructive or destructive interference in the radiation pattern to maximize power delivery to a specific receive antenna. Mutual coupling in far-field phased-array systems can significantly affect the system as spacing between antenna elements decreases [75]. Consequently, the effect of mutual coupling is typically considered parasitic and requires mitigation techniques. However, the parasitic mutual coupling can be leveraged to improve range and efficiency [76]. Near-field WPT systems must also optimize the mutual coupling between coils for efficient operation.

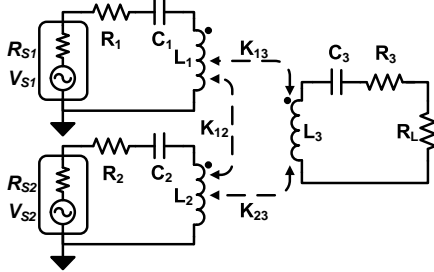


Figure 5.1: Circuit representation of a three coil system.

In the proposed system, the magnitude and phase shift of each transmitter can be controlled independently. Parameters are derived that determine scenarios where the phased-array system outperforms a single transmitter. Depending on the strength of the transmit-coil coupling coefficients, the wireless power can be optimized or minimized to an arbitrary location within a three-dimensional volume of space.

5.2.1 Equivalent Circuit Analysis

Using lumped-element circuit theory, the output voltage V_o at any of the receiving coils may be derived using mesh-current analysis. The matrices in (5.1) present the general case of n coupled coils. \mathbf{Z} is a square matrix of the impedance parameters and contains n^2 elements. The main diagonal comprises the reactance and resistance of each coil, which is a function of the self-inductance, tuning capacitance, source and load impedances and parasitic resistances. Using Cramer's rule, the unknown mesh currents can be determined. The \mathbf{V} vector accounts for the driving voltage source of each Tx coil. The driving voltage corresponding to each Rx coil is 0 since the Rx coils are not driven.

In this representation, we assume there are a transmitters and b receivers. In each Tx coil, the resistance is the sum of the source and parasitic resistances. Similarly, in each Rx coil, the resistance is the sum of the load and parasitic resistances. Also, the load in each Rx coil is purely resistive. Thus, the output voltage of the i^{th} coil V_{oi} is the product of load

resistance and the mesh current. M_{ij} is the mutual inductance between the any two coupled inductors and can be calculated as a function of the distance and angular alignment between two coils [77]. For the three coil system, the magnitude of the voltage across R_L of the Rx coil is shown in (5.3). Fig. 5.1 shows the equivalent circuit model of a phased array WPT system using $a = 2$ Tx coils and $b = 1$ Rx coils. Each coil consists of a winding inductance $L_{a|b}$, a parasitic AC resistance $R_{a|b}$ and a series tuning capacitor $C_{a|b}$. All coils are coupled by the coupling coefficient k . Consequently, there are $n(n - 2)/2$ coupling coefficients where $n = a + b$ is the total number of Tx and Rx coils in the phased-array WPT system. Each Tx coil is driven at the same frequency by a phase-synchronized voltage source with adjustable magnitude and phase.

Assuming that the frequency of the two coupled Tx coils is equivalent, phasor analysis can be used to add the contributions of each transmitter. The cumulative effort of the two Tx coils may interfere constructively or destructively, depending on the relative phase difference. In this analysis, the voltage source for the first TX coil (TX_1) is considered the reference source, with a phase $\phi_1 = 0$ and a magnitude $\alpha_1 = 1$. Thus the phase difference $\Delta\phi = \phi_2 - \phi_1$ between the two Tx coils reduces to the phase ϕ_2 of the second transmitter's (TX_2) voltage source. Ideally, for a symmetric system with $k_{12} = 0$, if $\phi_2 = 0$ then constructive interference results in maximum V_o . Conversely, if $\phi_2 = 180^\circ$, then the two transmitters are out of phase, which results in destructive interference and consequently a reduction in V_o . This anti-phase condition minimizes power delivered to the Rx coil.

For the remainder of the 3-coil discussion, α and ϕ will represent the magnitude and phase respectively of the transmitted signal from TX_2 such that $V_{S1} = \cos(\omega t)$ and $V_{S2} = \alpha \cos(\omega t + \phi)$. The magnitude of TX_1 will be normalized to one and the phase set to zero such that $V_{S1}=1$ in the phasor domain. Using Euler's identity, the second source will provide the magnitude and phase offset relative to the first source such that $V_{S2} = \alpha \cos(\phi) + j \alpha \sin(\phi)$. Additionally, a symmetric system will be considered such that $L_1 = L_2 = L_3 = L$, and similarly for R and C of the coils. The same analysis can be applied to an asymmetric system, only the expressions become much larger and are not included here. The subscripts

for TX₁ will be references as 1, TX₂ as 2 and RX as 3.

$$V_o = \frac{\omega R_L [(\omega M_{12}M_{23} + jM_{13}Z_2)V_{S1} + (\omega M_{12}M_{13} + jM_{23}Z_1)V_{S2}]}{Z_1Z_2Z_3 + \omega^2(M_{12}^2Z_3 + M_{13}^2Z_2 + M_{23}^2Z_1) - 2j\omega^3M_{12}M_{13}M_{23}} \quad (5.3)$$

$$\alpha_{opt,min} = \frac{\omega^3 k_{12} L R C^2 (k_{23}^2 - k_{13}^2) \sin \phi - k_{13} k_{23} (\omega^2 R^2 C^2 + k_{12}^2) \cos \phi}{\omega^2 k_{23}^2 R^2 C^2 + k_{12}^2 k_{13}^2} \quad (5.4)$$

$$\alpha_{opt,min,symm} = \frac{k_{13}}{k_{23}} \cos \phi \quad (5.5)$$

$$\phi_{opt,min} = \tan^{-1} \left[\frac{\omega^3 k_{12} (k_{13}^2 - k_{23}^2) L R C^2}{k_{13} k_{23} (\omega^2 R^2 C^2 + k_{12}^2)} \right] \quad (5.6)$$

$$\phi_{opt,max} = 180^\circ - \phi_{opt,min} \quad (5.7)$$

5.2.2 Maximize and Minimize Power Delivery

For the function V_o , $\alpha_{opt,min}$ represents the optimal solution that minimizes V_o . The expression for $\alpha_{opt,min}$ in (5.4) is a function of the inter-coil coupling coefficients k_{12} , k_{13} and k_{23} , the coil parameters L , R and C and ϕ . $\alpha_{opt,min}$ is derived by differentiating V_o with respect to α , setting the result equal to zero, and solving for α . For a given ϕ value, $\alpha_{opt,min}$ represents the magnitude that will give a relative minima of V_o at that specific phase shift. Since $\alpha_{opt,min}$ is dependent on ϕ , it will only imply an absolute minimum for V_o if the phase at which V_o will be minimized ($\phi_{opt,min}$) is specified.

When $k_{12} = 0$, (5.4) simplifies to (5.5). In this symmetric case, the absolute $\alpha_{opt,min,symm}$ always occurs at $\phi = 180^\circ$, which creates perfect destructive interference between the two transmitters and allows for an absolute minimum of $V_o = 0V$. If $k_{13} > k_{23}$ and $k_{12} = 0$, α_2 needs to be greater than α_1 by a factor of k_{13}/k_{23} to minimize V_o because TX₂ needs to compensate for the stronger coupling between TX₁ and the Rx coil. Alternatively, when $k_{13} < k_{23}$ and $k_{12} = 0$, α_2 needs to be less than α_1 by a factor of k_{13}/k_{23} in order to minimize V_o . In the case where $k_{13} \gg k_{23}$, an absolute minimum of $V_o = 0V$ is not possible to achieve unless α_2 is very large in magnitude (i.e. TX₂ outputs significantly more power than TX₁).

$\phi_{opt,min}$ is derived by differentiating V_o with respect to ϕ , setting the result equal to zero, and solving for ϕ as in (5.6). Since $\phi_{opt,min}$ is independent of α , $\phi_{opt,min}$ can be calculated first, and

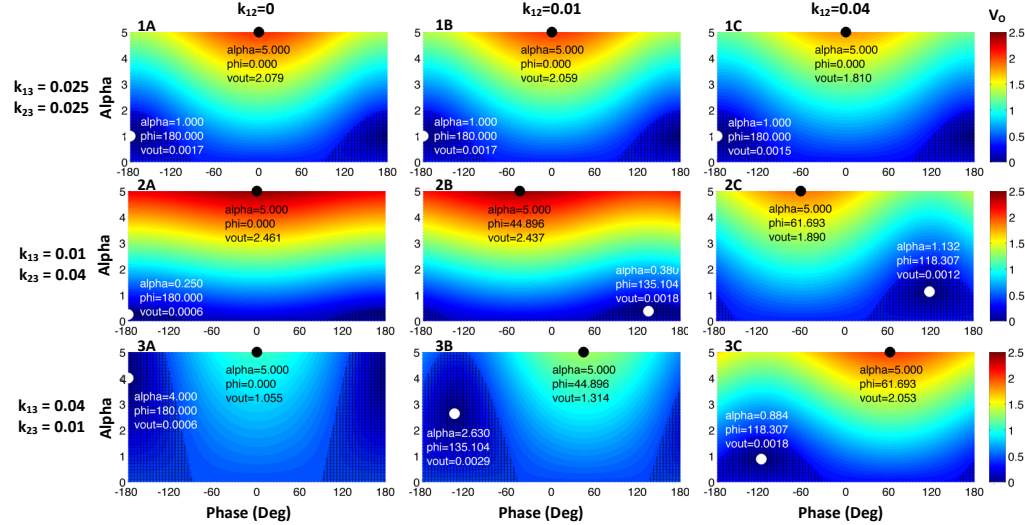


Figure 5.2: V_o for a range of α and ϕ for a three-coil phased-array system with varying k_{12} , k_{13} , k_{23} .

then used to find the $\alpha_{opt,min}$ at which an absolute minimum of V_o can be achieved.

The value of α that maximizes V_o ($\alpha_{opt,max}$) always corresponds to the largest allowable value of α . This is logical because α represents the magnitude of the transmitted power: sending more power results in a larger V_o . In a real system, $\alpha_{opt,max}$ is limited by the maximum output power capability of the power amplifier in the WPT system. When $k_{12}=0$, the $\alpha_{opt,min}$ simplifies to the result shown in (5.5).

The value of ϕ that maximizes V_o ($\phi_{opt,max}$) always corresponds to a 180° phase shift from $\phi_{opt,min}$ as in (5.7). Therefore all four expressions for $\alpha_{opt,min}$, $\alpha_{opt,max}$, $\phi_{opt,min}$, and $\phi_{opt,max}$ can be computed directly, which implies that power can be minimized or maximized for a receiver if its position relative to the two transmit coils is known.

5.2.3 Single Tx Vs. Phased-Array

To identify the scenarios where using two Tx coils has a higher V_o than one Tx coil, the configuration with only one active Tx coil was compared to the case with two phase-synchronized Tx coils. We define the transition voltage ($V_{o,trans}$) as the output voltage for which the two-Tx coil system becomes greater than V_o for the single Tx coil configuration.

For a better perspective, Fig. 5.2 shows V_o as a function of α and ϕ . For these plots, $\alpha_2 = \alpha$ and

$\alpha_1 = 1$. The magnitude of V_o is represented by the intensity of the color map. Each plot in the panel corresponds to a different configuration of coupling coefficients k_{12} , k_{13} and k_{23} . The dark hashed regions correspond to the scenario when a single Tx coil achieves a higher V_o than the phased array. The first row shows that for a symmetric configuration when $k_{13} = k_{23}$, the maximum V_o always occurs at $\alpha = 5$ and $\phi = 0$ while the minimum V_o always occurs at $\alpha = 1$ and $\phi = \pm 180^\circ$. The second and third rows show that when $k_{13} \neq k_{23}$, the α and ϕ values at which the maximum and minimum V_o occurs are dependent on all three coupling coefficients. As k_{12} increases, the maximum achievable V_o decreases when $k_{23} > k_{13}$. However when $k_{23} < k_{13}$, higher k_{12} improves V_o because k_{13} is over-coupled, and as more energy couples from TX₁ to TX₂, the overall energy delivered to the Rx coil at a single operating frequency increases. Corresponding to the observation made in Section 5.2, to minimize V_o when k_{23} is four times greater than k_{13} and $k_{12} = 0$, α_2 must be four times less than α_1 (Fig. 5.2-2A). Similarly, to minimize V_o when k_{13} is four times greater than k_{23} , α_2 must be four times larger than α_1 (Fig. 5.2-3A).

$$\alpha_{trans} = 2\alpha_{opt,min} \quad (5.8)$$

The α value below which $V_o < V_{o,trans}$ for a given phase difference between transmitters is defined as α_{trans} (5.8) and is derived from Equation. 5.3 when TX₂ is off. This parameter can be used to identify the best configuration to use (single Tx coil or phase-synchronized Tx coils) for a given configuration of coil coupling coefficients. If the goal is to minimize V_o , it is always more suitable to have two Tx coils assuming the proper $\alpha_{opt,min}$ and $\phi_{opt,min}$ are applied for the given coupling coefficients. However, if the goal is to maximize V_o it may be better to have just one Tx coil if α_{trans} is greater than the maximum allowable α that can be realized by the power amplifier.

5.2.4 Echolocation Principle

The principle of using phased-array transmitters to implement WPT systems was introduced and the optimal settings for magnitude and phase have been theoretically analyzed. In such multi-Tx systems, the magnitude and phase of TXs are swept to obtain constructive and destructive interference for location-selectable power delivery. However, an estimate of the location of the receiver is necessary to set parameters for targeted maximizing/minimizing of power. The method presented here characterizes the system with two Tx coils and one Rx coil to achieve localization of the Rx in a 2D space. The goal for this work is to localize an Rx by using the existing hardware

on the Tx side and eliminating the dependence on two-way communication between the Tx and Rx communication.

$$\Gamma_n = \frac{Z_n - Z_0}{Z_n + Z_0} \quad (5.9)$$

The operation principle for this method relies on the change in \mathbf{k} between the Rx and Tx coils at different locations of the Rx. This in turn varies flux between the three coils. The \mathbf{Z} matrix for the three coil setup shown in Equation. 5.1 and 5.2 are also used to characterize the localization process. The \mathbf{Z} matrix contains 3x3 elements representing the impedance of the three coil system. The reflection parameter (Γ) which is obtained based on the \mathbf{Z} matrix is a ratio of the outgoing and incoming waves at a port. This relation is provided in Equation 5.9 where Z_n is the impedance at the n^{th} port (5.1) and Z_0 is the characteristic impedance (port termination/reference impedance - typically 50Ω). Thus the reflection parameter is dependent on the mutual inductance between coils. As the position of Rx is varied, the M_{12} , M_{23} and M_{31} change which varies the non-diagonal elements in the \mathbf{Z} matrix. This in turn gives rise to changes in the reflected and transmitted signals. Looking back at 5.2, the phase variation changes the interference pattern between the two Txs. At any given position of Rx, by involving a third control knob, (ϕ), information on the position can be inferred from the signals reflected at various phase differences between TX₁ and TX₂. The Z matrix increases in dimension with N coils as NxN, making the dependencies more complex. Hence, the reflected signals get more complex as the number of coils increases, and these dependencies provide more knobs to localize precisely.

5.3 Validation of Phased-Array Operation

In order to validate the expressions derived in Section 5.2, several experiments were conducted to compare the simulated results with experimental measurements.

The schematic for the experiments is shown in Fig. 5.3. It comprises two independent power amplifiers that are controlled by a single MCU and a precision clock distribution circuit for phase adjustment. The clock distributor is based on the AD9510 by Analog Devices. Received power is measured using a 50Ω 40dB attenuator and Agilent U2001A RF power meter. The TMS320 digital signal processing unit controls all the hardware on the transmitter board including a direct digital synthesizer for frequency generation, a single-ended class E PA [78] with a programmable supply voltage determined by a digital potentiometer that controls the output voltage of a DC-DC

boost converter, and an RF magnitude and phase detector that analyzes the forward and reverse signals from the bi-directional coupler. The Tx and Rx coils are all identical with an inductance of $L = 17.2\mu H$, series tuning capacitance of $C = 8pF$ and AC resistance of $R = 1.2\Omega$ with a resonant frequency of 13.56MHz.

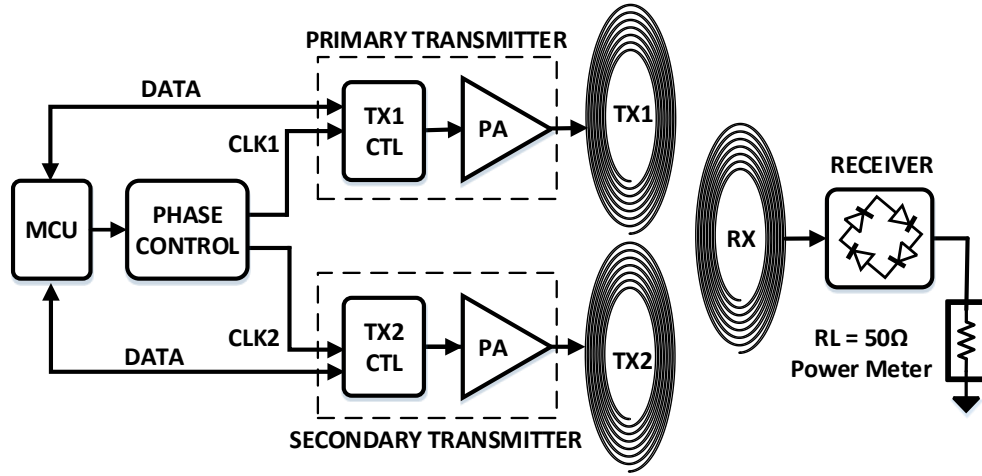


Figure 5.3: System level block diagram of experimental configuration using two Tx coils and one Rx coil.

As illustrated in Fig. 5.4 column A, the two Tx coils are positioned on two adjacent faces of a cube-like volume. We repositioned the Rx coil inside the volume to demonstrate different coupling configurations with each Tx coil. These positions were at 20, 69 and 135mm from TX₁ with the Rx coil always parallel to TX₁ and orthogonal to TX₂.

At each distance, we set the output power level of TX₁ and TX₂. The output power from each transmitter was set by connecting the output of each PA directly into a 50Ω RF power meter and adjusting the supply voltage to the PA. Relating back to the circuit analysis from Section 5.2, the magnitude α of each sinusoidal input V_S represents the power level of each transmitter. When the transmitter with an arbitrary source resistance R_S is connected directly to a fixed load resistance R_L , V_S relates to power delivered to the load power by:

$$P(W) = R_L \left(\frac{V_S}{R_S + R_L} \right)^2 \quad (5.10)$$

TX₁ was configured to deliver 1W into the 50Ω load, and remained fixed for all experiments.

For the first experiment, TX_2 was configured to transmit 5W, which corresponds to the maximum output power capability of this PA. Next, we configured TX_2 to deliver 1W into the 50Ω load, so that each transmitter delivers the same amount of power. Then we set the output power of TX_2 to correspond to the value of $\alpha_{opt,min}$ for the given coupling coefficient configuration. Since $\alpha_{opt,min}$ depends on k_{12} , k_{13} and k_{23} , the power level had to change for each of the three distances in this final experiment, but was always between 1 – 5W.

At each power setting and Rx coil configuration, we varied the phase of TX_2 relative to TX_1 from -180° to 180° at 10° increments and recorded the received power level with the Rx coil terminated by a 50Ω RF power meter. The experimental results are shown in Fig. 5.4. The red curves represent the experimental received power for each respective coil configuration.

A careful examination of these plots shows that for the same Rx coil position (i.e. same row), the minimum and maximum received power levels occur at the same ϕ value. This proves that $\phi_{opt,min}$ and $\phi_{opt,max}$ are independent of α , and only depend on the various coupling coefficients between the coils as expected from (5.6) and (5.7) respectively.

In order to validate our theoretical model, we extracted the coupling coefficients k_{12} , k_{13} and k_{23} from each of these configurations. There are direct calculations to compute coupling coefficients between two coils based on the coil geometries and distance between the coils [79]. However, for two Tx coils and one Rx coil, these approximations are not accurate. Therefore we relied on MATLAB to identify the best-fit coupling coefficients that match the experimental results with the theoretical circuit model, given the data obtained for each of the physical configurations. Since the coupling coefficients are only dependent on coil position, the coupling coefficients are constant across different power levels. Hence, the coupling coefficients are the same for each plot in the same row in Fig. 5.4; however, they differ from one row to the next as the coils are repositioned.

Using these extracted coupling coefficients, along with the equivalent V_S values corresponding to the various Tx power levels (5.10) and the measured coil parameters ($L = 4\mu H$, $R = 0.95\Omega$ and $C = 34pF$) of each identical Tx coil, V_o was calculated using (5.3) for the same range of ϕ as in the experiments. The simulated Rx power can be calculated from the output voltage measured across a 50Ω load. These simulated results are represented by the blue curve in Fig. 5.4.

Comparing the blue and red curves proves that our theoretical circuit model and simulation results for V_o accurately match the measured experimental results across all configurations. The maximum and minimum output power levels correspond to the calculated values of $\phi_{opt,max}$ and $\phi_{opt,min}$ respectively. Consider panel 1B for example: from (5.6) and (5.7), $\phi_{opt,min} = 110^\circ$, and

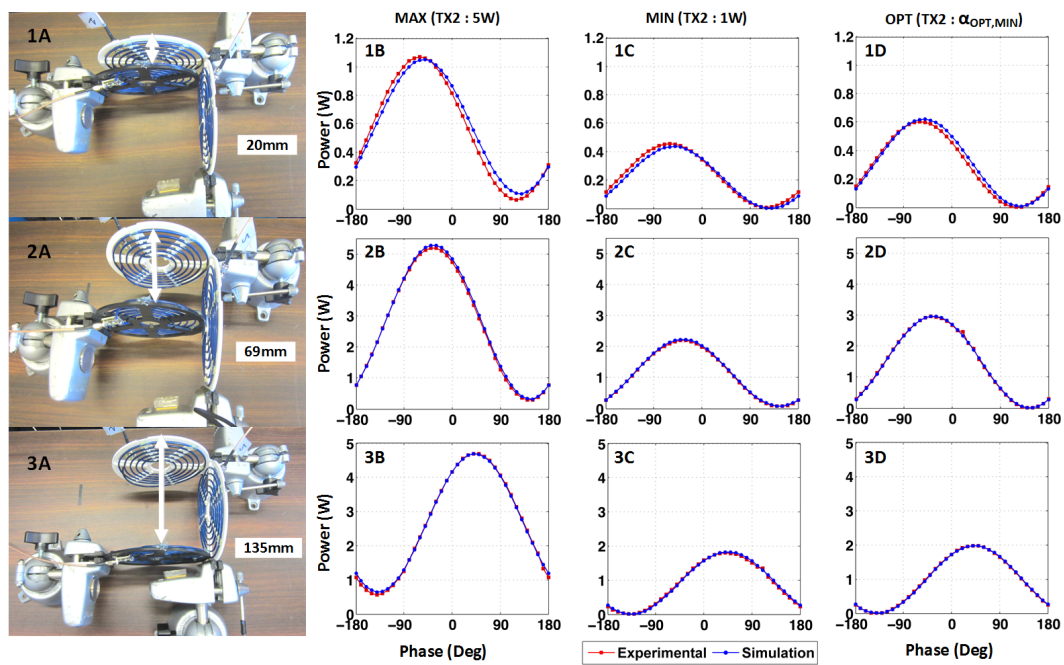


Figure 5.4: Experimental and simulation results for received power corresponding to three different coil configurations and various Tx power levels.

$\phi_{opt,max} = -70^\circ$, which closely match the measured phase at which minimum and maximum power occurs for the experimental result of 104° and -76° respectively. The expression for $\alpha_{opt,min}$ can be similarly validated for any of the results from column D.

By adjusting ϕ and α at any of the three Rx positions, the received power may be minimized or maximized. As expected, the maximum output power for each configuration always occurs for maximum P_{TX2} (i.e. maximum α) in column B. Additionally, by comparing columns B and C, a much wider range of power can be delivered to the Rx coil when TX_2 outputs more power than TX_1 . Although the minimum value of V_o is always greater in column B compared to column C, the difference between the peaks and troughs in column B are much wider than in column C.

The absolute minimum value of V_o always occurs when α is properly set to $\alpha_{opt,min}$ in column D. This may seem counterintuitive because the power levels of TX_2 in column D are always greater than those in column C, yet column D achieves the lowest V_o . Even though V_o can be driven close to zero for each power level, the lowest V_o is always achieved in column D when the system operates at $\phi_{opt,min}$ and $\alpha_{opt,min}$.

5.4 Experimental Validation of Echolocation

In the following experiments both TXs are powered by individual custom made class-E PA PCBs. It should be noted that the power from the PA to the Tx coil will change as the load impedance presented to the PA changes. In other words, even though the supply voltage to the class-E PA is fixed for all these experiments, the amount of power consumed by the PA and the RF output power from the PA will change as the distance between the Tx and Rx coils changes and as the phase between the two Tx coils changes. The schematic design and the setup are shown in Fig. 5.5A and B. The Rx is connected to a power meter through a 50Ω attenuator. A directional coupler at the output of the PA passes the forward and reflected signals to an RF detector. Magnitude and phase of reflected signal and Tx power for each position was recorded using the PA GUI (forward/reverse signals at TX). For the following sections we refer to this as the S11 parameter that is used to localize the Rx position. The experimental setup is very similar to the one presented in the previous section with some changes to the Tx signal generation. For this set of experiments, the PA phase and amplitude are controlled by output ports on a Tektronix AFG3252 dual channel function generator. A python driver is used to setup the AFG3252, perform the sweeps and log data from it. The time series signal that is logged can be used to verify the input signal to the PA. The Tx boards initially

carry out a standard ϕ sweep from -180° to 180° while Rx is absent. The Rx can be localized by analyzing the S11 parameters at each ϕ sweep. The PA control interface logs the S11 data which is parsed using Matlab and compared for localization, however, this calculation could be done in real time on the DSP. For 2D localization, the space in front of the Tx coils is divided into multiple

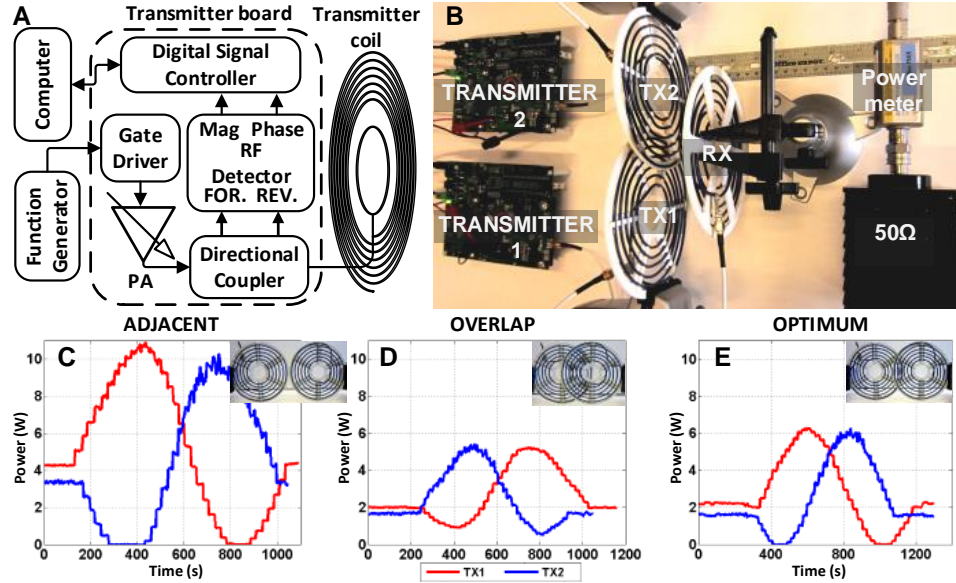


Figure 5.5: (A) Schematic of transmitter, (B) Experimental setup. The time trace of Tx power variation during phase sweep for (C) Adjacent, (D) Overlap, and (E) Optimal configurations.

positions which will be explained in the following sections. The Rx coil is placed planes parallel to the Tx coils.

5.4.1 Optimal Tx configuration

Before proceeding with the experiments, it is important to identify an optimal configuration for the two Tx coils. Two different Tx coil arrangements were initially considered. In the first arrangement the Tx coils are placed adjacent to each other (ADJ), and in the second they overlap (OVLP) by more than 50 % as shown in the insets of Fig. 5.5C and D. The drive strength of each Tx was 5Vpp. PA slow, periodic sweep of ϕ was carried out and the power level at each Tx for each ϕ value was recorded. The time series data of Tx power level is plotted in Fig. 5.5. It is evident that the

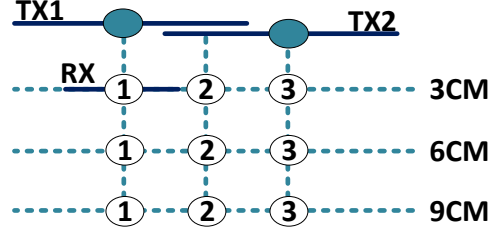


Figure 5.6: Different positions of the Rx coil used in the localization experiments. Tx Coils were positioned in the optimal overlap configuration.

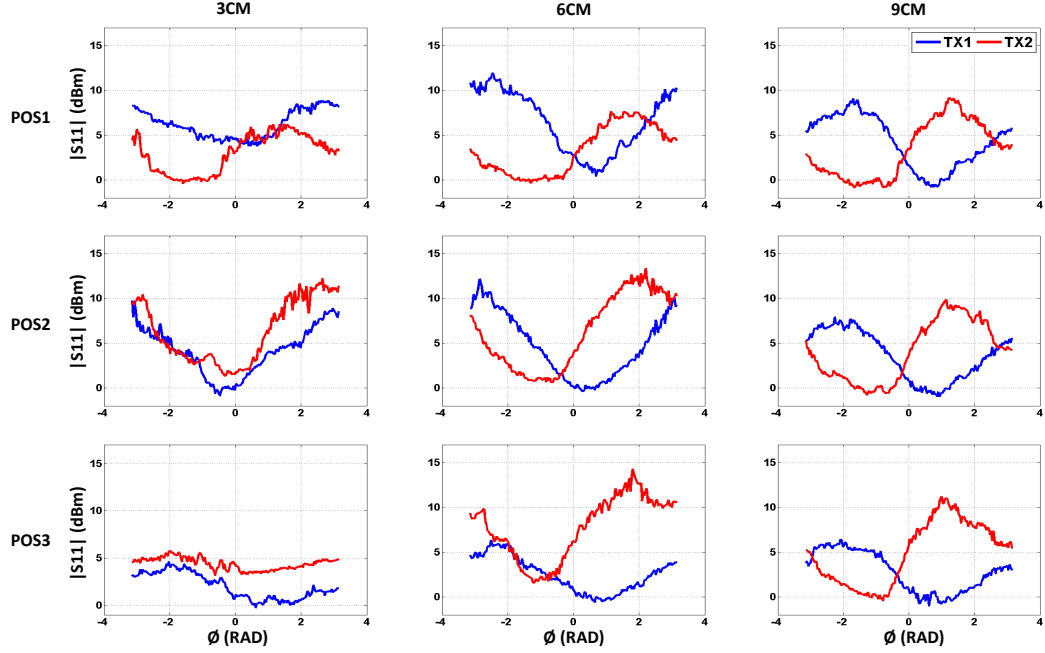


Figure 5.7: Magnitude plots for reflected signals over ϕ sweep for nine Rx positions.

coupling between TX_1 and TX_2 in case of ADJ is high. This is indicated by the large fraction of power dissipated in the absense of Rx coil (10W peak and $\sim 4\text{W}$ when ϕ is 0) when compared to OVLP (5W peak and $\sim 2\text{W}$ when ϕ is 0). This is primarily because the PA is optimized to drive a 50Ω load and the adjacent configuration changes the load value leading to more energy coupled

between the two Tx coils and dissipated across them. The coupling k_{12} in OVLP is relatively low where the system almost presents a 50Ω load and hence there is less power dissipated across the Tx coils. Also, due to the excellent k_{12} localization is easier in the ADJ configuration. High Tx coupling (k_{12}) results in high power dissipation between Tx coils even when Rx is absent but has very large correlated changes with ϕ sweep. Whereas, very low k_{12} implies low power dissipation but also lower correlation with ϕ change. To identify a configuration with low power dissipation as well as good localization ability a set of standard measurements were obtained for several configurations and the optimal case was selected as shown in Fig. 5.5E. The power dissipation level was kept low while obtaining a substantial change on either Tx while sweeping ϕ .

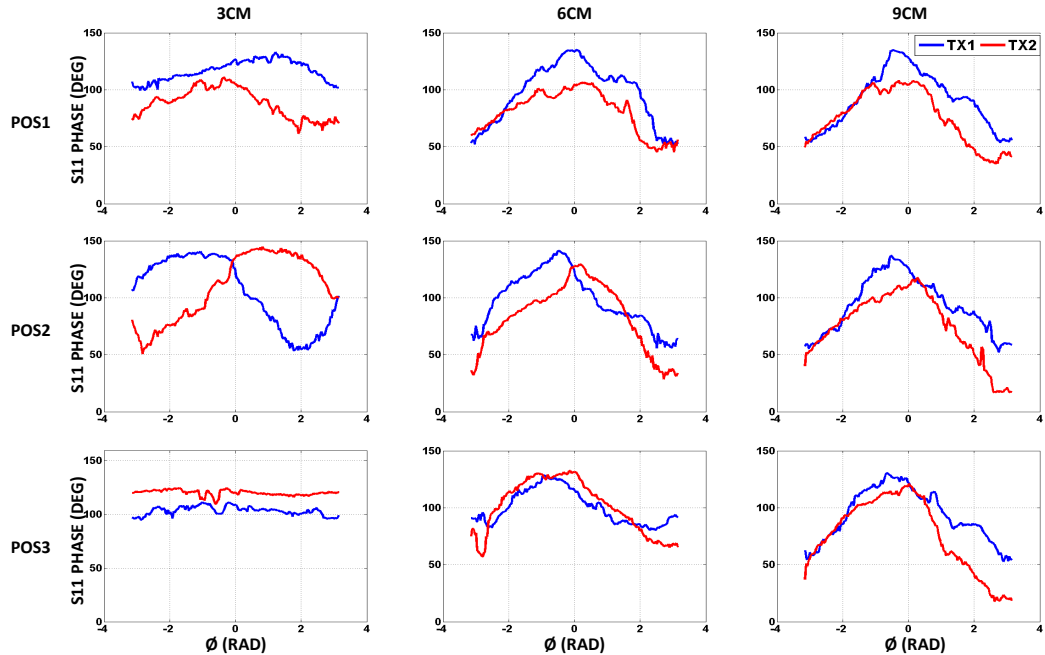


Figure 5.8: Phase plots for reflected signals over ϕ sweep for nine Rx positions.

5.4.2 Localization experiment

To identify a method of localizing the RX, a second set of experiments are performed. The PAs are both driven by the function generator. The phase of TX₁ is set at -180° and ϕ is swept from

-180° to 180° at 2° increments using a python controller interface to the AFG3252. S11 magnitude and phase are recorded at each ϕ setting. For 2D localization in this experiment, the space in front of the Tx coils is divided into 3 positions at three distances; in front of TX_1 (POS1), between the Tx coils (POS2), and in front of TX_2 (POS3). Each position at distances of 3cm, 6cm and 9cm from the Tx coils represents overcoupled, critically coupled and undercoupled regions respectively, as shown in the picture above Fig. 5.7. The Rx coil is placed parallel to the Tx coils at each of the nine positions depicted by circles in the picture.

Fig. 5.7 shows the recorded S11 magnitude plotted on the y axis with the phase sweep in radians on the x axis. Similarly Fig. 5.8 presents the S11 phase data on the y-axis with phase sweep on the x-axis. This data represents the S11 values averaged over two trials. In the 3cm distance, when the Rx is placed in front of TX_1 , both S11 phase and magnitude of TX_1 are greater than that of TX_2 (POS1), similarly when Rx is placed in front of TX_2 (POS3). However, if Rx is centrally located between the two Tx coils, there is no clear distinction between their S11 magnitudes while the shift in phase signals reflect the position to some extent(POS2). A similar trend can be observed in the 6cm plots. It is clear that both phase and magnitude are necessary to identify the positions at the different distances. This point becomes clear in the 9cm configurations as it can be distinguished from the other two distanced based on magnitude, but differentiating between the three positions by simple comparisons is challenging. This is because the Rx is now in the undercoupled region where the S11 signals are small and very close to the standard without any RX.

To make localization achievable within the given range, a localization parameter (LOC) was formulated to localize the Rx based the S11 data of each TX. A shape dependent centroid was first calculated for the magnitude and phase curves of S11 based on (5.11). Where, R represents the centroid, A is the amplitude of the curve at point B across the phase sweep, for each of the traces. R is computed over the i samples in the trace. For all nine configurations the LOC point was computed as given in (5.13). Where, R_{M1} , R_{M2} , R_{PH1} and R_{PH2} stand for the centroid of magnitude and phase of the two TXs respectively.

$$R = \frac{1}{\sum_{i=1}^n A_i} \left\{ \sum_{i=1}^n (A_i * B_i) \right\} \quad (5.11)$$

$$X = R_{PH2} - R_{PH1}, \quad Y = R_{M2} - R_{M1} \quad (5.12)$$

$$LOC = (X, Y) \quad (5.13)$$

The $LOCs$ of all nine configurations are plotted in Fig. 5.9A. The x-axis is the difference in the

phase centroid (X) and the y-axis is the difference in magnitude centroid of each location (Y). The constellation in red, blue and green represents the three distances 3cm, 6cm and 9cm. POS1, POS2 and POS3 are represented by circle, star and square markers respectively. The constellations for the three distances can be clearly distinguished in space and these are used as reference locations. A separate set of experiments were then performed by placing the Rx at approximately the same nine positions and S11 data is recorded with ϕ sweeps at 2° increments. This is followed by another set of measurements made with ϕ sweeps at 3° increments. The first set of data has 180 data points, while the second set has only 120. These experiments are used to verify that the Rx can be localized consistently with repeatability and also to estimate the effect of varying number of data points. The

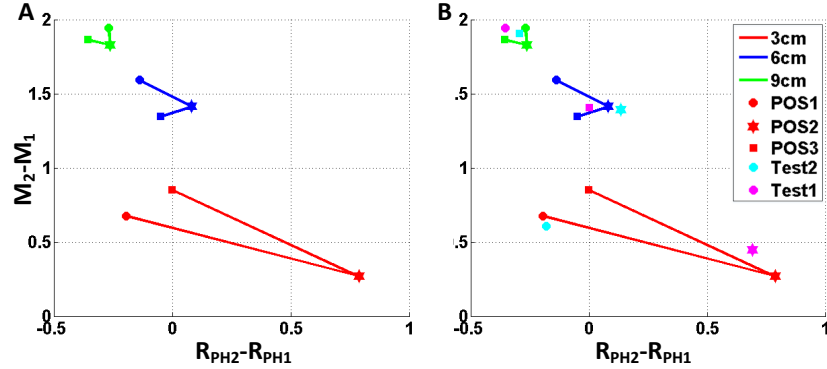


Figure 5.9: (A) LOC constellation plot showing averaged LOC parameter for three different distances and each position from multiple trials(B) Test case localization points were added for 2° and 3° sweep interval

LOC points for the recorded S11 data are computed in the same way as mentioned above. Three positions are chosen for the 2° sweeps; they were approximately POS1 at 3cm, POS2 at 6cm and POS3 at 9cm. The cyan markers in Fig. 5.9B represent these results and the estimates closely match the actual position. Similarly, three positions are chosen for the 3° sweeps; they were approximately POS2 at 3cm, POS3 at 6cm and POS1 at 9cm. The purple markers on Fig. 5.9B represent these locations. They also closely match the actual positions. Therefore, we can confirm that variance in the number of points in the ϕ sweep does not impact the localization accuracy. A shortest distance vector can be used to localize the Rx precisely around one of the reference locations. This simple heuristics-based algorithm can be run on a DSP to locate the Rx without additional out-of-band

communication dependence. This gives the Tx an approximate location of the Rx that can be used to obtain the local settings for maximum/minimum power delivery.

5.5 Summary

In this chapter we demonstrated that phased-array WPT systems can have advantages in terms of system efficiency and minimal leakage fields if the phased array system is designed and implemented properly. Proper design and implementation requires a rigorous understanding of the circuits and controllable parameters for a phased-array WPT system. We provide a thorough analysis of a generalized multiple transmitter, multiple receiver phase-synchronized WPT system that can be used to quickly simulate complex networks of wireless power transmitters and receivers.

The experiments and analysis in this work consists of a three-element system, consisting of two Tx coils and one Rx coil. We define critical parameters that allow the user to directly compute the magnitude and phase that either maximizes or minimizes power delivered to the load. These features have been experimentally validated and also been compared to operation with a single Tx coil.

This chapter also analyzed and demonstrated the use of phased array coils to achieve 2D localization of a receiver in near-field WPT systems. An optimal arrangement of TX coils was considered for this process to enable both lower power dissipation and localization. The localization mechanism leverages the difference in phase and magnitude of the forward/reflected power on each TX and also its difference from a standard measurement without any RX. A simple heuristics-based algorithm was developed to be run on the TX side and tested for localization of the RX, thus eliminating the dependence on communication with RX. Future direction to explore in this topic are on expanding the localization system to include more than two Tx coils. Furthermore, algorithms to precisely localize several Rx with better spatial resolution would help improve targetted power delivery.

Chapter 6

Closed-Loop Neural Interface

The need for a miniaturized device that can perform closed-loop (CL) operation is imminent with the growing interest in brain-controlled devices and in using stimulation to treat neural disorders. Such a device reduces the latency with transmission of recorded neural signals to an external computer for decoding. Towards the BCSI application, this chapter presents the Neural Closed-Loop Implantable Platform (NeuralCLIP), a modular FPGA-based device that can record neural signals, process them locally to detect an event and trigger neural stimulation based on the detection. The development of this implantable device and its on-board processing capability are analyzed in the following sections.

6.1 Introduction

Neural interface devices enable brain-controlled technology and provide tools for studying the brain and treating neural disorders. The next generation of such devices must be miniaturized and implantable to record neural signals and stimulate neurons [80]. Using the recorded signals, these devices should enable real-time detection and treatment of neural disorders. Hence the device needs to be able to perform local computation on the recorded signals to identify triggers for closed-loop neural stimulation.

Research in this field can be classified into three broad efforts. First, neural signal acquisition, including the development of state-of-the-art recording devices and electrodes [9] [10] [11]. Second, neural stimulation circuits capable of activating and blocking neuron function [15] [54]. Third, processing the recorded signals to either detect events (like epilepsy seizures) or decode intent (correlate neural signals to action intent) for closed-loop operation. While recording and stimulation are moving from bench top circuits to integrated circuits (ICs), signal analysis is yet to be miniaturized. Moreover, tying the three efforts together to make a small closed-loop device is still at an early stage. Statistical tools have provided us methods like Discrete Wavelet Transform (DWT) and Support Vector Machines (SVM) to analyze recorded data. The recent work in [15] [16] implement

processing of Spikes and Electroencephalogram (EEG for epilepsy detection) and are early attempts at fully closing the loop. However, these systems are limited to depending on external devices for processing or operate with signals at higher amplitudes (mV). Brain-machine interfacing applications require the ability to detect spike and local field potential (LFP) signals that lie in the $20 \mu\text{V}$ to $200 \mu\text{V}$ range. A detailed study is presented in [18] which presents closed-loop neural recording and stimulation in primates. This system, however, uses a rack-mounted test setup.

This work presents a miniaturized FPGA-based platform that combines the ability to record and process neural signals in the frequency range of spikes, LFP, ECoG and EEG. The platform is developed as a modular COTS printed circuit prototype that can scale processing in terms of system frequency, sampling rates and number of channels based on power availability and the neural signal of interest. The vision for this modular device is to enable research in low power closed-loop algorithms as well as to provide a platform to study and develop treatment for neural disorders. The FPGA-based processing makes it a useful development platform for future neural-interface ASIC development. The device is tested with a bio-signal calibrator as well as prerecorded LFP signals from a rodent. The test application for this platform is a brain-computer-spinal interface where closed-loop operation triggers stimulation in the spinal cord to bypass an injury and reanimate paralyzed limbs. The concept of stimulation for limb reanimation is explored in [14]. An illustration of the test application, description of the recording signal space and the NeuralCLIP platform are shown in Fig.6.1. The design, features and results from testing this device are described in the following sections.

6.2 System Design

6.2.1 Design for re-configurable operation

Neural signal acquisition, processing and neural stimulation have so far been implemented separately as miniaturized devices. The instances where they are used for closed-loop operation uses large rack-mounted test setups. The key capabilities of the NeuralCLIP, as shown in Fig.6.1, are recording, local processing and stimulating on a small form-factor device. In addition to physically shrinking the device, the power-hungry signal processing blocks are optimized to fit into this low-power implementation.

The NeuralCLIP uses a record/stimulate front end from Intan technologies (RHS2116), which has 16 unipolar channels that can be configured as low noise amplifiers or as constant-current stim-

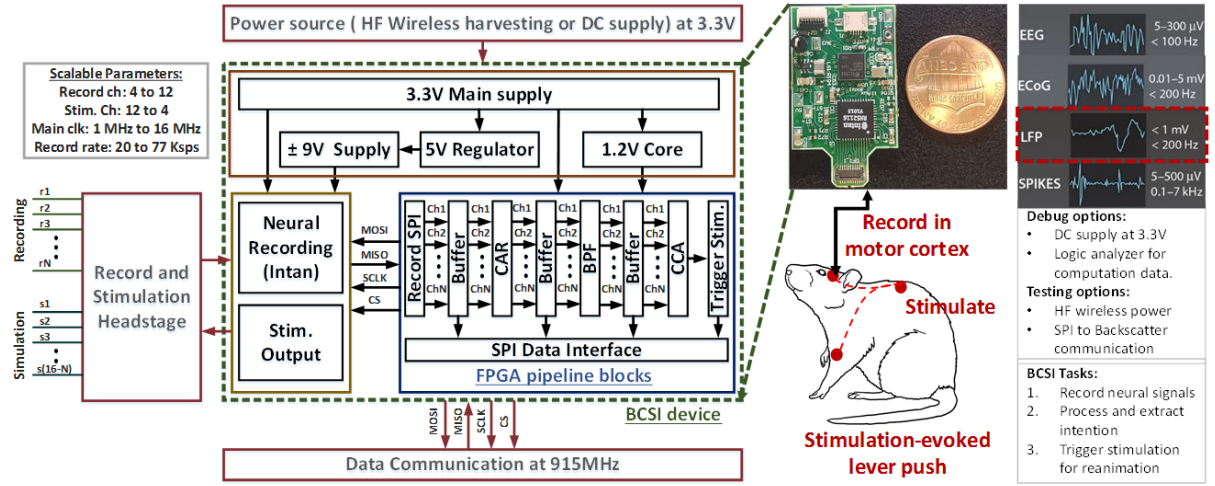


Figure 6.1: Image shows the functional block diagram and application of the NeuralCLIP. The application includes recording LFP signals from the motor cortex, processing them locally on the implantable device to identify intention and trigger stimulation in the spinal cord to reanimate an arm paralyzed due to spinal cord injury. The device block diagram shows the pipeline processing on FPGA. This includes modular synchronized blocks to configure the recording front-end to acquire the data from it, followed by filtering and correlation of the recorded signals to decode the motor intent. Decoded intent is then used to trigger stimulation. The device also provides a development feature where the secondary SPI module can be used to record data at each processing stage and communicate it to an external computer for training, study and analysis.

ulators. A four-wire serial peripheral interface (SPI) bus is used to configure and poll recording data from the Intan. The on-chip ADC provides 16-bit samples from 16 channels at a maximum 44 ksp/s each. The configuration architecture used in our device supports on-demand channel disabling to reduce power consumption by unused channels.

The central controller and processing are implemented on a low power FPGA from Microsemi (AGLN250). Specifically, the state machines for configuring and data acquisition from the Intan, the processing algorithm to provide stimulation trigger, and a secondary SPI debug channel are all implemented as synchronous modular blocks in the FPGA. These blocks are part of a pipeline controlled by the system clock. This modular implementation allows parallel data acquisition, processing and debugging, and makes adding or removing blocks easy. Each block can scale flexibly in frequency or channel count to optimize the system performance without affecting the processing

pipeline. This modular architecture also allows tailoring of the processing blocks to specific signals such as LFP. The parameters that allow for scaling and flexibility are as follows:

1. Processing clock: This parameter can be set to either 4 MHz, 8 MHz, or 16 MHz to scale the overall power consumed by the system.
2. Number of channels: The recording channel count can be set to N and the remaining 16-N channels are available for stimulation or can be disabled to save power.
3. Sampling frequency: The rate at which the Intan is polled, through SPI, sets the recording sample rate. Depending on the signal of interest and number of channels, the sampling rate can be set anywhere between 20 ksp/s and 77 ksp/s per channel.
4. Debug interface: The platform provides an optional secondary SPI block that can be used with a digital logic analyzer for debugging at each data processing stage. The architecture buffers data at each stage in the pipeline that can be transferred off-device for post-recording analysis.

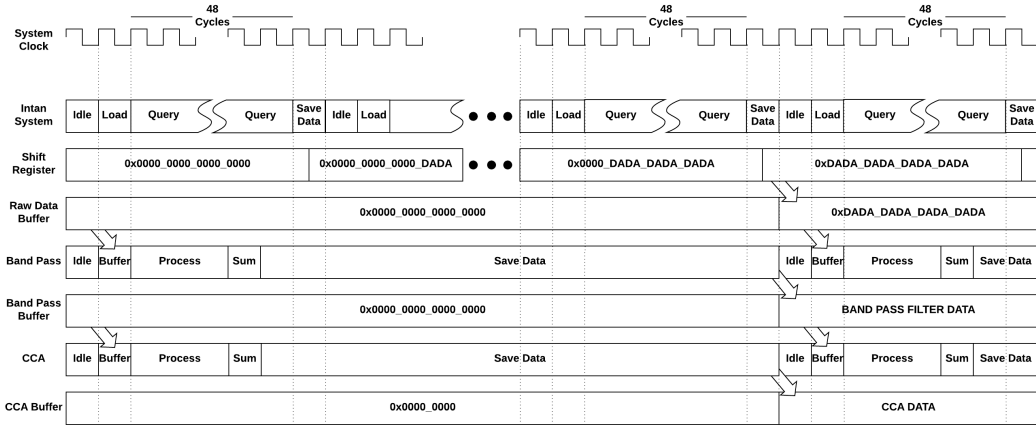


Figure 6.2: To record from N channels, the processing pipeline begins with the N Intan queries and the data is buffered for the N channels. This buffered data is then fed to the first processing block in parallel. The output of each block is buffered by N channels as input for the next block. A single system clock controls the transfer of data from each buffer to the next block and hence makes the functional blocks on the FPGA independent and synchronous. The data from N channels are thus processed in parallel. Processing blocks also function in parallel allowing optional addition or removal of blocks and channels.

The data acquisition and processing blocks are implemented in Verilog and used to configure the FPGA through the Libero SoC IDE.

6.2.2 Data acquisition and processing pipeline

A pipeline diagram for the data flow description is provided in Fig.6.2. The first stage in the pipeline is a state machine that communicates with the Intan to configure it and acquire data. All data is in 2's complement format to simplify arithmetic operations on the signed data. The second stage is an optional common average reference (CAR) filter that can be used to remove common noise. The third stage is a band pass filter (BPF) which typically consumes a large amount of resources. For example, a single instance of a 16x16 bit multiplier takes up 17 percent of the resources available on the FPGA. The filter implementation on the NeuralCLIP, however, is a normalized shift-to-divide approximate computing block. The filter coefficients are first generated for the frequency range of interest using MATLAB. By normalizing these coefficients to their nearest fraction of 2, we implement the divide operation as arithmetic right shifts. Since we handle 2's complement data, the division of a k-bit Sample (S) by a coefficient (C) to produce result (f_O) is reduced to the following form, where "k-bit-ext" is bit extension by k bits:

If (C[sign] is 1) :

$$f_O = \{\{k - \text{bit-ext}(C[\text{sign}]) \oplus S[\text{sign}]\}, \bar{S} + 1\} <<< C$$

else :

$$f_O = \{\{k - \text{bit-ext}(C[\text{sign}]) \oplus S[\text{sign}]\}, S\} <<< C$$

Such an implementation using approximate computing blocks trades accuracy and resolution of data to achieve lower processing requirements.

The fourth stage is a canonical correlation analysis (CCA) block that scales each channel with correlation coefficients [81]. The offline training to determine these coefficients is done with recorded data from N channels and the corresponding ground truth data in Matlab. The FPGA implementation is similar to that of the band-pass filter and uses approximate computing blocks to optimize for available resources. The CCA block demonstrated for in this application resembles a simple matrix multiplication to identify the correlation between different channels and the action intent. This block can be substituted with any other coefficient learning method based method to analyze neural signals for treatment of other disorders.

Figure 6.3: Power consumption vs. system clock

System Clock Freq (Mhz)	Single Channel Sampling Rate (ksps/ch)	Intan + FPGA Power (mW)
16	77.1	71
8	38.5	61
4	19.2	57

6.2.3 Device Power and Control

The power supply for this platform is derived from a central 3.3 V line that is used to generate a variable ± 3.3 V to ± 12 V supply for the Intan stimulator and a 1.2 V core supply for the FPGA. The maximum power consumption measurements for recording and processing across three system frequencies for 4 channels of LFP data is provided in Table 6.3.

For neural signals, the sampling rate per channel needs to be about 20 ksps, and can be reduced much further for the low frequency LFP signals (100 Hz to 500 Hz). This allows the system clock to be lowered in relation to the amount of processing necessary. To ensure this scaling, the platform is implemented with a flexible parallel architecture for the data processing pipeline where each block is synchronized to a global sub-clock. Thus, the overall device power consumption can be decreased by reducing the system clock, effectively lowering the data sampling rate and the data processing clock.

6.3 Test setup

To validate the NeuralCLIP operation in the frequency range of interest, a ground truth study was first performed with calibration signals. The signals used for testing are sine waves distributed in the bands of interest at 30 Hz, 200 Hz (Coulbourn Biosignal calibrator) and 800 Hz(Tucker Davis Technology (TDT)). The amplitude of these signals were in the 50 μ V to 100 μ V range.

The LFP processing algorithm was first implemented on the TDT benchtop system to verify correct closed-loop operation. Training to obtain CCA coefficients was performed using the TDT benchtop setup and a computer running MATLAB. This includes LFP recordings from the motor cortex of a rat and a ground truth lever push signal recorded from the lever as the rat's arm pushes against it. The correlation coefficients from training were used to first perform benchtop closed-loop stimulation testing. The decoded intent was used to trigger stimulation in the rat's spinal cord and

assist the rat in pushing a lever to obtain a reward. A sample of bandpassed data recorded using the NeuralCLIP is provided in 6.4. The top panel shows the channel data while the bottom panel shows the corresponding lever push data. The intent that needs to be decoded is visible as prominent increase in amplitude, across the frequency bands, that correlates with the lever push.

To verify the full processing pipeline on the NeuralCLIP, testing was done with prerecorded data from the motor cortex of the rat. Neural signals were first recorded from the motor cortex using the TDT setup. Second, the TDT neural output interface was used to emulate the rat by playing back the prerecorded neural data. The NeuralCLIP was then used to record these neural signals and process them. The CCA coefficients extracted from a window of this recording, in correlation to the lever push, were programmed into the approximate computing CCA block on the NeuralCLIP. Supply voltage of 3.3 V was derived from an external DC source. A Saleae digital logic analyzer was used to extract data from each block. The following signals were logged; raw recorded signal, the BPF output and the CCA output from N channels. We use N = 4 due to a limitation on the number of output channels from the TDT.

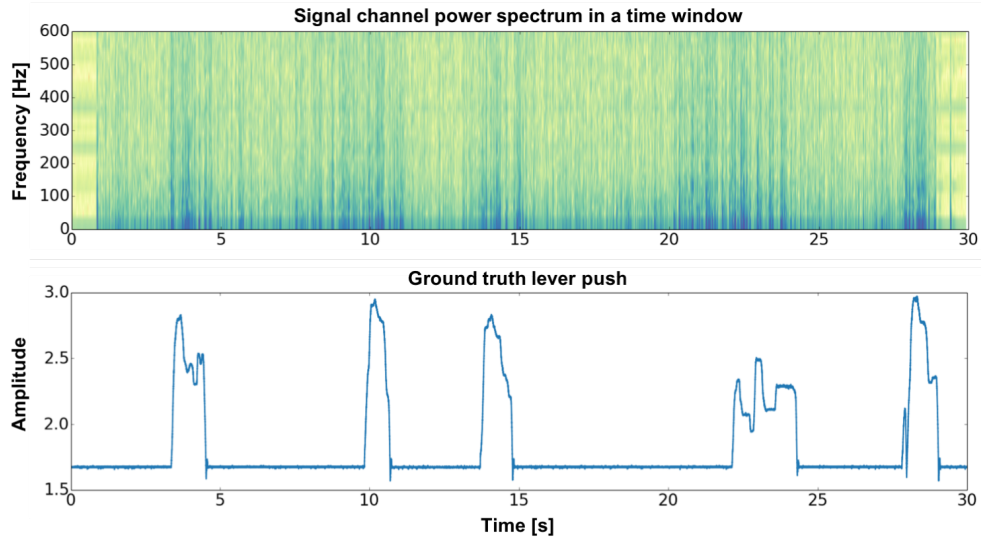


Figure 6.4: The top panel shows the power spectrum over a 30 second window of neural signal recorded from the motor cortex of a rat. Bottom panel shows the corresponding lever recording with an active push indicated by rise in amplitude. The power spectrum data that indicates the intent for lever push lies in the frequency bands up to 500 Hz.

6.4 Results and Discussion

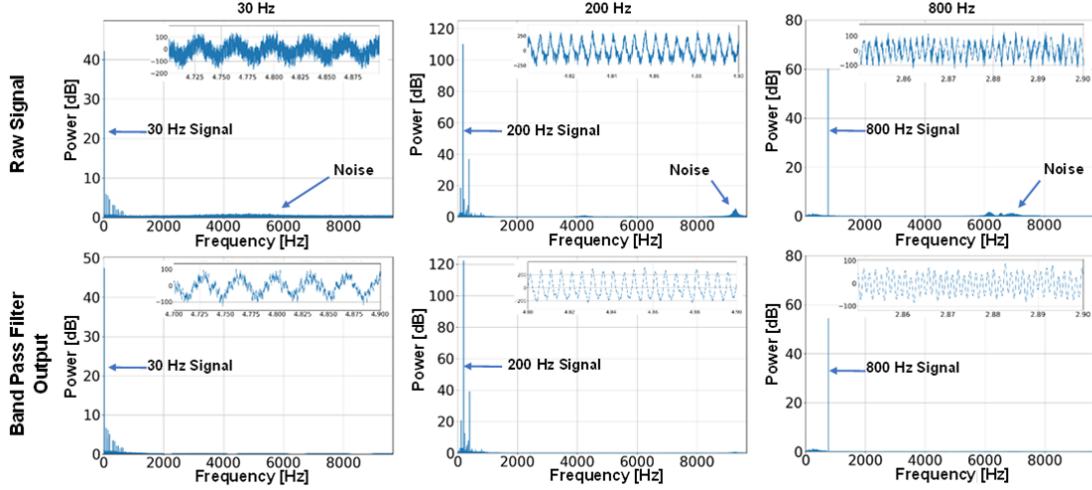


Figure 6.5: FFT plots for the three calibration signals from platform. The buffered data from Record SPI block are provided on the top panel and the corresponding BPF buffer output in the bottom panel. Insets show filtering of high frequency signal and improved signal quality.

This section presents and discusses our test results and future work. The first set of tests on the device verify it's ability to record and process neural signals in the frequency range between 20 Hz and 1 kHz, which is shown in Fig. 6.5.

The recorded signals, exported through our debugging interface, shows that the 30 Hz, 200 Hz, and 800 Hz test signals were properly recorded with high SNR, but it also shows recorded harmonics of the signal. Specifically, in the 200 Hz recording, the frequency that we would expect our LFP signals to be at. This is acceptable since the next largest harmonic is a third of the magnitude as our signal of interest. Additionally, the magnitudes of the 30 Hz and 800 Hz signals are lower than the 200 Hz signal due to the cutoffs we set on the Intan IC's band pass filter, with a low cutoff of 100 Hz and a high cutoff of 500 Hz.

Next, to validate the CCA block, we tested the NeuralCLIP by playing back LFP data recorded from a rat while the rat was performing a lever push task. We demonstrate the NeuralCLIP's ability to decode the intention by comparing the CCA output to the ground truth lever push data. The CCA data represents a weighted representation of four channels of data. Fig. 6.6 shows one out of

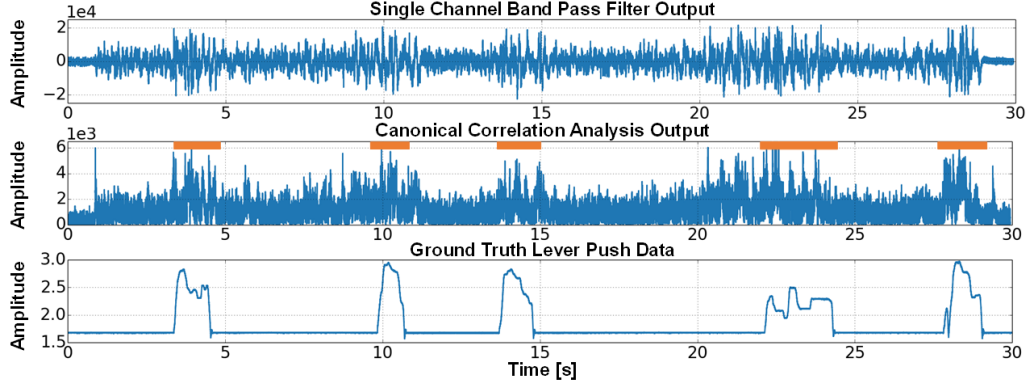


Figure 6.6: Testing with LFP signals from the motor cortex of a Rat recorded during a lever push task. First panel: signal from one channel after CAR and BPF processing. Second panel: CCA block output that is then thresholded to indicate lever push. Third panel: ground truth lever push recording. The BPF and CCA outputs are provided in ADC steps which have a resolution of $0.195 \mu \text{V/LSB}$. There is a 0.7 second head start on the BCSI signals in comparison to the lever push signal.

four BPF channels and the CCA output for four channels. By comparing the CCA output and the lever push plots, we see correlated increases in CCA power which aligns with the lever push data.

6.5 Conclusion

This chapter presents the NeuralCLIP that is capable of recording neural signals and performing local computation on an FPGA to trigger stimulation. The ability of this modular platform to record and process signals of interest between 20 Hz - 1000 Hz is demonstrated. This work also demonstrates decoding of LFP signals to enable closed-loop operation. Specifically, the device is used to acquire LFP data, process it with the synchronized modular blocks to perform low-complexity BPF and CCA operations. By implementing modular synchronous blocks the device achieves reduced resource and power consumption for this processing. The application demonstrated in this work is a brain-computer-spinal interface that records LFP signals from the motor cortex of a rat, processes them to detect a lever-push intent in order to trigger stimulation in the spinal cord for reanimation of the limb. The NeuralCLIP also allows access to data at each stage of processing for either training or post-recording analysis to enable neuromodulation research. With the implementation on FPGA, this device facilitates development of low power algorithms for closed-loop operation.

Chapter 7

Discussion for Closed-Loop Spike Signal Analysis

7.1 *Signal Acquisition and Stimulation*

The key block in developing a neural interface system is one that records signals from neurons and decodes meaning from it. Existing applications similar to BCSI focus on developing low-power, low-area, autonomous and accurate systems with long lifetime. Several low-power neural potential recording front-ends have been developed [82] and state-of-the-art technology is available commercially from Intan Tech. As we have seen, this low-noise amplifier is capable of providing multiple channels of unipolar recording with 16 bits of precision and more than 20 Ksps per channel. There are three ways of handling this large amount of data coming from the recording FE. Firstly, stream the data out using a low-power communication method like BSC as we have seen in Chapter 3. Secondly, perform on-board computation to derive meaning from recorded data as with the BCSI device. Finally, compress the data (data reduction) and then stream it out to the user. This is especially useful when there are power/bandwidth limitations and the data is necessary for further study in the field. This section focuses on the final method to provide a comparison of potential on-device processing for neural spike signals. The need for such processing in the future stems from the limitations of performing computation on-device due to the transient nature of WPT. Which means, over time and varying position of the RX relative to TX, the amount of power harvested by the RX is subject to variations [83] [84]. This in-turn means that any wirelessly powered computation platform must be optimized for low-energy availability. One of the ways to overcome this challenge is to develop power-aware platforms for computation. The following section analyzes neural spike signal processing from this perspective.

7.1.1 BCSI Task Setup

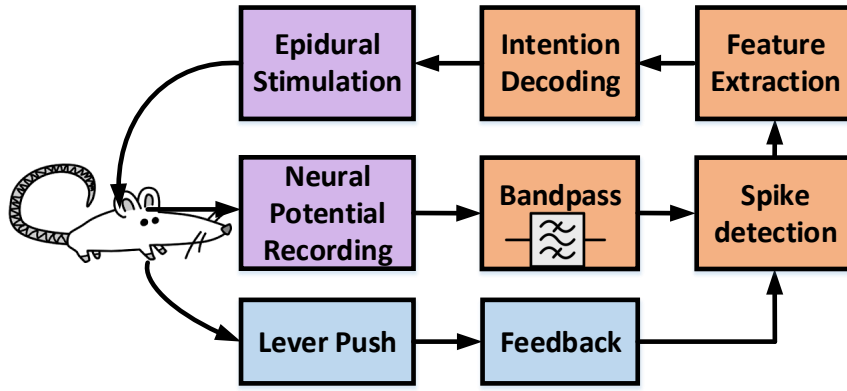


Figure 7.1: Signal processing steps involved in the closed-loop BCSI system, taking a rat as the subject

The task at hand for the BCSI system is shown in the 7.1. In the BCSI application we use closed-loop processing to stimulate with trigger decoded from a recorded signal. The signals to be analyzed in this section are obtained using the TDT system and processed in MATLAB. The experiment involves a rat pushing a lever with its right paw to release food/drink through a valve. An uninjured rat is used in the initial phases of experiments to obtain neural potentials and corresponding lever press times. The lever press data can be used to validate the accuracy of detection algorithms. 16 channels of recording electrodes in the motor cortex of the rat record the neural potentials. These signals are then filtered and the signal components responsible for lever push are identified and used to issue a cue for stimulation. The motivation and design concept for an adaptable closed-loop neural interface is discussed in [85]. It analyzes a distributed architecture that splits the recording task load among several satellite modules distributed around a central external module that serves as a control center. The BCSI vision is a fully wireless implantable system that can record, process, communicate when necessary and provide stimulation in other cases. External control is necessary only for off-line training of supervised algorithms, as will be discussed later.

7.2 Intent Decoding For Closed-Loop Operation

The raw neural data obtained from the rat motor cortex consistses of 16 channels of electrical signals from multiple neurons around it. The goal here is to identify the channels (with respective neurons) that represent the event, which is a lever press using the forelimb. The raw data is first filtered to the band of interest. The two types of signals that can be used from such recordings are neural spikes and local field potentials (LFPs). The configuration for sampling rate and filters for each is listed in Table 7.1. Respective analog filters can be used for obtaining the signal of interest while recording. Detection of an event from the recorded signals can be implemented in multiple stages. When using the spikes, we need to estimate the spike firing rate in a channel associated with the event to determine whether the event occurred or not. Prior literature gives us several algorithms to perform

Table 7.1: Neural Signal Domain Parameters

Signal	Sampling Rate (kHz)	Band (Hz)
LFP	1	1-500
Spikes	20	200-7500

this with varying levels of accuracy [86] [87] and complexity. The three stages that are involved in typical detection for closing the loop are 1) detection, 2) feature extraction (FE), and 3) classification and control as investigated in [88]. Detection involves a simple method to differentiate the spikes from surrounding noise such as absolute value thresholding (ABS) or using nonlinear energy operators (NEO). FE reduces the dimensionality of the signals of interest and extracts primary features that represent the spike, like integral transforms (IT) and discrete derivatives (DD). Classification is used to identify specific kinds of signals that represent the event once the spike has been detected and its features have been extracted. In this case, classification can be used to confirm if the signals detected and their respective features correlate to our signal of interest. It can also be used to indentify and accommodate for varying signal shapes over time, due to plasticity. With each of these stages the complexity/time of operation and power required increase and with them the accuracy in detecting the signal of interest increases. In the case of a wirelessly powered system, it becomes futile to shoot for high accuracy with complex algorithms when there is limited power available. Here, a tradeoff

with accuracy to extend the lifetime of device operation might be a better solution. When there is a loss in the WPT link, with the measure of the available power in a reservoir and the power required to execute a minimal algorithm we can extend the device lifetime till it re-establishes the WPT link. The goal is to tune the complexity of detection and FE to identify an event even in the absence of continuous WPT and extend device operation lifetime. The tradeoff here is the accuracy with which a specific event is detected, as will be shown in the following section. A MATLAB implementation of the algorithms specified above were implemented to validate their performance.

7.2.1 Spike Detection

The ABS and NEO algorithms were compared to a standard signal-tailored threshold to understand their performance characteristics. The data for analysis was obtained from the motor cortex of a rat that was performing the lever press task. About 40 to 70 trials were performed in a 15 minute window on six separate days and the 16 channels of data were extracted using the TDT system.

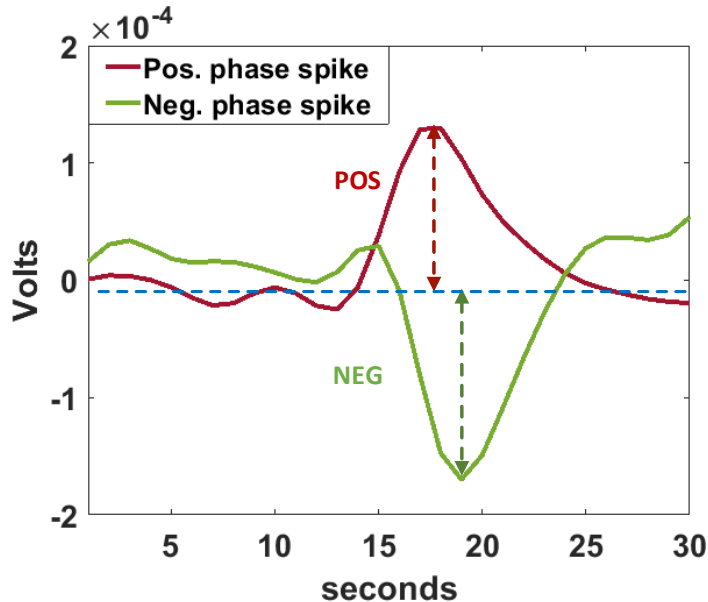


Figure 7.2: Template for positive and negative phase spikes that are found in the recorded time series data

The lever press stamps were used to identify the time stamp for activity trial and the data for

2s (-1s to +1s around the event) was recorded on each channel around the event. From online observation channels 1,6,8 and 15 did not contain spikes while the rest did. As a reference, peri-event time histogram (PETH) was used to identify channels which had activity right before the event occurred (around 0s). The lever push data served as a time stamp for the event. From the PETH observation channels 2, 9 and 11 had spikes right before the lever push. A standard (STD) thresholding method which was tailored for the spike signal of interest was used as a reference. Fig. 7.2 shows two kinds of spikes that are present in the recorded data. The negative phase spike is used as a template to identify similar spikes from the recorded data. This spike has a characteristic negative amplitude that sets it apart from the noise. The tailored threshold $T1_{std}$ was set using Equation 7.1. $T2_{std}$ is the threshold limit for rejecting artifacts. $\mu_{x(N)}$ is the mean of the signal of

$$\begin{aligned} T1_{std} &= \mu_{x(N)} - 4 * \sigma_{x(N)} \\ T2_{std} &= \mu_{x(N)} + 10 * \sigma_{x(N)} \end{aligned} \quad (7.1)$$

N samples and $\sigma_{x(N)}$ is the standard deviation. The first algorithm implemented is the simple and prevalent detection method, ABS, where the threshold parameters are obtained from the absolute value signal as shown in Equation 7.2. This method is useful since the spikes can be either positive or

$$\begin{aligned} T1_{ABS} &= \mu_{|x(N)|} - 4 * \sigma_{|x(N)|} \\ T2_{ABS} &= \mu_{|x(N)|} + 10 * \sigma_{|x(N)|} \end{aligned} \quad (7.2)$$

negative. This method was proved to be better than just a simple threshold in [89]. A slightly more complex algorithm known as NEO or Teager energy operator (TEO) is the second implementation for spike detection. It has been proposed for use in [89] [86]. The NEO value ψ is derived as shown in Equation 7.3. ψ is large only when the signal is instantaneously large in both frequency

$$\begin{aligned} \psi_n &= x^2(n) - x(n-1) * x(n+1) \\ T1_{\psi(N)} &= \mu_{\psi(N)} + 4 * \sigma_{\psi(N)} \\ T2_{\psi(N)} &= \mu_{\psi(N)} + 50 * \sigma_{\psi(N)} \end{aligned} \quad (7.3)$$

and amplitude (which is essentially the definition of a spike). Two thresholds were set for identifying spikes based on the ψ trace. The scaling constant for the artifact is much higher in this case since the NEO operation scaled the high frequency artifact signal as well. Other proposed methods of setting thresholds include using medians and a scaled version of mean. However, a combination of mean and standard deviation gives a better adaptation to the time varying signals. This works since spikes occur in bursts at a particular frequency but are aperiodic generally. To analyze the complexity

Table 7.2: Number Of Operations For N samples

Algorithm	Additions	Multiplications
STD	3N	N+2
ABS	3N	2N+2
NEO	4N	4N+2

scaling for comparison with implementation we calculate the number of addition and multiplication operations in each of these algorithms. This is summarized in Table 7.2. While ABS has N more multiplications in comparison to STD, NEO has N more additions and 2N more multiplications. This can be related approximately as $C(ABS) = 2 * C(STD)$ and $C(NEO) = 4 * C(STD)$, where C represents the complexity or operation time which translates to amount of power consumed. The algorithms use T1 to identify the spike and T2 to reject artifacts. The recorded signals for analysis are at $\sim 24.414\text{kHz}$ and each spike occurs within a window of ~ 30 samples.

7.2.2 Feature Extraction

The features that help identify a spike are typically its positive and negative lobes that occur at a higher frequency and higher amplitude. Once we have the signals that are detected using methods discussed, FE will give a way of classifying the signal and at the same time provide dimensional reduction. The two methods of FE that are chosen for implementation are Integral Transform (IT) and Discrete Derivatives (DD) from the analysis in [87] and [90]. IT identifies the area under the positive and negative lobes of the detected spikes while DD uses the slope between maxima and minima to classify the signals and is computed as shown in Equation 7.4.

$$\begin{aligned} I_A &= \frac{1}{N_A} \sum_{n=N_A}^{n_A+N_A} s(n) \\ I_B &= \frac{1}{N_B} \sum_{n=N_B}^{n_A+N_B} s(n) \end{aligned} \quad (7.4)$$

Here, s is the spike signal, NA and NB are number of samples in the positive and negative phases of the spike respectively. From the detected spike of 30 samples, the dimension has been effectively reduced to 2 (I_A and I_B)

$$dd_\delta(n) = s(n) - s(n - \delta) \quad (7.5)$$

For the DD method, slope of the signal at each sample point is computed using 7.5, over a few timescales. here s is the spike signal and δ is the time scale that is chosen to be 3 and 7 from [90]. The features $dd_{\delta=3,7(max)}$ and $dd_{\delta=3,7(min)}$ are the selected features that can be used to represent the detected signal.

7.3 Algorithm Analysis Results

A comparison of the two detection methods provided in the previous section with a STD method is implemented in MATLAB to detect spikes from the 16 channels of rat lever-press trials. One-fourth each data train was used to compute the thresholds and the entire data was then used for spike detection. Another observation was that the data on a channel during a particular trial did not have any significant variation in amplitude levels throughout the trial. Fig. 7.3a shows a raw time series of 2s in a channel with spikes and Fig. 7.3b is an enlarged section of the time series signal. The bandpass filtered signals for identifying spikes is shown in Fig. 7.3c with the corresponding enlarged section in Fig. 7.3d. The enlarged section focuses on some neural spikes as well as a large artifact and this section will be used to explain the rest of the processing. The filtered and processed spikes along with the detected spike index for this signal using the STD, ABS and NEO algorithms are shown in Fig. 7.4a, b and c. The computed T1 and T2 threshold levels for each are also plotted for reference. The correct rejection of artifact is highlighted in each of the plots while detected spikes are marked by the index signals. ABS and NEO both picked up four spikes in this section, while STD

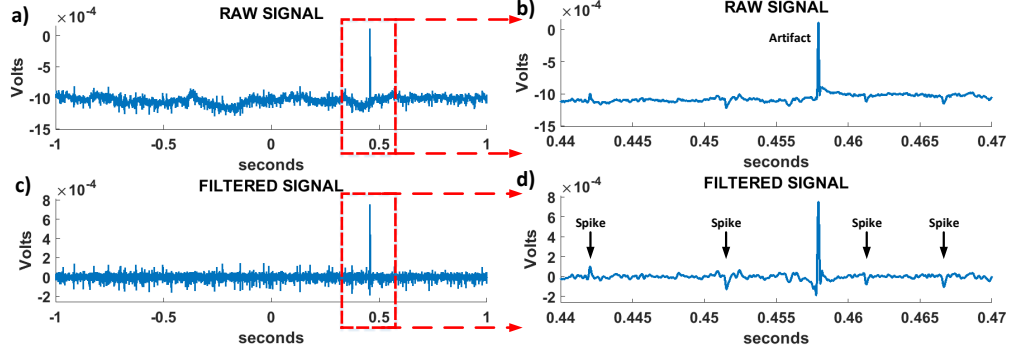


Figure 7.3: a) Raw time series signal recorded from a single channel, b) an enlarged portion of the raw data highlighting four spikes and an artifact within the window. c) filtered version of raw signal and d) filtered version of the enlarged window with arrows pointing to spikes.

(tailored to one kind of signal) could not identify the first positive phase spike. All three successfully rejected the artifact. In all channels the spikes occur within a window of 30 samples. Hence, this window size was used to make sure that a single spike event is counted only once. On detection of the spike, a window of 30 samples centered on the detected index is captured. Fig. 7.4c, d, and e show the spike snippets detected and binned from each algorithm. The analysis of the spike snippets shows that STD picked up signals that it was tailored for (i.e. spikes with a large negative phase). ABS was able to pick up spikes with both positive and negative phases. NEO processed the filtered signal further to amplify spikes and suppress the noise, hence it was able to capture any signal that had instantaneous high frequency and amplitude. The spike count averaged over each channel for the six days for each algorithm are plotted in Fig. 7.5. The value of N for each trial was 48828 samples. The data was averaged for 16 channels over 40-70 trials for 6 days of recordings.

The standard reference for spike counts was a peri-event time histogram that shows firing rate and timing around the event by multiple trials and the spiking activity from online observation. To summarize the observations, all three algorithms scored a relatively low spike count on channels 1, 6 and 15 which did not have any significant spiking activity during online observation using TDT. Also, all three had high spike count on channels 5, 7, 9, 11, 12, 14 and 16. Specifically analyzing the data:

1. The STD algorithm on average detected fewer spikes on each channel and had close to zero

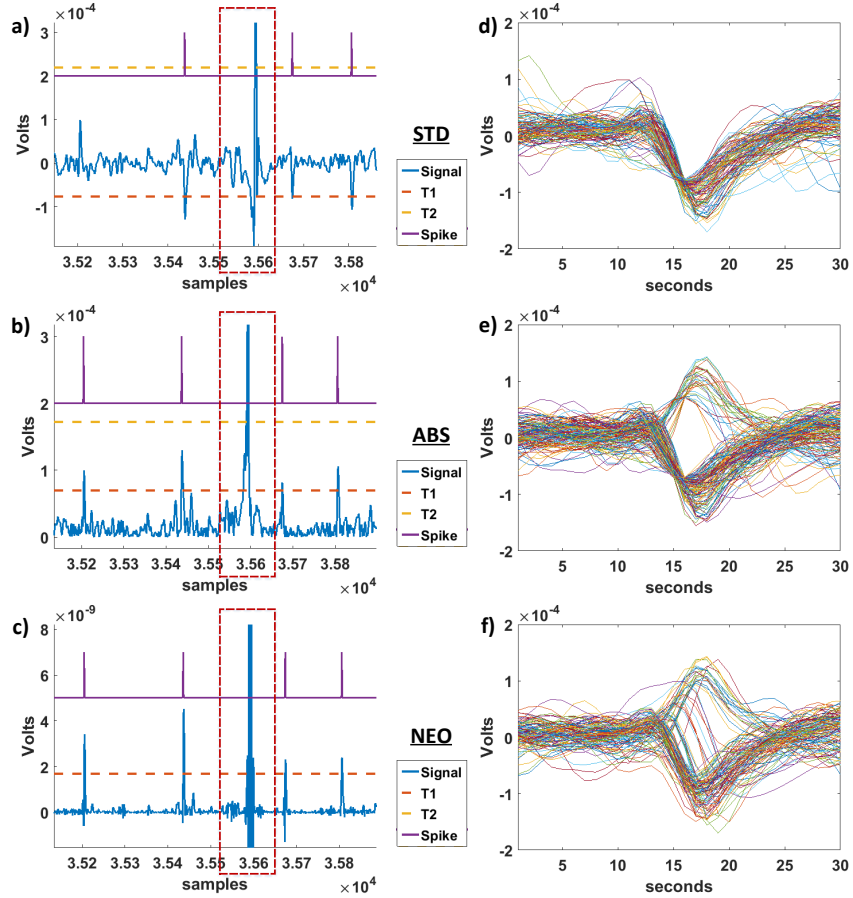


Figure 7.4: a), b) and c) Spike detection using STD, ABS and NEO respectively. The dotted lines indicate the computed thresholds T1 and T2 for each and the purple spike trace marks the index when the spike occurred. All three reject the artifact (highlighted by the red box). d), e) and f) Binned spikes that were detected using each algorithm. STD picks up signal it was tailored to which ABS and NEO pick up other spikes as well.

spikes on channels 1, 3, 6, 13 and 15. The low count on channels 1, 6 and 15 agree with the online observation.

2. Channels 2, 3, 4, 10 and 13 had a large population of spikes with positive phase which were picked up by ABS and NEO but not STD.
3. Channels 9, 11 and 14 had a large population of spikes with negative phase which were picked

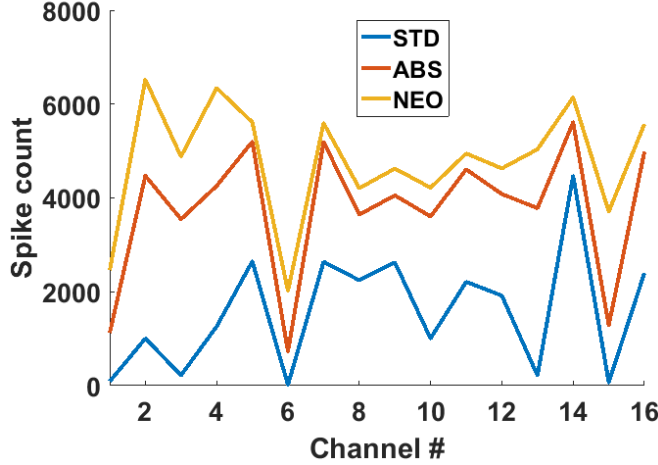


Figure 7.5: Detected spike count for all the trials in each channel, using the different algorithms. NEO recorded the maximum while STD recorded minimum. All channels had fewer spikes on channels 1, 6 and 15.

Table 7.3: CPU Execution Time

Algorithm	Operation time (ms)
STD	1.4
ABS	3.0
NEO	5.2

up by all the algorithms.

This also correlates with previous online observation from the TDT system and the standard where channels 2, 9 and 11 had significant spiking activity right before the lever push. A point to note here is that the detection algorithms can also be used to distinguish the channels in the recording array which have significant spiking activity from ones which do not. This is important to identify the group of neurons that correspond to the given task. The average CPU execution time for

each algorithm block across all samples was also obtained from MATLAB. From Table 7.3, time for execution of ABS is $\sim 2x$ that of STD and that of NEO is $\sim 4x$ of STD. This also corresponds with the complexity computation from previous section. With this we can conclude that increasing complexity leads to increased time for operation and the accuracy for detecting a time varying neural spike is higher. Moreover, detection can also be used to identify channels that do not have any spikes on them, and this leads to further data reduction.

7.3.1 Conclusion

Based on the study in [87], IT and DD have been implemented as feature extraction methods. The study also describes that IT is of lower complexity than DD. The next potential step with respect to spike signal processing on the BCSI system is to obtain classification based on the detected signals by using the implementations of IT and DD. The future objective is to identify a combination of the three detection and two FE algorithms to obtain a gradually increasing complexity for neural signal processing along with increasing accuracy levels for detecting a spike of interest (scaled over multiple channels this translates to intent decoding).

Chapter 8

Discussion and Thesis Conclusion

The focus in this work lies developing wireless biomedical sensing. With the growing number of such sensing devices, solutions to make them small, untethered and battery-free are becoming necessary. This is true especially when they are designed for use as wearables or implantables. To address these requirements this work presents solutions from the aspect of enabling wireless power transfer, wireless communication and computation for low-power wearable and implantable devices. The following section summarizes these specific contributions.

8.0.1 Developing an Ultra-low Power Wearable Biosensing Platform

This platform is aimed at enabling miniaturized fabric-like devices that can be worn on the body like a tattoo, they are simple and disposable and are comfortable to use. The RF Bandaid device in this work is a fully analog sensor platform that can interface to different passive sensors for continuous wireless monitoring of heart rate, breathing rate, temperature and audio. The digitization and processing blocks are decoupled from the platform to a remote receiver, and it only performs sensing and communicates data as FM using UHF backscatter. Thus, the platform operates at power levels as low as $35 \mu\text{W}$ to $160 \mu\text{W}$. Due to the ultra-low power consumption the device achieves continuous operation with harvested energy at distances as far as 13 ft from a transmitter that emits 390 mW of RF power at 915 MHz. In addition to simple biomedical sensing, the secondary aim of this platform lies in development of passive sensing for applications that require continuous monitoring.

8.0.2 Developing an Implantable Neuromodulation Interface

The requirements of the implantable device are much larger in terms of power, data rate and computational complexity. Such a device is intended to live inside the body to perform sensing and provide feedback for treatment and rehabilitation. The specific application that is targeted in this work is rehabilitation and treatment for patients paralyzed due to spinal cord injury. Such an injury

breaks the connection of commands between the brain, spinal cord and the organs (like limbs). The challenges in developing the device and solutions provided in this work are described below.

- The first challenge addressed here is to make the device free of cables and batteries. This work presents a dual-band wireless solution where, the device harvests energy from a HF resonant wireless channel at 13.56 MHz and communicates data using UHF backscatter communication at 915 MHz. The two are implemented to work simultaneously in the near field to ensure continuous power delivery and reliable communication. Since the application space for this device is in spinal-cord injury treatment, the dual-band device is also implemented to provide electrical stimulation in the spinal-cord for reanimation of paralyzed limbs. The results from testing this device *in vivo* a rat are also provided.
- Having established the ability to deliver power and communicate with the device, the next challenge addressed here is localized power delivery. When the device is on a moving target, there is a need to localize the device and deliver power to it for higher efficiency. Typically devices have out-of-band communication modules that communicate their location to the power transmitter. This, however, comes with the power and computation overhead on the receiver. This work presents a phased-array echolocation method, where the reflections on a pair of phased-array coils can be analyzed to localize the device in 2 D space and use phase controlled beam-forming to deliver localized power to it. This method moves the overhead of localization from the power constrained implantable device to the unlimited resources on the external transmitter. By using the phased-array beam-forming method, we also achieve higher efficiency in terms of wireless power transfer.
- The most important aspect of an implantable device is its ability to function without depending on external controllers. This requires the implantable device to be capable of some computation. The main limitation with implants are in terms of power, computational resources and size. Hence there is a need to address the need for computation within these limitations. Moreover, there has been very little work in developing closed-loop neural interface devices that are capable of recording neural signals, processing them and using the decoded signal to trigger stimulation. Current efforts at closed-loop processing are implemented on large bench-top setups that are not practical for implantation.

This work presents the Neural Closed-Loop Implantable Platform (NeuralCLIP) that can record neural signals in the range of 20 Hz to 20 kHz as well as provide electrical stimulation.

The NeuralCLIP is an implementation on low-power FPGA, which enables modular computation optimized with respect to the limited resources. Closed-loop processing on the device is demonstrated with respect to the BCSI application, where neural signals (LFP) recorded from the motor cortex of a rat are processed to identify intent for arm motion. Since this device is modular and capable of recording and processing signals like EEG, ECoG, LFP and spikes, it is also developed as a platform for research in closed-loop algorithm development. The device also has a secondary communication channel that provides computation data which can be useful in closed-loop neural and behavioral research.

- One of the key factors in understanding the neural function comes from analyzing neural spike signals. A discussion for future development with respect to spike signal analysis on implantable devices is provided to outline possible future implementation in spike analysis. Three existing methods are compared for their computational complexity and ability to detect and classify spike signals for low power devices. Such analysis methods are useful when the application for the device includes behavioral studies which require analysis on recorded and processed data.

8.0.3 Future Directions

Having established solutions to some of the major challenges in both the wearable as well as the implantable devices for biosensing, some of the future steps to move this domain further are outlined here:

- RF Bandaid: This work has provided an ultra-low power device that enables continuous physiological sensing. The application envisioned is within a room environment where these RF bandaid platforms can perform fully analog sensing. One of the challenges that is inherent to biomedical applications is the security of sensed signals. Within a home the range of the device can be limited to perform secure sensing. However, when such a system is to be deployed in open environments like hospitals the need for securing the transmitted data is imminent. While digital communications systems have established protocols for encrypting data, there is very little work that has been done in the analog domain. Existing work like the Analog Feedback Shift Register in [91] consume large amounts of power and are not useful in ultra-low power applications. Hence there is a need to implement fully-analog and low-power encryption methods for secure analog sensing and communication. The RF bandaid system is

also implemented as a COTS device in this work. While it is capable of operation at ultra-low power levels, implementing it in ASIC form would lead to further reduction in power and size of the device.

- Brain-computer-spinal interface: This work has addressed challenges with power delivery, communication and computation to enable closed loop operation. To fully validate the system, the device has to be tested *in vivo* an animal for long term operation. Towards this, the first steps are to integrate the capabilities at the system level to create a testbed that facilitates wireless closed-loop operation in a rat subject. Secondly, biocompatible packaging is necessary to make the system fully implantable. This work has used PDMS as a solution, however, it is permeable to humidity over time, which makes it unsuitable for long term implantation. Recent work has shown that materials like liquid crystal polymer [92] are highly water resistant and can be used to create an encapsulation for the implants. Finally, the BCSI device is also implemented as a COTD platform that is flexible for development in the algorithm domain as well as analysis for treatment of neural disorders. Since the device is FPGA-based it provides ease of translating the implementation into an ASIC for specific applications, which can result in further reduction in power levels.

Bibliography

- [1] A. Al-Fuqaha, M. Guizani, M. Mohammadi, M. Aledhari, and M. Ayyash. Internet of things: A survey on enabling technologies, protocols, and applications. *IEEE Communications Surveys Tutorials*, 17(4):2347–2376, Fourthquarter 2015.
- [2] Vaishnavi Ranganathan, Sidhant Gupta, Jonathan Lester, Joshua R. Smith, and Desney Tan. Rf bandaid: A fully-analog and passive wireless interface for wearable sensors. *Proc. ACM Interact. Mob. Wearable Ubiquitous Technol.*, 2(2):79:1–79:21, July 2018.
- [3] P.V. Nikitin and K.V.S. Rao. Theory and measurement of backscattering from rfid tags. *Antennas and Propagation Magazine, IEEE*, 48(6):212 –218, dec. 2006.
- [4] Zhang T Wang X, Liu Z. Flexible sensing electronics for wearable/attachable health monitoring. *Small(Weinheim an der Bergstrasse, Germany)*, 13(25), October 2017.
- [5] Hsin-Liu (Cindy) Kao, Christian Holz, Asta Roseway, Andres Calvo, and Chris Schmandt. Duoskin: Rapidly prototyping on-skin user interfaces using skin-friendly materials. In *Proceedings of the 2016 ACM International Symposium on Wearable Computers*, ISWC ’16, pages 16–23, New York, NY, USA, 2016. ACM.
- [6] Dae-Hyeong Kim, Nanshu Lu, Rui Ma, Yun-Soung Kim, Rak-Hwan Kim, Shuodao Wang, Jian Wu, Sang Min Won, Hu Tao, Ahmad Islam, Ki Jun Yu, Tae-il Kim, Raeed Chowdhury, Ming Ying, Lizhi Xu, Ming Li, Hyun-Joong Chung, Hohyun Keum, Martin McCormick, Ping Liu, Yong-Wei Zhang, Fiorenzo G. Omenetto, Yonggang Huang, Todd Coleman, and John A. Rogers. Epidermal electronics. *Science*, 333(6044):838–843, 2011.
- [7] Elinor Ben-Menachem. Vagus-nerve stimulation for the treatment of epilepsy. *The Lancet Neurology*, 1(8):477 – 482, 2002.
- [8] Helen S. Mayberg, Andres M. Lozano, Valerie Voon, Heather E. McNeely, David Seminowicz, Clement Hamani, Jason M. Schwab, and Sidney H. Kennedy. Deep brain stimulation for treatment-resistant depression. *Neuron*, 45(5):651 – 660, 2005.
- [9] R. R. Harrison and C. Charles. A low-power low-noise cmos amplifier for neural recording applications. *IEEE JSSC*, 38(6):958–965, June 2003.
- [10] Anoop C. Patil and Nitish V. Thakor. Implantable neurotechnologies: a review of micro- and nanoelectrodes for neural recording. *Medical & Biological Engineering & Computing*, 54(1):23–44, Jan 2016.
- [11] X. Liu, M. Zhang, T. Xiong, A. G. Richardson, T. H. Lucas, P. S. Chin, R. Etienne-Cummings, T. D. Tran, and J. Van der Spiegel. A fully integrated wireless compressed sensing neural signal acquisition system for chronic recording and brain machine interface. *IEEE TBCAS*, 10(4):874–883, Aug 2016.
- [12] E. Pepin et al. High-voltage compliant, capacitive-load invariant neural stimulation electronics compatible with standard bulk-cmos integration. In *IEEE BioCAS*, pages 260–263, Oct 2014.
- [13] Jee Woong Lee, Daejeong Kim, Sangjin Yoo, Hyungsup Lee, Gu-Haeng Lee, and Yoonkey Nam. Emerging neural stimulation technologies for bladder dysfunctions. *International neurourology journal*, 19(1):3–11, mar 2015.

- [14] Sarah E. Mondello, Michael R. Kasten, Philip J. Horner, and Chet T. Moritz. Therapeutic intraspinal stimulation to generate activity and promote long-term recovery. *Frontiers in Neuroscience*, 8(8 FEB):1–7, 2014.
- [15] Daniel J. Yeager, William Biederman, Nathan Narevsky, Jaclyn Leverett, Ryan Neely, Jose M. Carmena, Elad Alon, and Jan M. Rabaey. A 4.78mm² fully-integrated neuromodulation soc combining 64 acquisition channels with digital compression and simultaneous dual stimulation. In *VLSIC*, pages 1–2. IEEE, 2014.
- [16] Wei-Ming Chen, Herming Chiueh, Tsan-Jieh Chen, Chia-Lun Ho, Chi Jeng, Ming-Dou Ker, Chun-Yu Lin, Ya-Chun Huang, Chia-Wei Chou, Tsun-Yuan Fan, Ming-Seng Cheng, Yue-Loong Hsin, Sheng-Fu Liang, Yu-Lin Wang, Fu-Zen Shaw, Yu-Hsing Huang, Chia-Hsiang Yang, and Chung-Yu Wu. A fully integrated 8-channel closed-loop neural-prosthetic cmos soc for real-time epileptic seizure control. *IEEE JSSC*, 49(1):232–247, 2014.
- [17] T K T Nguyen, Z Navratilova, H Cabral, L Wang, G Gielen, F P Battaglia, and C Bartic. Closed-loop optical neural stimulation based on a 32-channel low-noise recording system with online spike sorting. *Journal of neural engineering*, 11(4):46005, aug 2014.
- [18] Marco Capogrosso, Tomislav Milekovic, David Borton, Fabien Wagner, Eduardo Martin Moraud, Jean-Baptiste Mignardot, Nicolas Buse, Jerome Gandar, Quentin Barraud, David Xing, Elodie Rey, Simone Duis, Yang Jianzhong, Wai Kin D Ko, Qin Li, Peter Detemple, Tim Denison, Silvestro Micera, Erwan Bezard, Jocelyne Bloch, and Grégoire Courtine. A brainspine interface alleviating gait deficits after spinal cord injury in primates. *Nature*, page 284, nov.
- [19] Understanding the FCC regulations for low-power, non-licensed transmitters.
- [20] The Thing (listening device), 2018.
- [21] A.P. Sample, D.J. Yeager, P.S. Powledge, A.V. Mamishev, and J.R. Smith. Design of an rfid-based battery-free programmable sensing platform. *IEEE Transactions on Instrumentation and Measurement*, 57(11):2608–2615, November 2008.
- [22] V. Talla, M. Buettner, D. Wetherall, and J. Smith. Hybrid analog-digital backscatter platform for high data rate, battery-free sensing. In *Wireless Sensors and Sensor Networks (WiSNet), 2013 IEEE Topical Conference on*, 2013.
- [23] Pavel Nikitin, A.N. Parks, and Joshua R. Smith. RFID-Vox: A Tribute to Leon Theremin. In Joshua R. Smith, editor, *Wirelessly powered sensor networks and computational RFID*. Springer SBM, 2012.
- [24] Michael Buettner, Ben Greenstein, Alanson Sample, Joshua R. Smith, and David Wetherall. Revisiting smart dust with RFID sensor networks. In *Proc. 7th ACM Workshop on Hot Topics in Networks (Hotnets-VII)*, October 2008.
- [25] LTC6906 micropower precision programmable oscillator, Datasheet.
- [26] ADG902 reflective switch, Datasheet.
- [27] BQ25570 nano power boost charger and buck converter for energy harvester powered applications, Datasheet.
- [28] USRP N210 networked series, Datasheet.
- [29] EnFilm - rechargeable solid state lithium thin film battery, Datasheet.

- [30] Bioharness 3 activity monitor, 2018.
- [31] Spire breath and activity tracker, 2018.
- [32] Smart fabrics: The next generation in pressure mapping, 2018.
- [33] Stan J Thomas, Reid R Harrison, Anthony Leonardo, and Matthew S Reynolds. A battery-free multichannel digital neural/emg telemetry system for flying insects. *Biomedical Circuits and Systems, IEEE Transactions on*, 6(5):424–436, 2012.
- [34] S. Naderiparizi, A. N. Parks, Z. Kapetanovic, B. Ransford, and J. R. Smith. WISPCam: A battery-free RFID camera. *2015 IEEE International Conference on RFID, RFID 2015*, pages 166–173, 2015.
- [35] Vamsi Talla, Bryce Kellogg, Shyamnath Gollakota, and Joshua R. Smith. Battery-Free Cell-phone. *Proceedings of the ACM on Interactive, Mobile, Wearable and Ubiquitous Technologies*, 1(2):1–20, 2017.
- [36] Aaron N. Parks and Joshua R. Smith. Sifting through the airwaves: Efficient and scalable multiband RF harvesting. *2014 IEEE International Conference on RFID, IEEE RFID 2014*, pages 74–81, 2014.
- [37] Hubregt J. Visser, A. C F Reniers, and J. A C Theeuwes. Ambient RF energy scavenging: GSM and WLAN power density measurements. *Proceedings of the 38th European Microwave Conference, EuMC 2008*, (October):721–724, 2008.
- [38] Vamsi Talla, Bryce Kellogg, Benjamin Ransford, Saman Naderiparizi, Shyamnath Gollakota, and Joshua R. Smith. Powering the Next Billion Devices with Wi-Fi. 2015.
- [39] Yunfei Ma, Xiaonan Hui, and Edwin C. Kan. Harmonic-WISP: A passive broadband harmonic RFID platform. *IEEE MTT-S International Microwave Symposium Digest*, 2016-August:0–3, 2016.
- [40] Hohyun Keum, Martin McCormick, Ping Liu, Yong-wei Zhang, and Fiorenzo G Omenetto. RESEARCH ARTICLES Epidermal Electronics. *Science*, 333(September):838–844, 2011.
- [41] Pengyu Zhang, Mohammad Rostami, Pan Hu, and Deepak Ganesan. Enabling practical backscatter communication for on-body sensors. In *Proceedings of the 2016 ACM SIGCOMM Conference, SIGCOMM ’16*, pages 370–383. ACM, 2016.
- [42] Hyung-Min Lee, Hangue Park, and M. Ghovanloo. A power-efficient wireless system with adaptive supply control for deep brain stimulation. *IEEE JSSC*, 48(9):2203–2216, Sept 2013.
- [43] Hyo-Gyuem Rhew et al. A fully self-contained logarithmic closed-loop deep brain stimulation soc with wireless telemetry and wireless power management. *IEEE JSSC*, 49(10):2213–2227, Oct 2014.
- [44] S. Zanos et al. The neurochip-2: An autonomous head-fixed computer for recording and stimulating in freely behaving monkeys. *IEEE T. on Neural Systems and Rehabilitation Engineering*, 19(4):427–435, Aug 2011.
- [45] Chet T Moritz, Steve I Perlmutter, and Eberhard E Fetz. Direct control of paralysed muscles by cortical neurons. *Nature*, 456(7222):639–642, 2008.
- [46] Maysam Ghovanloo and Suresh Atluri. An integrated full-wave cmos rectifier with built-in back telemetry for rfid and implantable biomedical applications. *Circuits and Systems I: Regular Papers, IEEE Transactions on*, 55(10):3328–3334, 2008.

- [47] William Biederman, Daniel J Yeager, N.athan Narevsky, Aaron C Koralek, Jose M Carmena, Elad Alon, and Jan M Rabaey. A fully-integrated, miniaturized (0.125 mm^2) $10.5 \mu\text{w}$ wireless neural sensor. *Solid-State Circuits, IEEE Journal of*, 48(4):960–970, April 2013.
- [48] Uei-Ming Jow and Maysam Ghovanloo. Optimization of data coils in a multiband wireless link for neuroprosthetic implantable devices. *Biomedical Circuits and Systems, IEEE Transactions on*, 4(5):301–310, 2010.
- [49] Guillaume Simard, Mohamad Sawan, and Daniel Massicotte. High-speed oqpsk and efficient power transfer through inductive link for biomedical implants. *Biomedical Circuits and Systems, IEEE Transactions on*, 4(3):192–200, 2010.
- [50] Anil Kumar RamRakhyani and Gianluca Lazzi. On the design of efficient multi-coil telemetry system for biomedical implants. *Biomedical Circuits and Systems, IEEE Transactions on*, 7(1):11–23, 2013.
- [51] Guoxing Wang, Peijun Wang, Yina Tang, and Wentai Liu. Analysis of dual band power and data telemetry for biomedical implants. *Biomedical Circuits and Systems, IEEE Transactions on*, 6(3):208–215, 2012.
- [52] J. Besnoff, M. Abbasi, and D.S. Ricketts. High data-rate communication in near-field rfid and wireless power using higher order modulation. *IEEE Transactions on MTT*, 64(2):401–413, Feb 2016.
- [53] Wei-Ming Chen et al. A fully integrated 8-channel closed-loop neural-prosthetic soc for real-time epileptic seizure control. pages 286–287, Feb 2013.
- [54] V. Ranganathan, B. Mahoney, E. Pepin, M. D. Sunshine, C. T. Moritz, J. C. Rudell, and J. R. Smith. A high-voltage compliant neural stimulator with hf wireless power and uhf backscatter communication. *IEEE Wireless Power Transfer Conference (WPTC)*, pages 1–4, 2016.
- [55] Python client for LLRP-based RFID readers, howpublished = <https://github.com/ransford/sllurp>,
- [56] S.J. Thomas et al. A battery-free multichannel digital neural/emg telemetry system for flying insects. *Biomedical Circuits and Systems, IEEE Transactions on*, 6(5):424–436, Oct 2012.
- [57] V. Talla, V. Ranganathan, B. Mahoney, and J. R. Smith. Dual band wireless power and bi-directional data link for implanted devices in 65 nm cmos. *IEEE International Symposium on Circuits and Systems (ISCAS)*, pages 658–661, 2016.
- [58] V Talla, BH Waters, and JR Smith. A study of detuning effects and losses in implantable coils for biomedical wireless power transfer. *Session 4A4 SC4: Wireless Energy Transmission and Harvesting*, page 1369, 2013.
- [59] Yat-Hei Lam, Wing-Hung Ki, and Chi-Ying Tsui. Integrated low-loss cmos active rectifier for wirelessly powered devices. *Circuits and Systems II: Express Briefs, IEEE Transactions on*, 53(12):1378–1382, 2006.
- [60] Jordan S Besnoff and Matthew S Reynolds. Near field modulated backscatter for in vivo biotelemetry. In *RFID (RFID), 2012 IEEE International Conference on*, pages 135–140. IEEE, 2012.
- [61] V Ranganathan. Verilog implementation of the EPC Gen2 RFID protocol. <https://bitbucket.org/vnattar/epc-gen2-verilog/src>.

- [62] B.H. Waters, B.J. Mahoney, Gunbok Lee, and J.R. Smith. Optimal coil size ratios for wireless power transfer applications. In *Circuits and Systems (ISCAS), 2014 IEEE International Symposium on*, pages 2045–2048, June 2014.
- [63] R. Johari, J.V. Krogmeier, and D.J. Love. Analysis and practical considerations in implementing multiple transmitters for wireless power transfer via coupled magnetic resonance. *Industrial Electronics, IEEE Transactions on*, 61(4):1774–1783, April 2014.
- [64] J.J. Casanova, Zhen Ning Low, and Jenshan Lin. A loosely coupled planar wireless power system for multiple receivers. *Industrial Electronics, IEEE Transactions on*, 56(8):3060–3068, Aug 2009.
- [65] A Uchida, S. Shimokawa, H. Kawano, K. Ozaki, K. Matsui, and M. Taguchi. Phase and intensity control of multiple coil currents in mid-range wireless power transfer. *Microwaves, Antennas Propagation, IET*, 8(7):498–505, May 2014.
- [66] Jouya Jadian and Dina Katabi. Magnetic mimo: How to charge your phone in your pocket. In *Proceedings of the 20th Annual International Conference on Mobile Computing and Networking, MobiCom ’14*, pages 495–506, New York, NY, USA, 2014. ACM.
- [67] Dukju Ahn and Songcheol Hong. Effect of coupling between multiple transmitters or multiple receivers on wireless power transfer. *Industrial Electronics, IEEE Transactions on*, 60(7):2602–2613, July 2013.
- [68] Federal Communication Commission. Part 15: Radio frequency devices. *Electronic Code of Federal Regulations*, Title 47: Telecommunication (47CFR15), 2014.
- [69] Benjamin H. Waters, Brody J. Mahoney, Vaishnavi Ranganathan, and Joshua R. Smith. Power Delivery and Leakage Field Control Using an Adaptive Phased Array Wireless Power System. *IEEE Transactions on Power Electronics*, 30(11):6298–6309, 2015.
- [70] V. Ranganathan, B. H. Waters, and J. R. Smith. Localization of receivers using phased-array wireless power transfer systems. In *2015 IEEE Wireless Power Transfer Conference (WPTC)*, pages 1–4, May 2015.
- [71] L.M. Ni, Dian Zhang, and M.R. Souryal. RFID-based localization and tracking technologies. *Wireless Communications, IEEE*, 18(2):45–51, April 2011.
- [72] Ahmed E. Fouad, Fernando L. Teixeira, and Mehmet E. Yavuz. Time-reversal techniques for miso and mimo wireless communication systems. *Radio Science*, 47(6):n/a–n/a, 2012.
- [73] A Massa, G. Oliveri, F. Viani, and P. Rocca. Array designs for long-distance wireless power transmission: State-of-the-art and innovative solutions. *Proceedings of the IEEE*, 101(6):1464–1481, June 2013.
- [74] D. Arnitz and M.S. Reynolds. Wireless power transfer optimization for nonlinear passive backscatter devices. In *RFID (RFID), 2013 IEEE International Conference on*, pages 245–252, April 2013.
- [75] IJ. Gupta and AA Ksieński. Effect of mutual coupling on the performance of adaptive arrays. *Antennas and Propagation, IEEE Transactions on*, 31(5):785–791, Sep 1983.
- [76] R. Islam and R. Adve. Beam-forming by mutual coupling effects of parasitic elements in antenna arrays. In *Antennas and Propagation Society International Symposium, 2002. IEEE*, volume 1, pages 126–129 vol.1, 2002.

- [77] S. Raju, Rongxiang Wu, Mansun Chan, and C.P. Yue. Modeling of mutual coupling between planar inductors in wireless power applications. *Power Electronics, IEEE Transactions on*, 29(1):481–490, Jan 2014.
- [78] Zhen Ning Low, R.A Chinga, Ryan Tseng, and Jenshan Lin. Design and test of a high-power high-efficiency loosely coupled planar wireless power transfer system. *Industrial Electronics, IEEE Transactions on*, 56(5):1801–1812, May 2009.
- [79] C.M. Zierhofer and E.S. Hochmair. Geometric approach for coupling enhancement of magnetically coupled coils. *Biomedical Engineering, IEEE Transactions on*, 43(7):708–714, July 1996.
- [80] M A L Nicolelis. Actions from thoughts. *Nature*, 409(6818):403–407, 2001.
- [81] Abed Khorasani, Reza Foodeh, Vahid Shalchyan, and Mohammad Reza Daliri. Brain control of an external device by extracting the highest force-related contents of local field potentials in freely moving rats. *IEEE TNSRE*, 26:18–25, 2018.
- [82] Seung Bae Lee, Hyung-Min Lee, Mehdi Kiani, Uei-Ming Jow, and Maysam Ghovanloo. An Inductively Powered Scalable 32-Channel Wireless Neural Recording System-on-a-Chip for Neuroscience Applications. *Digest of technical papers / IEEE International Solid-State Circuits Conference. IEEE International Solid-State Circuits Conference*, 2010(6):120–121, jan 2010.
- [83] Michael Buettner, Ben Greenstein, and David Wetherall. Dewdrop: an energy-aware runtime for computational RFID. *Proceedings of the 8th USENIX conference on Networked systems design and implementation*, pages 15–15, 2011.
- [84] A P Chandrakasan, R Min, M Bhardwaj, S Cho, and A Wang. Power Aware Wireless Microsensor Systems. *28th European Solid-State Circuits Conference (ESSCIRC'02)*, 2002.
- [85] Lei Hamilton, Marc McConley, Kai Angermueller, David Goldberg, Massimiliano Corba, Louis Kim, James Moran, Philip D Parks, Sang Chin, Alik S Widge, Darin D Dougherty, and Emad N Eskandar. Neural signal processing and closed-loop control algorithm design for an implanted neural recording and stimulation system. *Conference proceedings : ... Annual International Conference of the IEEE Engineering in Medicine and Biology Society. IEEE Engineering in Medicine and Biology Society. Annual Conference*, 2015:7831–6, 2015.
- [86] Sarah Gibson, Jack W Judy, and Dejan Marković. Technology-aware algorithm design for neural spike detection, feature extraction, and dimensionality reduction. *IEEE transactions on neural systems and rehabilitation engineering : a publication of the IEEE Engineering in Medicine and Biology Society*, 18(5):469–478, 2010.
- [87] Sarah Gibson, Jack W Judy, and Dejan Markovic. Comparison of spike-sorting algorithms for future hardware implementation. *Conference proceedings : ... Annual International Conference of the IEEE Engineering in Medicine and Biology Society. IEEE Engineering in Medicine and Biology Society. Conference*, 2008:5015–5020, 2008.
- [88] R Quian Quiroga, Z Nadasdy, and Y Ben-Shaul. Unsupervised spike detection and sorting with wavelets and superparamagnetic clustering. *Neural computation*, 16(8):1661–1687, 2004.
- [89] Iyad Obeid and Patrick D. Wolf. Evaluation of spike-detection algorithms for a brain-machine interface application. *IEEE Transactions on Biomedical Engineering*, 51(6):905–911, 2004.

- [90] Majid Zamani and Andreas Demosthenous. Feature extraction using extrema sampling of discrete derivatives for spike sorting in implantable upper-limb neural prostheses. *IEEE Transactions on Neural Systems and Rehabilitation Engineering*, 22(4):716–726, 2014.
- [91] B. Vigoda, J. Dauwels, M. Frey, N. Gershenfeld, T. Koch, H. . Loeliger, and P. Merkli. Synchronization of pseudorandom signals by forward-only message passing with application to electronic circuits. *IEEE Transactions on Information Theory*, 52(8):3843–3852, Aug 2006.
- [92] Tae Mok Gwon, Chaebin Kim, Soowon Shin, Jeong Hoan Park, Jin Ho Kim, and Sung June Kim. Liquid crystal polymer (lcp)-based neural prosthetic devices. *Biomedical Engineering Letters*, 6(3):148–163, Aug 2016.